2019-12

Land use effects on groundwater recharge in the prairies

Morgan, Laura Rose

UNIVERSITY OF CALGARY

Land use effects on groundwater recharge in the prairies

by

Laura Rose Morgan

A THESIS

SUBMITTED TO THE FACULTY OF GRADUATE STUDIES

IN PARTIAL FULFILMENT OF THE REQUIREMENTS FOR THE

DEGREE OF MASTER OF SCIENCE

GRADUATE PROGRAM IN GEOLOGY AND GEOPHYSICS

CALGARY, ALBERTA

DECEMBER, 2019

Abstract

Land use effects on groundwater recharge in the prairies are poorly understood. Recharge rates are low, driven by snowmelt runoff in the spring. Errors in measurements of water balance components are often greater than the volume of recharge. Land use effects on snowmelt runoff were determined by comparing runoff volumes at two scales: point scale fields and watershed scale with remote sensing. A paired plot study was compared using the water table fluctuation and chloride mass balance methods to estimate groundwater recharge rates for two spring snowmelt events. It was found that cropland fields had greater snowmelt runoff volumes, and thus likely greater groundwater recharge rates. However, given differences in topography and aspect, the water table fluctuation and chloride mass balance techniques were inconclusive with regards to land use effects on groundwater recharge. To increase recharge rates, converting higher topography fields to croplands or installing snow fences along depressions to capture more snow are viable options.

Acknowledgements

First and foremost, I would like to thank my supervisor, Dr. Masaki Hayashi, for his guidance, support, and endless patience throughout the last three years. I would also like to thank Dr. Ed Cey and Dr. Larry Bentley for their help as part of the GRIP project. As well, I would like to thank Dr. Ed Cey and Dr. Jennifer He for being a part of my examination committee.

Many thanks are extended to Rocky View County for use of their elevation data, Alberta Innovates and Alberta Environment and Parks for research funding, and NSERC CREATE for Water Security Program for scholarship support.

I would like to thank the many graduate students and technicians who have helped me along the way. In particular, I would like to thank the GRIP team members Igor Pavlovskii, Aaron Mohammed, Polina Abdrakhimova, and Alexandra Hughes. Thank you for your help in the field and with all of the data analysis. I would also like to thank Brandon Hill, Evan Sieben, and Eric Mott for all of the field help come rain, snow, or minus thirty; broken fingers and all.

Finally, I would like to thank my friends and family. Your support throughout the last three years has kept me sane. Thank you for the love, the laughs, and the many beers.

Table of Contents

List of Tables

List of Figures

List of Symbols, Abbreviations and Nomenclature

<u>Symbol</u>	<u>Definition</u>
TG	Triple G
PPR	Prairie Pothole Region
WNC	West Nose Creek
SH	Spyhill
WF	Woolliams Farm
GP	Grassland Pasture
C24	Alfalfa Field
TGG	Triple G Grassland
TGC	Triple G Cropland
SWE	Snow Water Equivalent (mm)
GPS	Global Positioning System
LiDAR	Light Detection and Ranging
TDR	Time Domain Reflectometry
ET	Evapotranspiration
E_{raw}	Raw evapotranspiration values (mm d^{-1})
E_1	Energy-balance corrected evapotranspiration values (mm d^{-1})
E_2	Sensible heat flux corrected evapotranspiration values (mm d^{-1})
E_{av}	Seven-day average evapotranspiration for days with missing E_1 and E_2 (mm d^{-1})
DEM	Digital Elevation Model
RGB+NIR	Red Green Blue and Near Infrared bands
H	Depth of ponded water (m)
A	Area of pond (m^2)
V	Pond volume (m^3)
DGPS	Differentially corrected Global Positioning System
NDWI	Normalized Difference Water Index
EM	Electromagnetic
WTF	Water Table Fluctuation
CMB	Chloride Mass Balance
LMWL	Local Meteoric Water Line
lc-excess	Line-conditioned excess (‰)
TU	Tritium Units
R	Groundwater Recharge (m)
Δh	Change in head over recharge event for WTF method (m)
S_y	Specific yield (-)
R_{dep}	depression focused recharge rate in (m y^{-1})

P	Annual precipitation (m)
C_P	Chloride concentration in precipitation (mg L^{-1})
Q_{in}	Annual anthropogenic chloride deposition rate (kg m^{-2} y^{-1})
Q_{lat}	Lateral flux of chloride from uplands to depressions (g m^{-2} y^{-1})
A_{up}	Upland area of a given catchment (m^2)
A_{dep}	Maximum ponded area of a given catchment (m^2)
C_{dep}	Chloride concentration in pore-water (g m^{-3})
R_{cat}	Catchment-scale recharge rate (m y^{-1})
C_{gw}	Average groundwater chloride concentration in the catchment (g m^{-3})
d_{lc}	Lc-excess (‰)
a	Slope of the LMWL
b	y-intercept of the LMWL (‰)
S	Standard deviation of d_{lc}
$\Delta\delta^2H$	measurement uncertainty for hydrogen isotopes (2 ‰)
$\Delta\delta^{18}O$	measurement uncertainty for oxygen isotopes (0.25 ‰)
f	fraction of the sample that is contributed by the winter precipitation end member
C_m	Measured isotope ratio in the sample (‰)
C_1	Isotopic composition of winter precipitation (‰)
C_2	Isotopic composition of summer precipitation (‰)
δR_{dep}	uncertainty associated with the depression-focussed recharge rate (m)
$\delta[Cl]$	uncertainty associated with pore-water chloride concentrations (g m^{-3})
δQ_{lat}	uncertainty associated with the lateral chloride flux (mg m^{-2} y^{-1})

Chapter 1. Introduction

1.1 Background

Water use continues to rise throughout the world for industrial, agricultural, and domestic use. With many surface water sources becoming fully allocated for use, increasingly contaminated, or having periods of drought and deluge causing uncertainty in water availability year to year, pressures on groundwater are expected to increase. At the same time, large areas of land are being converted to agricultural fields to increase food production for the growing global population. With these factors, increased knowledge of how changing land uses affect groundwater quantity is needed. In semi-arid climates, where groundwater recharge rates are low, changes in land use can have major effects on groundwater recharge.

The Prairie Pothole Region (PPR) extends from southern Alberta into South Dakota and Iowa in the United States. Climate varies from the comparatively wetter southeast region in the United States to the semi-arid plains of Canada. Covered by glacial deposits such as clay-rich till and glaciolacustrine sediments, the landscape ranges from mildly undulating to hummocky, dotted with numerous small depressions and upland regions. The depression areas frequently fill with water, and are divisible into permanently flooded wetlands, typically fed by groundwater discharge, flow-through wetlands, and both permanent and ephemeral ponds (van der Kamp et al. 2016; Winter and Rosenberry, 1995). The smaller ephemeral ponds are thought to be a main driver for groundwater recharge, typically filling with snowmelt water in spring that infiltrates before the start of the growing season (Rover et al. 2011). Climate change simulations for the PPR have suggested that a warming climate with changing precipitation will greatly reduce the number of permanently flooded wetlands in the PPR (Johnson et al. 2005; Renton et al. 2015).

The Canadian prairie region is primarily covered by low-permeability glacial tills. The region is cold and semi-arid, with soils freezing down to 1.5 metres over the winter, and potential evapotranspiration in the summer greatly outweighing precipitation. In general, groundwater recharge in the Canadian prairies is driven by snowmelt runoff over frozen soil (Hayashi et al. 1998a, Hayashi et al. 2003). The snowmelt runoff collects in the numerous small depressions across the landscape and slowly infiltrates as the soil thaws (Hubbard and Linder 1986; Keller et al. 1988; Hayashi et al. 2003).

Land use in the Canadian prairies is primarily agricultural, with most of the land being used for crops and with remaining grasslands typically grazed by cattle. Conversion of cropland to ungrazed grassland has been found to eliminate ponding of snowmelt water in the spring (van der Kamp et al. 2003), due to the complex interactions of land use and snowmelt runoff. The presence of macropores, larger pores in the soil, formed by plant roots and burrowing animals, can greatly affect the amount of snowmelt infiltration (van der Kamp et al. 2003; Watanabe and Kugisaki 2017). Destruction of near surface macropore networks by grazing animals, tilling, and compaction by farm equipment reduces the amount of infiltration and increases runoff (Fiedler et al. 2002). Conversion of fields between land uses affects snow retention, with crop fields retaining less snow than grasslands (Fang and Pomeroy 2009).

Large regions of the Albertan prairies have been converted to agricultural crop fields, except for some natural grass reserves and grazing pastures used for cattle (particularly in the southwest), with oil and gas wells dotting the landscape. While uncommon in the northwestern portion of the Albertan prairie region, irrigated agriculture dominates in the southeast. Glacial till thickness in Alberta ranges from a few metres in the northwest region to hundreds of metres in the south. While winters are long and cold, they are often punctuated by warm foehn winds, known locally as chinooks, which can raise the air temperature by twenty degrees Celsius over the course of a day. These winds can deplete or completely melt the snowpack before temperatures drop again (Pavlovskii et al. 2019).

In southern Alberta, where surface water resources have been fully allocated in a first-in-time, first-in-right system (Alberta Environment and Parks 2017a), increasing pressures on groundwater are expected. Currently, groundwater extraction rates are regulated using a “Q20” extraction rate (Alberta Environment and Parks 2017b), where this is the assumed sustainable amount of water that can be pumped for 20 years. To provide more meaningful regulations that can ensure water availability for all license holders and the environment, adequate constraints on all groundwater processes, such as recharge, in a region are needed. Without an understanding of the quantity of groundwater recharge to an aquifer system, the sustainability of a pumping rate under changing climates is difficult to ascertain. As land use changes can be driven by climate (e.g., warming temperatures lead to earlier soil thaw and possible planting dates for crops), understanding the processes behind land use effects on groundwater recharge can aid in determining the effect of climate change.

While land-use effects on snowmelt runoff generation have been examined in a catchment in Alberta (van Dijk 2005; Hayashi and Farrow 2014) and between multiple depressions in Saskatchewan (van der Kamp et al. 2003), the mechanisms causing differences in snowmelt runoff and groundwater recharge due to land use are poorly understood. With the semi-arid climate in southern Alberta, groundwater recharge is often on the order of a few to a few tens of millimetres per year, and, due to the potential evapotranspiration in summer being greater than the total precipitation, is heavily reliant on snowmelt runoff and infiltration (van Dijk 2005; Hayashi et al. 1998, Hayashi et al. 2003; van der Kamp et al. 2003). This study aims to understand the effects of land use, specifically dryland agriculture and grasslands, on groundwater recharge in the PPR. This study is part of a larger study on Groundwater Recharge in the Prairies.

1.2 Research Objectives

The main objective of this research is to provide a more complete understanding of the effects of land use on groundwater recharge quantities and processes in southern Alberta. This is completed using a variety of methods, examining the effects of land use on snowmelt runoff processes at a small and large scale, and evaluating the application of chloride and isotope profiles in the Canadian prairies. Methods used include estimating the volume of snowmelt runoff on a field scale, using infrared satellite imagery and a high-resolution digital elevation model to estimate snowmelt runoff between land uses on a larger scale, estimating evapotranspiration and soil moisture differences between land uses, and estimating groundwater recharge using the chloride mass balance and water table fluctuation techniques. The applicability of the chloride mass balance and water table fluctuation techniques in estimating groundwater recharge is examined.

1.3 Thesis Organization

This thesis is organised into six distinct, but related, chapters. The first is an introductory chapter to provide relevant background information. Chapter two is a general outline of the climate and geology of the study sites used in this research. Chapter three examines short-term local-scale estimations of land use effects on snowmelt runoff at two sites in southern Alberta. Chapter four deals with larger-scale variations in land use effects on snowmelt runoff generation using remote sensing techniques. In chapter five, a paired plot site was compared using long-term groundwater recharge estimation techniques to determine a time-averaged groundwater recharge amount beneath two different land uses. A synthesis of all conclusions and prospective future work is presented as the final chapter.

Chapter 2: Overview of Study Sites

2.1 Triple G

The primary study site, called Triple G (TG), is located approximately 100 km east of Calgary, AB, Canada in the PPR (Figure 2.1). The site is in the semi-arid grassland ecoregion (Government of Alberta 2005) and contains a grassland and a cropland field that undergo typical land maintenance for the region (in the form of pasture grazing and crop rotations) near one another.

At the long-term climate station of Gleichen located 40 km south of the site, the 1971-2000 climate normal mean annual precipitation was 335 mm, with approximately 20% falling as snow over the winter (Mekis and Vincent 2011). The mean temperature in January is -11.1 °C and the July mean temperature is 17.0 °C (Mekis and Vincent 2011). The Gleichen station was taken offline in 2005, and as such an updated 1981-2010 climate normal was not available.

Typical soil at TG is Orthic Dark Brown Chernozem (Soil Classification Working Group, 1998). The surficial geology of the region is stagnant ice moraine (Fenton et al. 2013), with oxidized tills at least 14 m thick. Bedrock in the area is the Cretaceous-Paleogene Scollard Formation and is generally 15-20 m below ground surface in the region, although outcrops can be seen near the surface in some locations (Prior et al. 2013). The Scollard Formation is comprised of interbedded sandstone and siltstone, pale to dark grey, with some carbonaceous mudstones.

A paired-plot setup of land uses was instrumented, utilizing a grazed grassland site and rainfed cropland site approximately 1.5 km apart (Figure 2.2). The grassland site is usually grazed; however, it was not in the summer of 2017. In both years of the study, the cropland was planted with spring wheat (*Triticum aestivum*), although crops are usually rotated between cereal and oil crops (e.g., barley, wheat, canola, and mustard). The grassland site was seeded with meadow bromegrass (*Bromus riparius*).

Previous studies conducted at the Triple G Grassland site are covered in Chapter Three and Chapter Five and include site investigation details and groundwater recharge estimations. The cropland site was chosen for development in 2017 based on the proximity to the grassland site established in 2014.

2.2 West Nose Creek and Spy Hill/Woolliams Farm

The West Nose Creek (WNC) watershed is a small (~250 km^2 gross drainage area) watershed northwest of Calgary (Figure 2.1). The watershed is within the parkland ecoregion, which receives slightly more precipitation than the grassland ecoregion (Government of Alberta 2005). Using the 1981-2010 normal climate data from Calgary International Airport, located 14 km east of Spyhill, the average yearly precipitation is 482 mm per year, with approximately 27% falling as snow in the winter months (Alberta Agriculture, 2019; Mekis and Vincent 2011). Mean temperatures in January and July are -6.8 °C and 16.6 °C, respectively (Mekis and Vincent 2011). The main land uses are grasslands (typically grazed) and croplands (either perennial crops like alfalfa or annual crops such as wheat, barley, peas, and canola) (Guha 2007). There is no irrigation in the area.

The surficial geology of the region is glacial till that ranges from zero to forty metres thick, although this is highly variable throughout the area (van Dijk 2005; Farrow 2014). The bedrock is the upper Paleocene Paskapoo Formation, which consists of interbedded sandstones, siltstones, and mudstones (Prior et al. 2013).

Spyhill (SH) is located just south of the WNC watershed, and Woolliams Farm (WF) is located on the eastern edge of the WNC watershed (Figure 2.1, Figure 2.3). The Spyhill site consists of two monitored sites, a grassland depression (GP) and a depression in an alfalfa field (C24). The grassland field containing GP was grazed until 2006 and is covered by smooth brome grass (*Bromus inermis*), as well as alfalfa (*Medicago sativa*), tufted hair grass (*Deschampsia caespitosa*), smooth meadow grass (*Poa pratensis*), and Canadian thistle (*Cirsium arvense*) (Mohammed et al. 2013). Woolliams Farm (WF) is a cropland site approximately 11 km north of SH (Figure 2.3). The field is managed under a typical crop rotation for the region, rotating through barley, malt, peas, and canola. In 2017 the field was planted with peas (*Pisum sativum*), and in 2018 the field was planted with spring wheat (*Triticum aestivum*). These sites have been monitored since 2003.

The surficial tills at SH are, on average, 13 m thick, and are underlain by at 10-30 m thick layer of gravel (EBA Engineering Consultants 2003). Surficial sediments at WF are only a few metres in thickness and directly overlay the bedrock. The primary soil type at SH and WF sites is Orthic Black Chernozem (Hayashi and Farrow 2014).

Previous studies in WNC and at SH and WF are covered more in depth in Chapter Three (SH and WF) and Chapter Four (WNC). WNC and SH and WF were chosen for analysis due to the wealth of data from previous studies (e.g., van Dijk 2005; Guha 2007; Hayashi et al. 2010; Hayashi and Farrow, 2014).

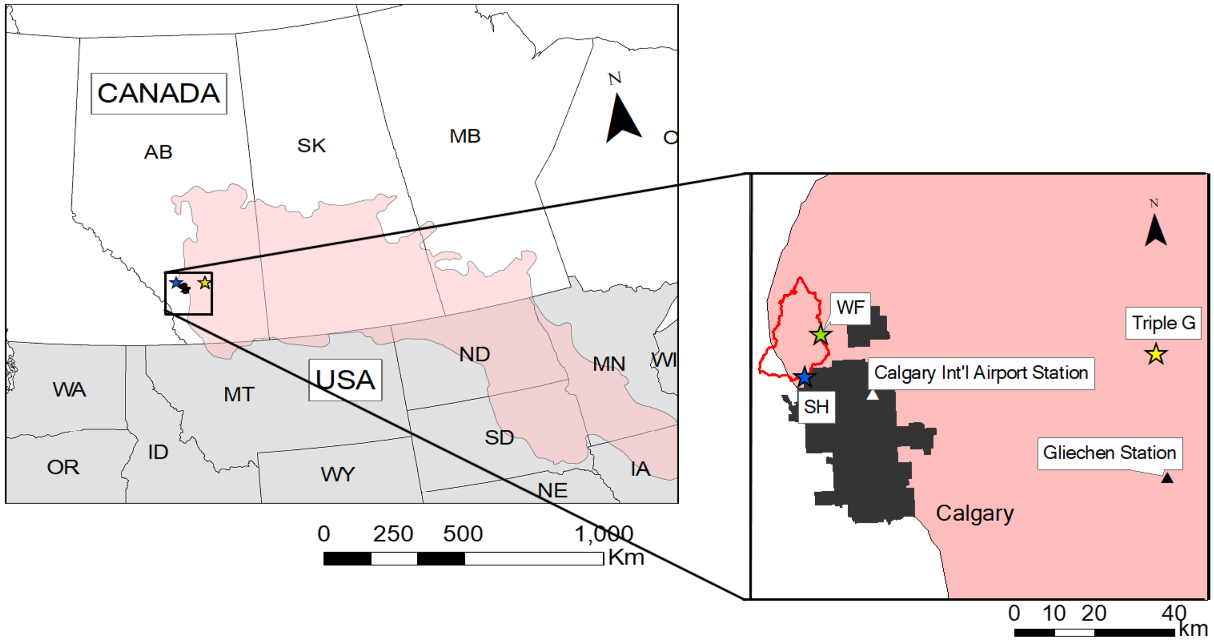

Figure 2.1. Location of the Prairie Pothole Region (PPR, in pink). The blue star in the left image is the location of the WNC watershed, and the yellow star Triple G. Weather stations used for climate normal are indicated with triangles.

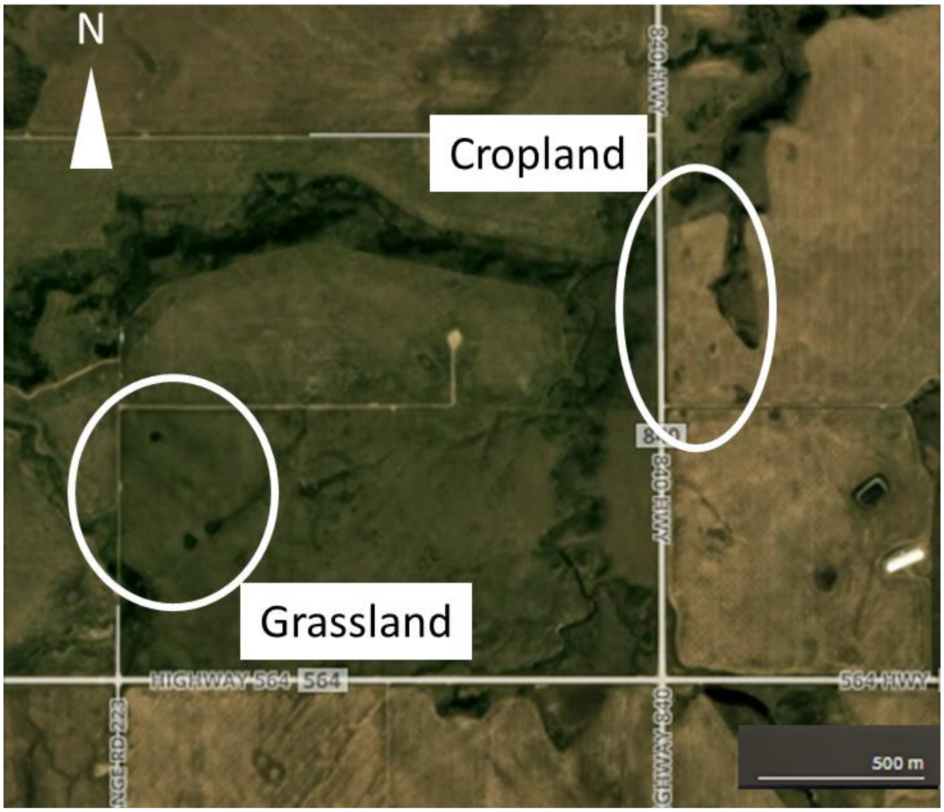

Figure 2.2. TG grassland and cropland sites (Planet Team, image from June 2019).

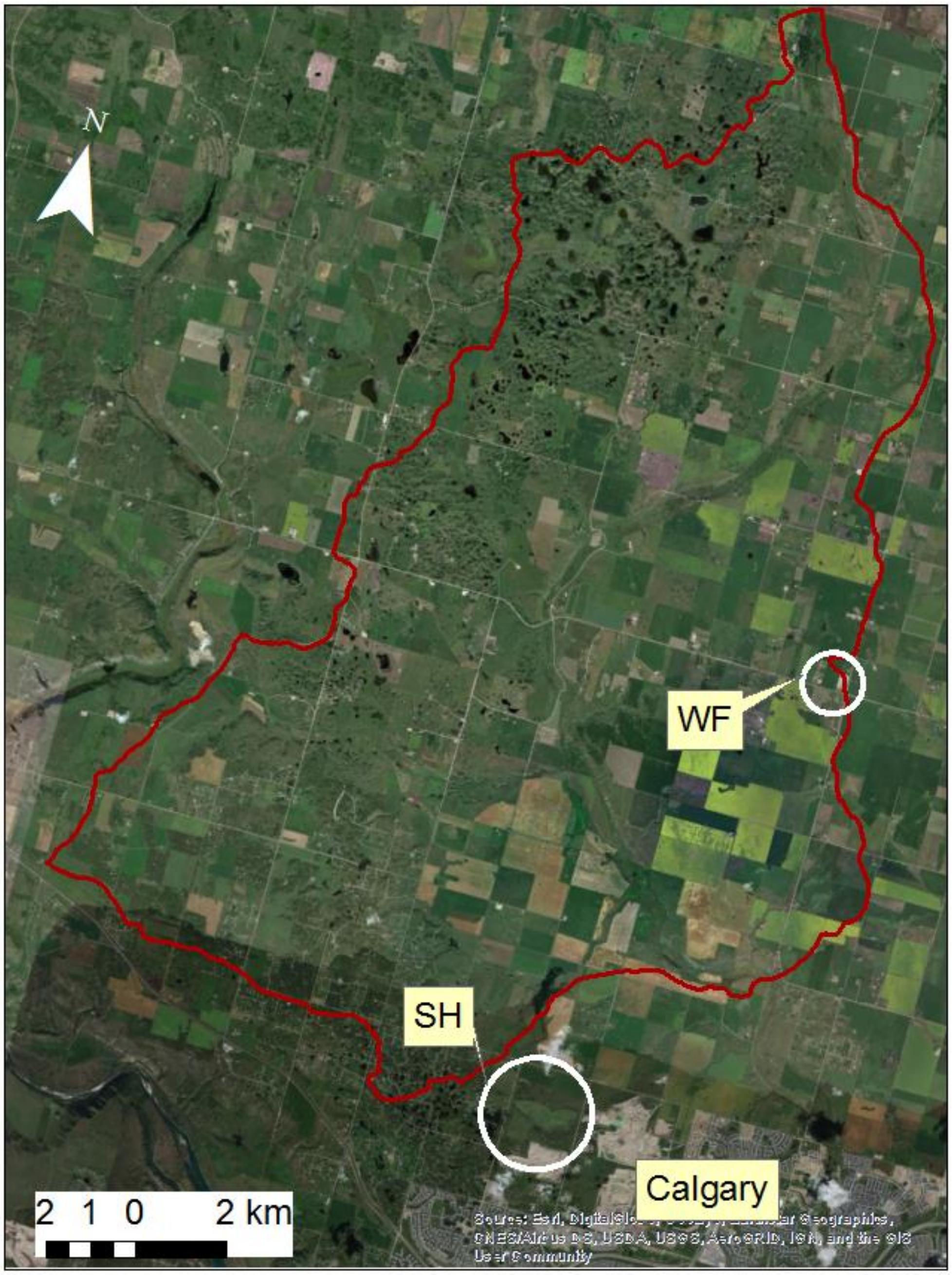

Figure 2.3. Spyhill and Woolliams Farm locations near/within the WNC boundary (red outline) (ESRI World Imagery, image captured September 9, 2016).

Chapter 3. Land-use effects on snowmelt runoff generation

3.1 Introduction

The process of snow accumulation and snowmelt runoff over frozen soil is complex and dependent on many factors (Fang and Pomeroy 2009; Ireson et al. 2013). Throughout the winter, snow accumulates over the landscape and is redistributed by wind. In the prairies of southern Alberta, midwinter melt events often occur, and can partially or completely deplete the snowpack multiple times over the winter (Pavlovskii et al. 2019a). As the snow melts, it initially infiltrates into the soil, until the melt rate exceeds the infiltration rate. At this point, the rest of the snowmelt water runs off and collects in depressions. This ponded water infiltrates slowly as the soil thaws in the spring. Infiltrating water that reaches the water table is the primary source of shallow groundwater recharge. However, much of this shallow groundwater is often cycled from depressions to the upland regions and consumed through evapotranspiration (Hayashi et al. 1998a).

The distribution of snow across the landscape is highly variable and dynamic. Snow is redistributed by wind, leaving scoured hilltops and large drifts on the lee sides of slopes (Pomeroy et al. 2007). Beyond topographical effects, snow is more likely to accumulate in areas with more vegetation, as the vegetation can catch snow. Grasslands, particularly ungrazed grasslands, typically capture the most snow with their high and dense vegetation. Longer stubble left in harvested crop fields can act in a similar manner. Fallow fields, however, typically retain the least amount of snow, as there is no vegetation to trap it as the wind blows (Fang and Pomeroy 2009; van der Kamp et al. 2003; Pomeroy et al. 2007). Up to 15% of snowfall has been estimated to be lost from fallow fields from wind processes alone (Pomeroy et al. 1998).

No-till farming in Canada as a whole has increased from 6.7% of farmland in 1991 to 59% in 2016 (Statistics Canada 2017), with the benefit that many farmers can leave stubble on fields over winter to trap snow and increase soil moisture content in the spring. In the prairie provinces (Alberta, Saskatchewan, and Manitoba) in 2016, no-till farming was used on 68% of agricultural fields, low-till farming was used on 22% of fields, and the remaining 10% were conventionally tilled (Statistics Canada 2017). Man-made structures can affect snow distribution, with snow drifts forming along fences and buildings. These drifts, along with those along sides of slopes, can persist longer in the spring, past the time that the rest of the field has melted.

Snowmelt runoff generation is dependent on several factors, including macropore development, soil type, and antecedent moisture conditions. Macropore networks are created by the roots of plants, burrowing animals, and desiccation cracks caused by the drying of clays, and a greater number of connected macropores increases the amount of water that can infiltrate, instead of running off (LeBlanc 2017; Watanabe and Kugisaki 2017). Croplands typically have less well-developed and connected macropore networks than grasslands, due to the disturbance of the near-surface soil during harvesting and seeding each year (van der Kamp et al. 2003). Grazing by cattle in fields can reduce the near-surface hydraulic conductivity through compaction, increasing runoff, however this impact is highly dependent on grazing intensity (greater grazing intensity increases compaction and decreases hydraulic conductivity) (Fiedler et al. 2002). Destruction of macropores greatly reduces the amount of infiltration that can occur while soil is frozen, while increased frozen water content reduces infiltration rates regardless of macropore structures (LeBlanc 2017).

Another factor affecting runoff generation is the antecedent soil moisture condition in a field (Granger et al. 1984; LeBlanc 2017; Watanabe and Kugisaki 2017; Mohammed et al. in press). As soils freeze, water in the largest water-filled pores freezes first. The greater the water content in the fall, the more likely it is for ice to block the pore space in the matrix as well as water-filled near-surface macropores, limiting the amount of infiltration that can occur to the open macropores (LeBlanc 2017; Watanabe and Kugisaki 2017).

The clay mineralogy of a site can also greatly influence the infiltration and runoff capacities of a soil. Swelling clays, such as smectite, are present in surficial sediments throughout the Canadian prairies and swell as water is absorbed, blocking macropores.

van der Kamp et al. (2003) observed that conversion of crop fields to grasses can drastically reduce, or even eliminate, snowmelt runoff. They showed that snowmelt runoff was gradually reduced as the grasses became established and created an interconnected macropore network. Hayashi and Farrow (2014) estimated snowmelt runoff within the West Nose Creek watershed at the Spyhill and Woolliams Farm sites as part of a decadal study estimating groundwater recharge. Eleven depressions were monitored, and it was found that the cropland site (WF) had the greatest amount of runoff, followed by the alfalfa field (C24), and then by the grassland (GP). Following the cessation of grazing, runoff in the grassland field became almost nonexistent, highlighting the effects of grazing on snowmelt runoff generation. The effects of land use on snow accumulation, snowmelt runoff, and groundwater recharge were examined in GP and C24, which found more snow accumulation in GP, the grassland, but more snowmelt runoff in C24, the alfalfa field (van Dijk 2005).

The purpose of this chapter is to examine the effects of land use on snowmelt runoff generation over two spring melt periods by examining the differences in snow accumulation and snowmelt runoff at a paired plot site and three secondary sites. Additionally, differences in soil moisture and temperature between land uses at the paired plot site are examined for effects of land use on antecedent moisture conditions and soil freezing.

3.2 Methods

3.2.1 Study Sites

The two study areas used for this land use comparison study are Triple G grassland and cropland (TGG and TGC), and Spyhill and Woolliams Farm (SH (GP and C24) and WF). Sites were instrumented with a variety of runoff measurement tools in the depressions, and dedicated snow survey lines established (Figure 3.1, Figure 3.2). TGG and TGC were the primary paired plot study sites, while SH and WF were used to compare snowmelt runoff only. There is a fence surrounding a weather station at WF, as well as along the east side of the field (Figure 3.1a). There is also a fence at TGG, which runs along the southern edge of the west depression (Figure 3.2c).

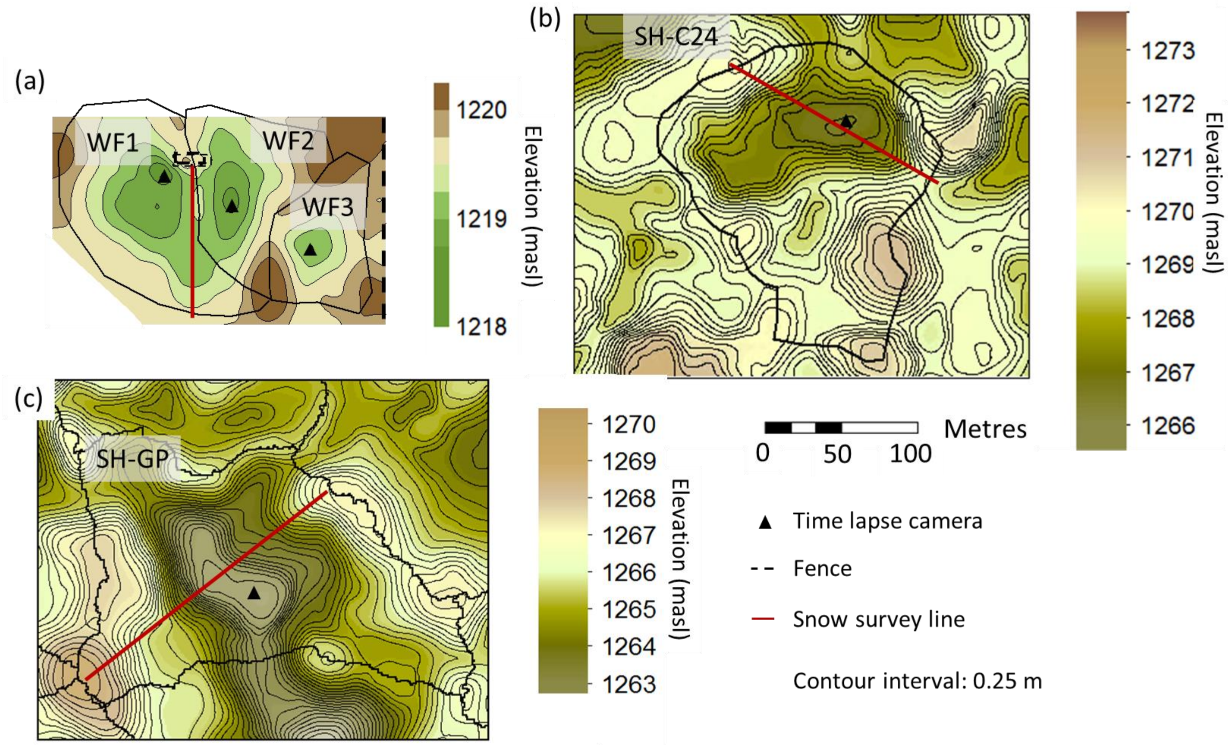

Figure 3.1. Locations of monitored catchments (outlined in black), time lapse cameras (triangles) and snow survey lines (red lines) for (a) Woolliams Farm, (b) C24 depression at Spyhill, and (c) GP depression at Spyhill. Contour interval is 0.25 m.

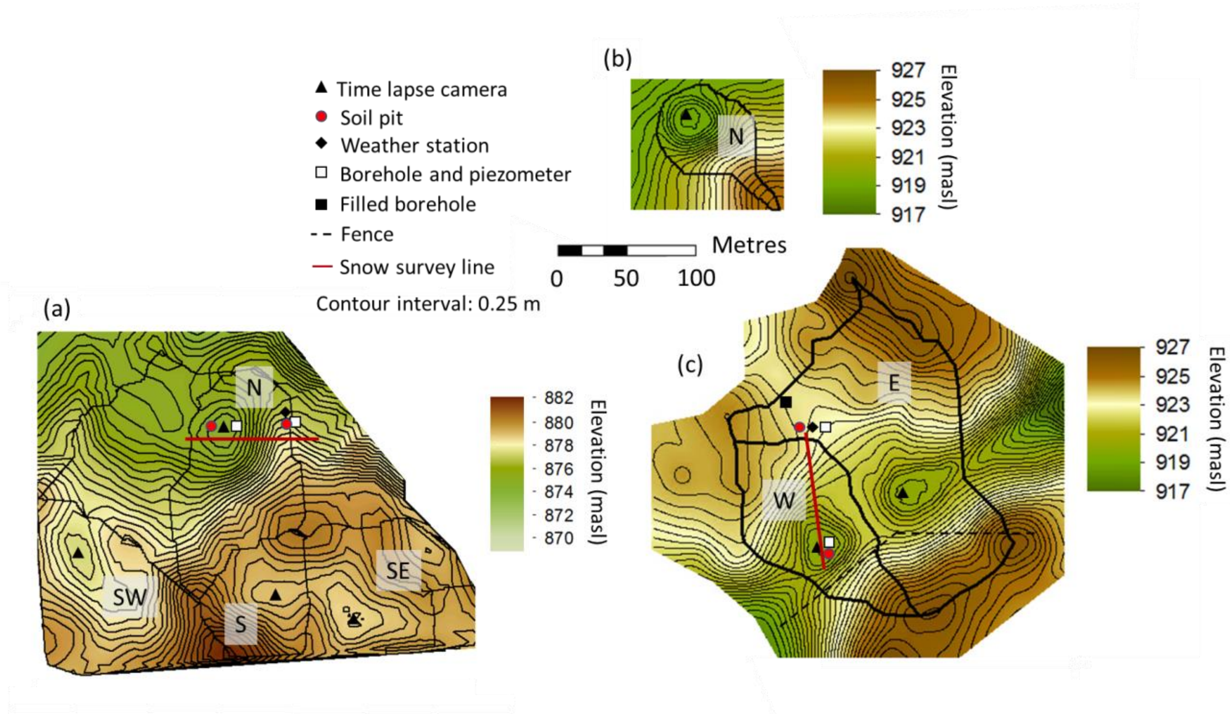

Figure 3.2. Locations of monitored catchments (outlined in black), time lapse cameras (triangles), soil pits (red circles), boreholes (white squares), weather stations (black diamonds), and snow survey lines (thick black lines) for (a) Triple G cropland and (b) and (c) Triple G grassland N and W/E depressions, respectively. Contour interval is 0.25 m.

3.2.2 Previous Data Sets

TGG was the subject of a related groundwater recharge study conducted from 2014 to 2017 (Pavlovskii et al. 2018, 2019a, b; Mohammed et al. in press). Site installations for the grassland were completed as part of this previous study. A laboratory investigation into frozen soil infiltration dynamics was completed using soil cores from TGG (LeBlanc 2017). The saturated hydraulic conductivity of surface soil was measured in the fall using ring infiltrometers at both TGG and TGC (Muenchrath 2019).

SH and WF are part of a long-term groundwater recharge study, which began in 2003 (van Dijk, 2005). The sites have been the subject of numerous studies, including an initial estimate of land-use effects on groundwater recharge in the prairies (van Dijk 2005; Zaitlin et al.

2007). SH was also used as part of the 2014 to 2017 groundwater recharge study (Pavlovskii et al. 2018, 2019a, b).

3.2.3 Snow and Elevation Surveys

Snow water equivalent for each site was determined over the 2018 and 2019 hydrologic years (defined here as the period from November 1 to October 31) by conducting snow surveys after each snowfall event at all sites. Surveys were oriented along upland-depression transects and were of varying length to accommodate the full catchment (Table 3.1). Snow depth was measured every metre along the lines using a metal ruler, and snow samples were taken using a 7 cm internal diameter Meteorological Service of Canada (MSC) snow sampler every 50 m, starting at 0 m. Snow samples were bagged and weighed, and sample hole depth measured, to determine the density of the snow. The average snow depth along the line was used in conjunction with the snow density to determine the snow water equivalent (SWE) for each site. In the winter of 2018, a thick ice layer formed in a snow drift along the snow survey line at TGG. The MSC snow sampler was unable to penetrate the ice layer, so a 3.78 cm cutter size Standard Federal snow sampler was used to collect samples.

At WF and TGG, where large drifts were present, the field average SWE was calculated for the drifts and upland regions separately, then weighted over the proportion of the snow survey line that each portion took up. This was done to avoid erroneously increasing the SWE for the field based on the drift, as the drifts commonly had two to three times the density of the rest of the field.

Total winter precipitation for TG was calculated by correcting precipitation measurements from the Standard weather station, located approximately 5 km north of the site, for wind undercatch (Kochendorfer et al. 2017, Eq. 3). Total winter precipitation for SH and WF was determined by applying the same correction to a weighing precipitation gauge installed at the SH site.

Table 3.1. Snow survey lengths (m) at all study sites.

Site	Snow Survey Length (m)
SH-GP	175
SH-C24	150
WF	100
TGG	100
TGC	100

High-resolution elevation surveys were completed for all of the depressions excluding SH-GP using a differential GPS system (< 5 cm accuracy horizontally and vertically), with points one metre apart near the centre of depressions, ranging out to two to three metres apart near the catchment edges. The data were used to generate a digital elevation model using ArcGIS, and the resulting depressions were analysed to determine the area and volume of water that would occur for each 2 cm of water height added, until the depression would spill (Pavlovskii 2019). Elevation contours for GP and C24 were created from a LiDAR survey completed over the area (LiDAR survey is described in detail in Chapter 4). The depth, area, and volumes were used to generate depth-area-volume functions for TG (Hayashi and van der Kamp 2000) that relate the height or area of ponded water to the volume, and relationships for the SH and WF sites (generated in the same way) from previous studies were used to keep the analysis consistent between studies (Farrow 2014). Volumes of water could then be converted to mm of runoff over the catchment area. Contour maps were generated using ArcMap (ESRI) and Surfer 8 (Golden Software).

3.2.4 Runoff Measurements

Snowmelt runoff was monitored in three ways. The primary method was the use of time-lapse cameras (Wingscapes, TimelapseCam), which took photographs of a staff gauge located at approximately the deepest point in the depression five times per day. In some depressions, pressure transducers were installed to monitor the pond water level at a higher temporal resolution. Due to the highly variable weather during the snowmelt period, however, many of the ponds froze after installation and the transducers recorded unreliable data. Manual measurements of pond height were taken during field visits from the top of a pole with a known elevation.

Infiltration was accounted for in the total volume ponded by determining how much was lost overnight from either the pressure transducers or the time-lapse cameras. The infiltration rate beneath frozen ground calculated using this method was assumed to be constant and was calculated for the full day based on the overnight rate (Hayashi et al. 2003). This volume lost was added back to the total volume, which was then used to calculate the total snowmelt runoff. There were no precipitation events during the ponded periods in 2018 or 2019.

The runoff ratio for each depression was calculated by first dividing the volume of ponded water by the catchment area and converting to millimetres. The value was then divided by the SWE for the field. This normalized value of snowmelt runoff (i.e. runoff ratio) allowed for comparisons between land uses regardless of the observed differences in snow water equivalent between fields.

3.2.5 Soil Moisture and Temperature.

Soil liquid water content and temperature at TGG were measured using capacitance sensors (Stevens, Hydraprobe II) co-located with time domain reflectometry (TDR) probes (LeBlanc 2017; Mohammed et al. in press) in the upland, and with TDR probes and copperconstant thermocouples in the depression. The TGC soil pits contained capacitance sensors and TDR probes in both the upland and depression. Each location had sensors installed at depths of 20 cm, 40 cm, 60 cm, 80 cm, 100 cm, and 150 cm. Data were recorded by dataloggers (Campbell Scientific, CR1000 or CR10X) every half hour and averaged over each day.

3.2.6 Evapotranspiration

Evapotranspiration at TGG and TGC was estimated using the eddy-covariance method. Weather stations were installed in the uplands of each field equipped with a four-component net radiometer (Kipp and Zonen, CNR1), a krypton hygrometer (Campbell Scientific, KH2O), a sonic anemometer (Campbell Scientific, CSAT3B), and a temperature and relative humidity sensor (Vaisala, HMP45C). Ground heat flux plates (Campbell Scientific, HFT3) were installed approximately 5 cm below the surface.

Eddy-covariance data were recorded as 30-min averages, tilt-corrected using a planar fit algorithm (Wilczak et al. 2001), and further processed by applying the Webb-Pearman-Leuning (WPL) correction for both vapour density (Webb et al. 1980) and the separation between the krypton hygrometer and the sonic anemometer (Oncley et al. 2007). Daily average values of sensible and latent heat fluxes were calculated from the processed data. As the latent heat flux data had frequent data gaps due to the hygrometer malfunctioning during precipitation events, daily average values were only computed for days that had less than four hours of data gap. These days accounted for approximately 78 % of the period of this study at TGC, and 73 % at TGG, except during the time when the hygrometer was removed for repairs.

For hydrological studies, it is important to correct the flux data for energy-balance errors (Barr et al. 2012) because the sum of measured latent and sensible heat fluxes is almost always smaller than available energy (= net radiation − ground heat flux) (e.g., Foken 2008). Averaged over the two growing seasons, the ratio of the sum of latent and sensible heat fluxes to available energy was 0.69 at TGG and 0.71 at TGC, indicating consistent energy imbalance. Therefore, an energy-balance correction was made for daily ET values (E_1, mm d^{-1}) for those days with available latent heat flux data using the method described by Hayashi et al. (2010), assuming that the Bowen ratio was correctly measured by the system. For those days with only sensible heat flux data, daily ET (E_2, mm d^{-1}) was calculated from available energy and sensible heat flux assuming a constant energy imbalance ratio (see above) for each site throughout the growing season.

Previous studies have found that energy-balance correction tends to overestimate ET (e.g., Hayashi et al. 2010; Mohammed et al. 2013). The reason for this is unknown, but Charuchittipan et al. (2014) reported that the large-scale secondary circulation responsible for energy-balance errors affects sensible heat more than latent heat, implying that the method used in this study may over-correct for latent heat flux. Therefore, a best estimate of ET is given by an average E_{av} of corrected ET (i.e. E_1 or E_2) and uncorrected ET (E_{raw}). For those days with no E_1 or E_2 available, an average (E_{av}) of the seven days around the missing data was used to fill the gap.

3.2.7 Uncertainty Analysis

The dominant error associated with estimating pond volume was assumed to be a result of using the lime-lapse cameras to estimate the water height, which is directly related to the resolution of the staff gauges. The gauges are divided into 0.0254 m sections, so half of this value was used as the error, or 0.0127 m. For the maximum pond levels, this corresponds to an error of ±8%. While there would likely be errors in the digital elevation model (DEM) related to the accuracy of the differential GPS system, random errors would be likely to cancel out over the entire catchment, and not affect the total volume by an appreciable amount.

The soil moisture probes have a reported accuracy of ±0.03 for fine-textured soils. For the daily soil moisture values used in the water budget, this leads to an uncertainty of 23 mm of soil moisture each day for the entire soil column.

Uncertainty in ET values was determined using the raw uncorrected eddy flux data (E_{raw}) as the lower bound and the corrected data (E_1) as the upper bound. The ratio between the best estimate (E_{av}) and the range of uncertainty (i.e. $E_1 - E_{raw}$) was computed for days that had an estimate available using this method. These ratios were then averaged over the entire growing season and multiplied by the final estimate of growing season ET calculated using the latent heat flux to fill gaps from missing days of data to determine an estimate of error in ET measurements.

3.3 Results

3.3.1 Snow Accumulation and Melt

Snow accumulation across all the transects was measured 2-7 days before the spring melt events, as well as after each snowfall event in 2018. In 2018, the grassland sites had as much or more snow than the croplands (Figure 3.3, Figure 3.4, Table 3.2). In 2019, TGG had a greater SWE than TGC, but at SH and WF, the WF (crop) had the greatest SWE and SH-GP (grass) the least, with SH-C24 (alfalfa) in between (Table 3.2).

Differences in topography and artificial structures across all sites affect snow accumulation. Large drifts formed at multiple sites, including TGG, SH, and WF. The drifts at TGG and SH occurred along the lee sides of slopes, while the drift at WF formed against a fence surrounding weather station equipment. At GP, there were two regions that had little to no snow cover late in the winter of 2018 (Figure 3.3, at roughly 100 m and the end of the snow survey line at 175 m). The region around 100 m is in the depression on ground with little to no vegetation, and the region at 175 m is at the top of a slope.

The snow drift at WF primarily drains into WF1, the easternmost depression (Figure 3.1a), The drift that formed at SH-GP in 2018 was along the lee side of a slope. The drift that formed in 2018 at the TG grassland site had a thick ice layer form during a warmer period. Snow depth was measured above and through this ice layer to determine the total SWE.

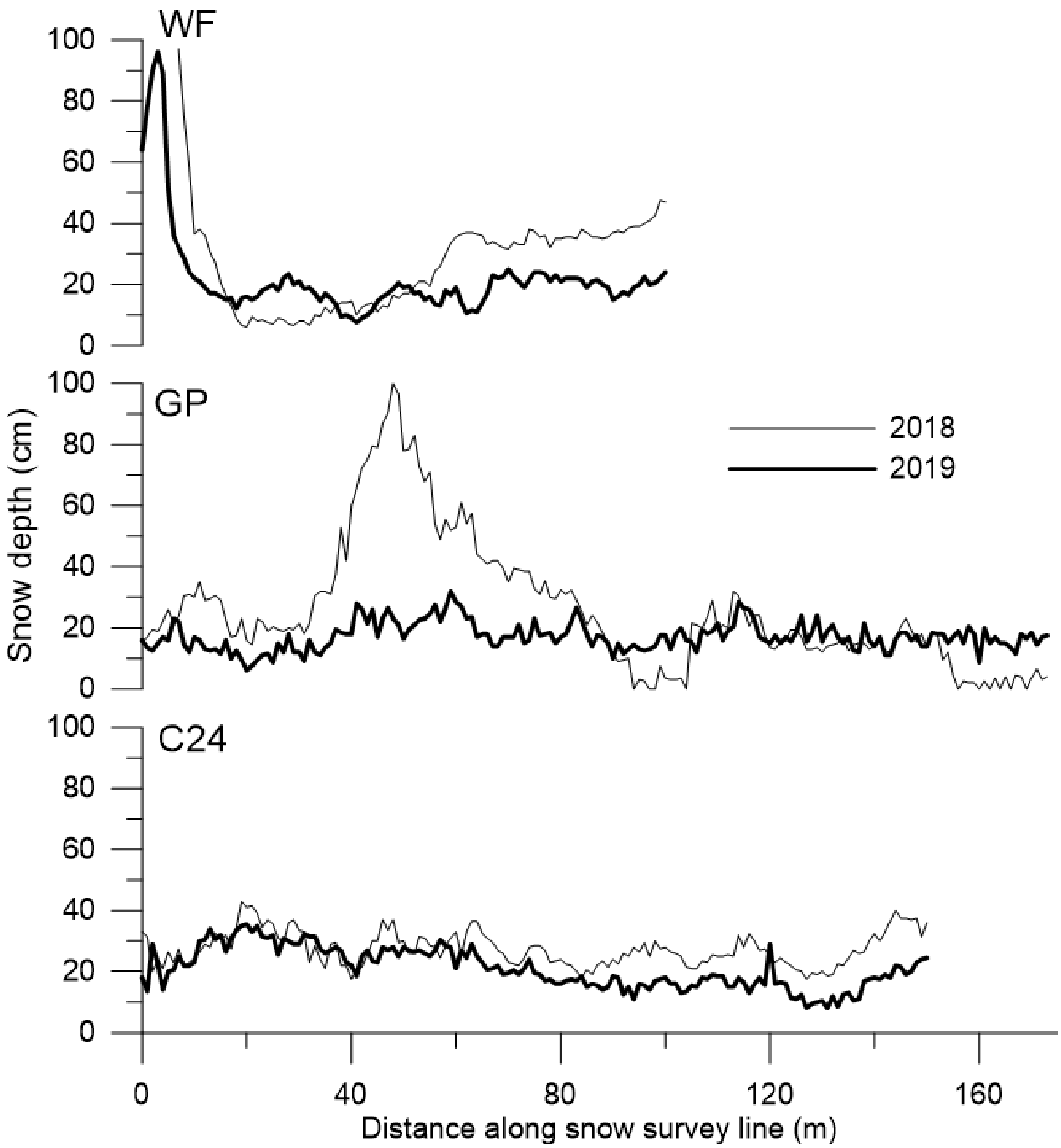

Figure 3.3. Snow depth before spring melt at the Woolliams Farm (crop), Spyhill-GP (grass) and Spyhill-C24 (alfalfa) depressions for 2018 and 2019.

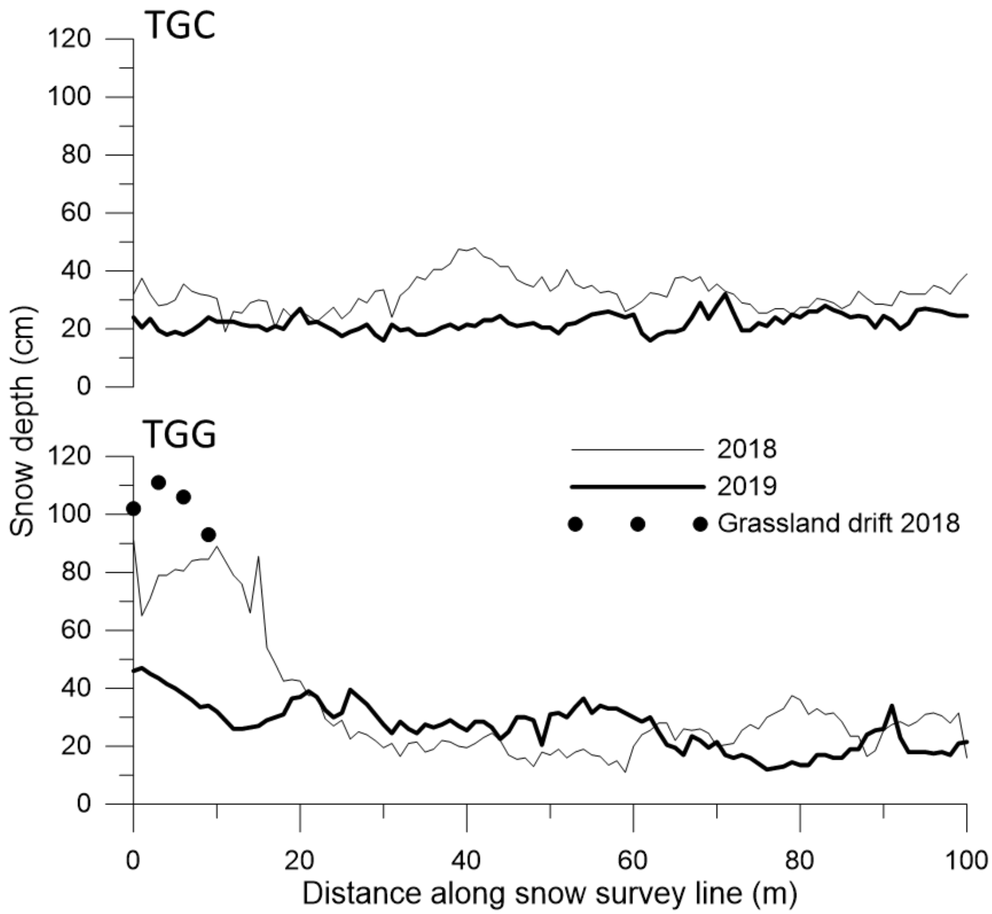

Figure 3.4. Snow depth along the snow survey lines for TGC (top) and TGG (bottom) in 2018 and 2019. Grassland drift 2018 points represent the total depth of the drift, above and below the ice layer.

Despite the consistency in snow depth between years, the snow density was quite different between years. In 2018, the average snow density was 320 kg m^{-3} at both sites at Triple G, while in 2019 it averaged 138 kg m^{-3}. This was also observed at SH and WF, where the average snow density was 256 kg m^{-3} in 2018 and 177 kg m^{-3} in 2019.

There were no midwinter melt events that completely depleted the snowpack in 2018, although there were numerous high wind events that redistributed snow, leading to changes from full to partial snow cover even when temperatures remained below freezing (Figure 3.5). The short warm period in January 2018 did not cause significant melting at any of the field sites. However, in 2019, the snowpack was completely melted by a chinook in January.

Differences in melt date are apparent, with the melt in 2018 occurring a month later than in 2019. A cold period in late March/early April of 2018 pushed the melt date to later in the year. In 2016 and 2017, the final spring melt occurred in mid-March, similar to 2019 (Pavlovskii et al. 2019a).

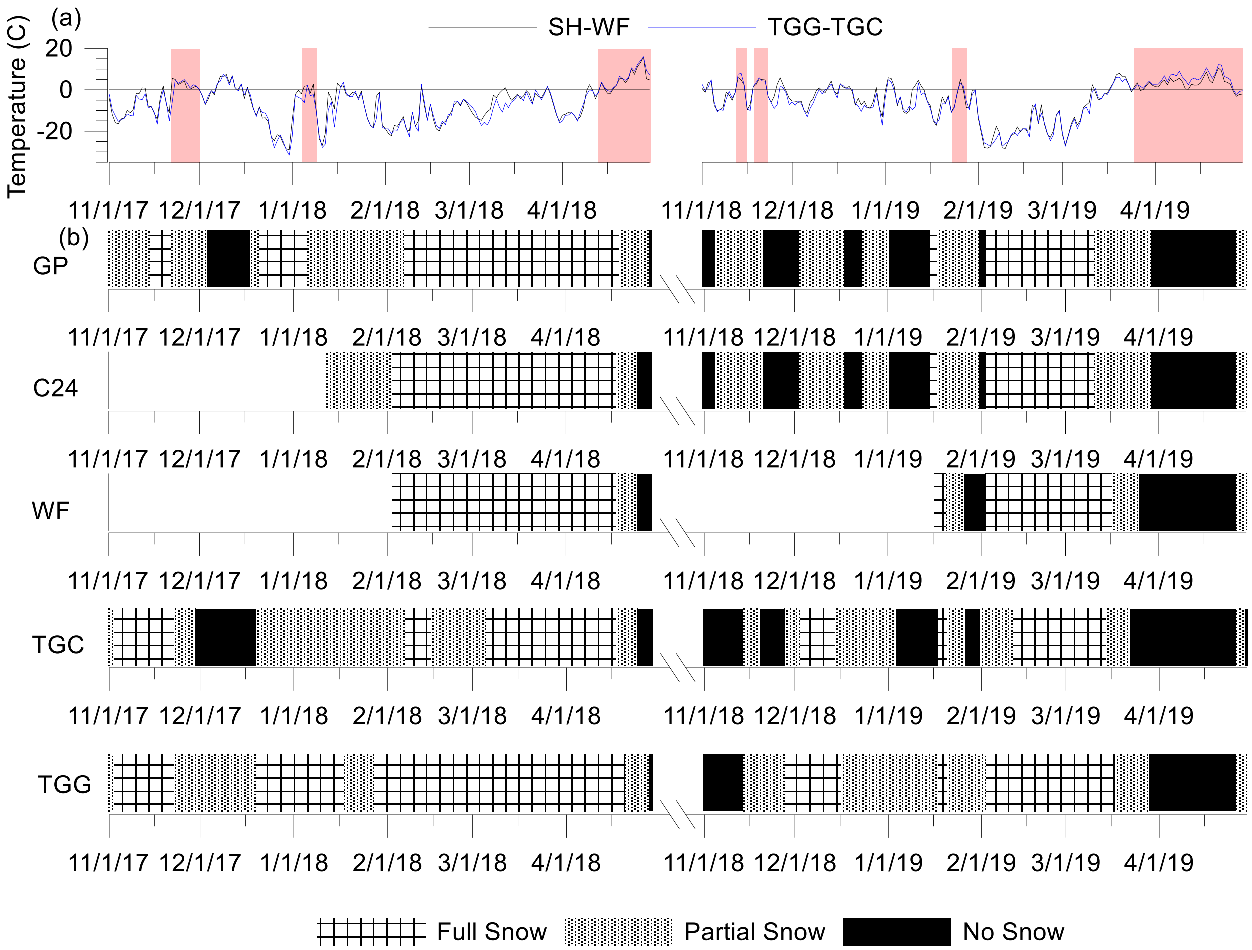

Figure 3.5. Average daily air temperature (a) and snow accumulation at all sites (b) based on time lapse camera images in depressions for November 1 to April 30 of 2018 and 2019. Pink shaded areas indicate air temperatures over 0°C for more than one day. Blank regions in snow accumulation indicate that cameras were not installed.

3.3.2 Snowmelt Runoff

There was a greater volume of snowmelt runoff in TGG than TGC in 2018 and 2019 (Table 3.2). TGG had a higher runoff ratio in 2018, but this switched in 2019, with TGC having a greater runoff ratio. At SH and WF, the greatest amount of runoff was in WF, the cropland. C24, the alfalfa field, had less, and GP, the grassland, did not generate any runoff over the two winters (Table 3.2).

Table 3.2. Snowmelt runoff volume and runoff ratio for 2018 and 2019. In 2019 there was a midwinter melt event that caused complete depletion of snowcover at both TG sites and ponding in the TG grassland, however a snow survey was not conducted prior to the melt event (SWE marked as "--". Total winter precipitation is from November 1 to April 30. *The two SWE values for WF in 2018 and 2019 are with drift/without drift. As the drift drains into WF1, the runoff ratio for the other two was calculated using the without drift SWE.

	2018				2019			
Site	Total Winter Precip (mm)	Pre-melt SWE (mm)	Ponded water volume (mm)	Runoff ratio	Total Winter Precip (mm)	Pre-melt SWE (mm)	Ponded water volume (mm)	Runoff ratio
TGC	110	121	26±2	0.21	87	--	0	--
						25	15±1	0.37
TGG		122	40±3	0.33		--	4.2±0.5	--
						41	9.5±1	0.23
WF	228	140/60*	53/24±4/2	0.38	173	50/39*	35/8±3/1	0.24
C24		84	25±2	0.29		35	0.3±0.1	0.08
GP		91	0	0		26	0	0

At both study sites, the croplands experienced complete snowpack depletion before the grasslands, by three days at all sites in 2018, one week at Triple G in 2019, and one day at SH and WF in 2019 (Table 3.3). Total snowpack depletion at WF was influenced by the large drift that formed against the fence at the site. The field was completely melted, aside from the drift, three days before the C24 and GP in 2019.

Table 3.3. Date of snowpack depletion for monitored sites in 2018 and 2019.

Site	Land use	Date of total snowpack depletion - 2018	Date of total snowpack depletion - 2019
TG	Cropland	April 25	March 22
	Grassland	April 28	March 29
SHWF	Cropland	April 25	March 28
	Alfalfa	April 25	March 29
	Grassland	April 28	March 29

3.3.3 Soil Water Content and Temperature

At TG, the cropland soil was consistently wetter than the grassland. Liquid water contents decreased at all depths in the grassland throughout the growing season, while in the cropland, water contents only decreased at depths of up to 100 cm (Figure 3.6). The presence of a preferential flow path is evident in the grassland upland (Figure 3.6b), with sudden spikes in water contents at all depths following snowmelt at the end of April 2018. This flow path is likely the result of numerous badger and gopher holes near the soil pit. A heavy rainstorm (approximately 70 mm of rainfall) on June 22 and 23, 2018 caused runoff and ponding at both sites, evidenced by the increase in water content to saturation in both the cropland and grassland depressions (Figures 3.6c-d), and in the time-lapse camera imagery of the two main depressions (Figure 3.7). The ponding from the rainfall event also caused an increase in groundwater level (Chapter 5, Figure 5.9).

The greater water content in the cropland also leads to warmer soils in the winter than in the grassland, with the effect more visible in the uplands, where the water contents are more different (Figure 3., Figure 3.8). The grassland soils freeze sooner than the cropland, which is particularly evident in the uplands with the grassland upland freezing on December 4, 2017 and the cropland upland freezing on December 19, 2017. Soil frost penetrated to a greater depth in the upland at TGG than TGC in 2018, however this did not occur in the winter of 2019 when soils froze to similar depths (Figure 3.6 e,f; Figure 3.8 e,f). The general trend of higher water content and temperature in the cropland, however, did continue in 2019 (Figure 3.8).

Soils thawed after a similar length of time after snowmelt in 2018 and 2019 (approximately 3 weeks). This was despite a long period of extreme cold in February that caused soils at both upland locations to freeze down to 1.5 metres (Figure 3.8e,f).

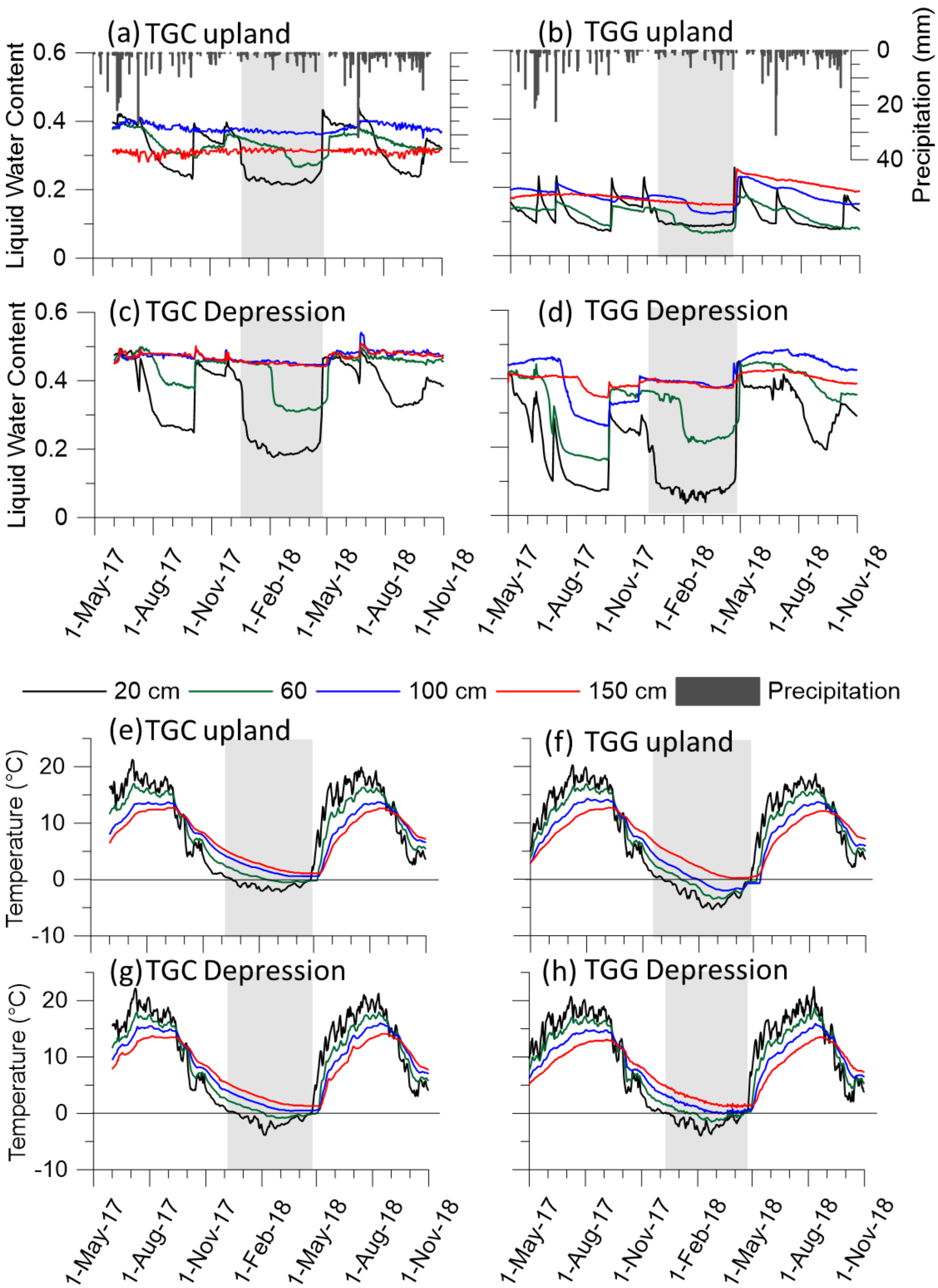

Figure 3.6. Volumetric content of liquid water (a-d) and soil temperature (e-h) at 20 cm, 60 cm, 100 cm, and 150 cm depth at TG in the cropland upland (a,e) and depression (c,g) and grassland upland (b,f) and depression (d,h) for May 2017 to October 2018. Precipitation is shown along the top axis. The time that soil is frozen around the 20 cm sensor is highlighted in light grey.

Figure 3.7. Time-lapse camera imagery from spring 2018 showing pond water levels at TGC and TGG on May 7 (snowmelt runoff), dry ponds following the infiltration of snowmelt runoff water on June 18, and ponded water on June 24 following a large rainstorm over June 22 and 23.

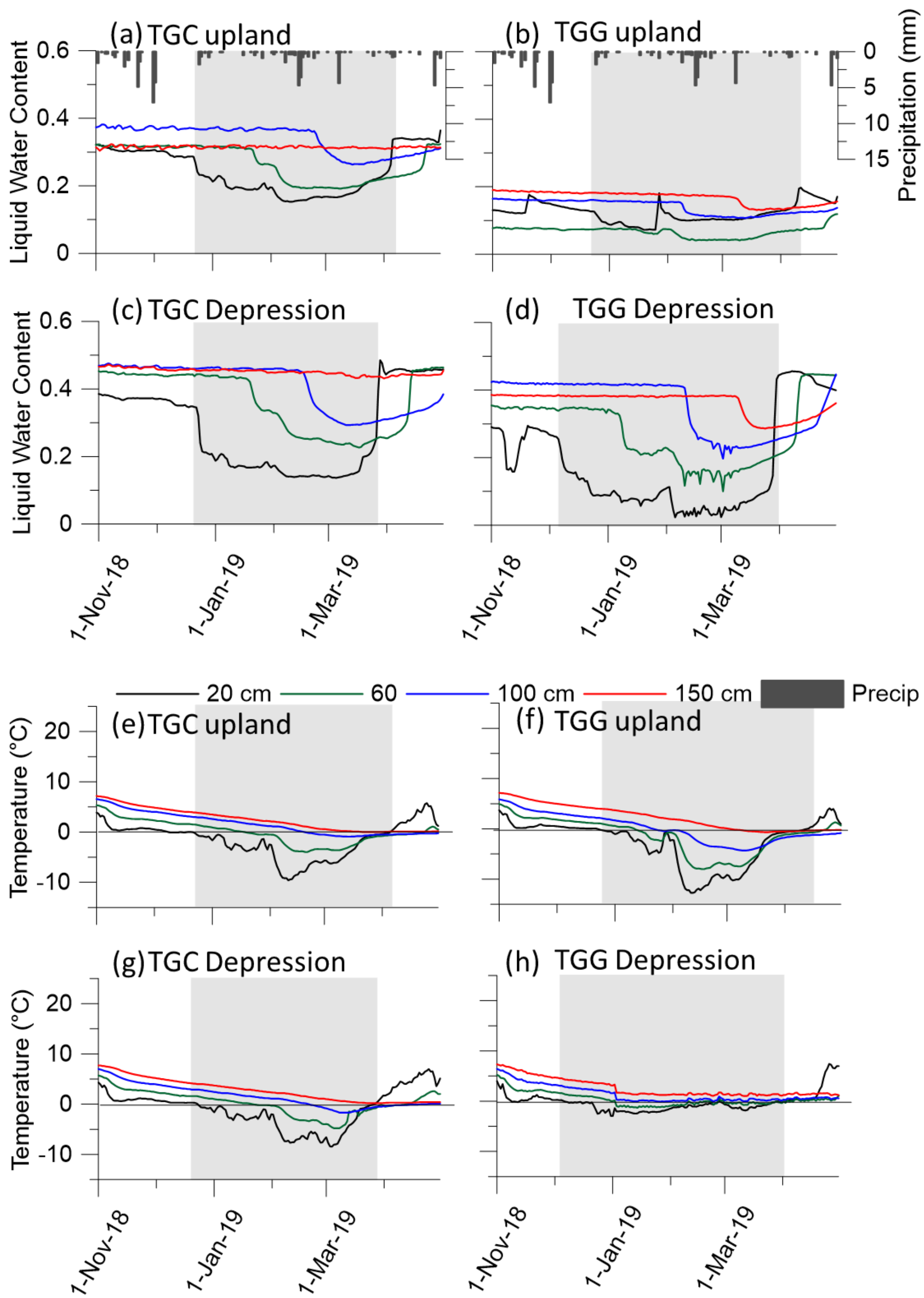

Figure 3.8. Volumetric content of liquid water (a-d) and soil temperature (e-h) at 20 cm, 60 cm, 100 cm, and 150 cm depth at TG in the cropland upland (a,e) and depression (c,g) and grassland upland (b,f) and depression (d,h) for November 2018 to April 2019. Precipitation is shown along the top axis. The time that soil is frozen around the 20 cm sensor is highlighted in light grey.

3.3.4 Evapotranspiration

TGG had greater evapotranspiration and soil moisture loss over the 2017 and 2018 growing seasons than TGC (Table 3.4). Here, the growing season is defined as the period from complete soil thaw to end of hydrological year; i.e. May 14 to October 31, 2018. The ET was greater in the grassland in the early spring before the cropland was planted and throughout fall after maturity (Figure 3.9). Seeding, germination, maturity, and harvest dates were determined for the cropland using time lapse cameras. Maturity date was determined to be when the wheat had completed its lifecycle and was brown throughout the field. An example of the range of uncertainty for the ET measurements were plotted alongside TGG ET from April 1, 2018 to October 31, 2018 for days which had E_{raw} and E_1 values (Figure 3.0).

Table 3.4. Evapotranspiration (ET) (mm) and soil moisture change (mm) for 2017 and 2018 growing seasons from the date of soil thaw (April 16 in 2017 and May 14 in 2018) to October 31. 2017 cropland ET was measured starting on June 2, ET before this time was estimated from 2018 data (indicated with *), soil moisture change in the cropland is from May 15, the date of the soil pit installation (**).

	2017			2018	
Site	ET (mm)		Soil moisture change (mm)	ET (mm)	Soil moisture change (mm)
TGG	Total: 347±49		-171±23	314±44	-155±23
TGC	Known: 270 Unknown: 43*	Total: 313±47	-8**±23	288±35	-42±23

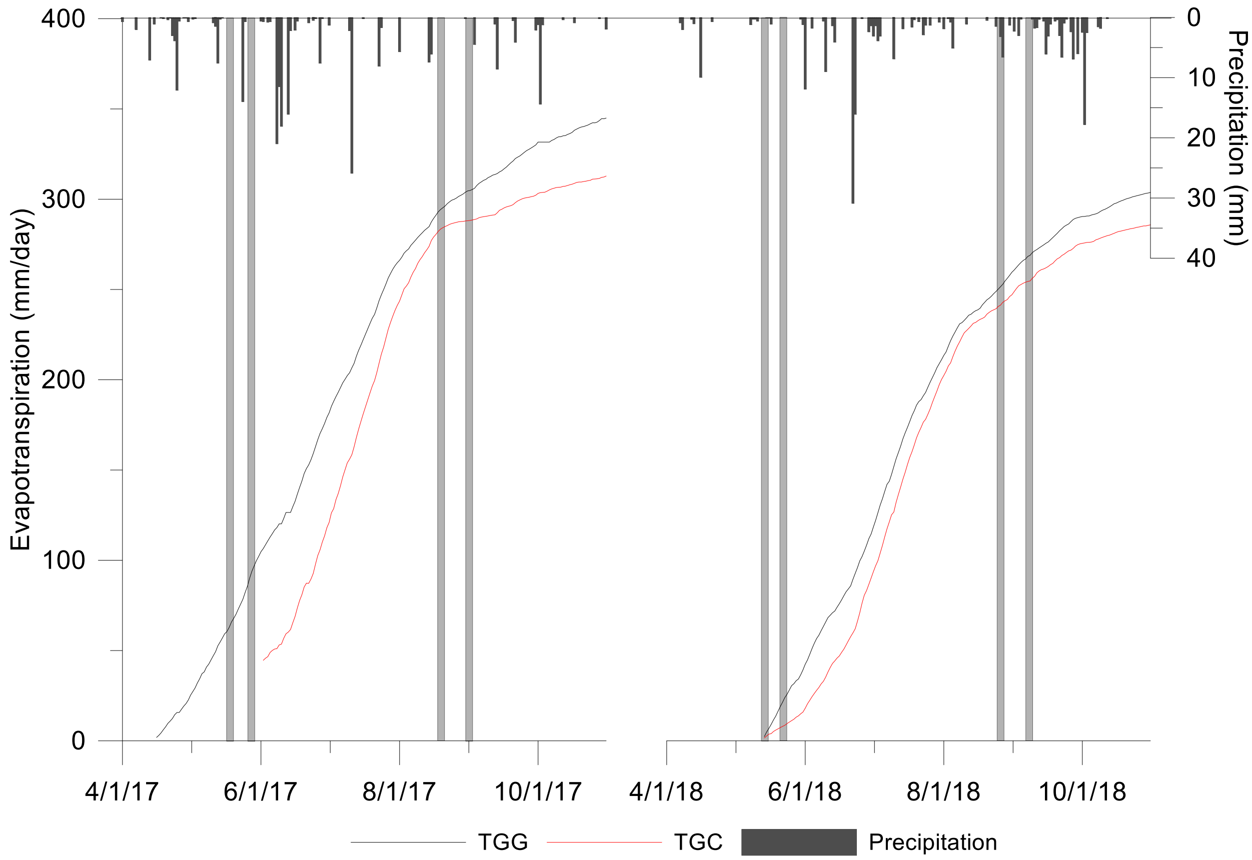

Figure 3.9. Cumulative evapotranspiration and precipitation at TGG and TGC for the 2017 growing season (April 16, 2017 to October 31, 2017) (left) and 2018 growing season (May 14 to October 31, 2018) (right). Eddy covariance weather station was installed at TGC on June 1, 2017. Light grey bars indicate in each year from earliest to latest: seeding date, germination date, maturity date, and harvest date. 2017 ET for TGC was adjusted for estimated ET before the weather station was installed (see Table 3.4)

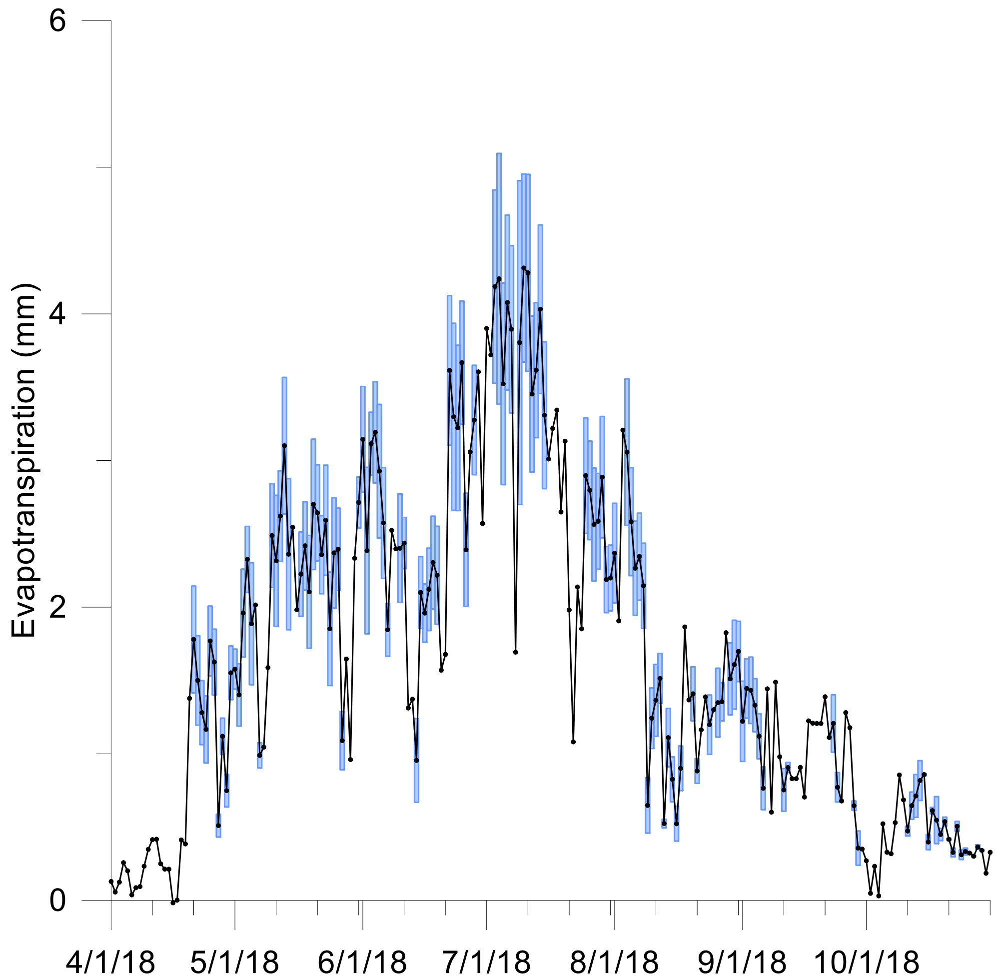

Figure 3.10. Uncertainty (blue bars) for ET measurements (black points) for the 2018 growing season at TGG. Points without bars do not represent days with no error, but rather days where ET was estimated using sensible heat flux and energy balance (E_2).

3.4 Discussion

Snow accumulation showed high intra-site variability, while within sites there was some consistency. The maximum snow depth in the croplands is likely related to the stubble height – in TGC the stubble height of spring wheat ranged from 20-30 cm in the fall, similarly to SH-C24 (alfalfa) and WF (planted with peas in 2017 and spring wheat in 2018). The differences in snow accumulation are somewhat expected, given the different land uses, however it is common for grasslands to have greater snow depths than croplands (Fang and Pomeroy 2009).

At Triple G, the grassland did have a greater snow depth (and snow water equivalent) than the cropland, however WF had a greater snow depth and SWE than C24 and GP. The cause for these differences is likely related to several factors. The SWE at WF has been found to be generally greater than at C24 or GP in the past, which may be due to the fence along the eastern edge of the field and around the weather station in the middle of the field (unpublished data). The greater SWE is unlikely to be due to topography, given the low relief of WF compared to GP and C24. Drift formation at GP is dependent on total snowfall, as a drift formed in 2018, but not in 2019. The orientation of these sites relative to the major wind direction likely plays a part (Fang and Pomeroy 2009), as the primary wind direction is from the southwest, aligning with the depression-upland transects at WF and GP, but not at C24 (Fang and Pomeroy 2009). Grass length may play a part in the lower snow accumulation in GP. The field has not been grazed since 2006, and the grass grows quite long throughout the year. It is speculated that following an initial snowfall in the early winter, the grass is weighed down and becomes much smoother, reducing the surface roughness and snow retention abilities. Further studies into difference of grazed vs ungrazed grasslands in the area would aid in understanding the reduced snow accumulation in the grassland.

Snowpack depletion differences between sites can be attributed to the land use and topography. Snow accumulates more on steeper lee-side slopes in fields with higher relief, and these thicker drifts will thus take longer to melt. With respect to land use, croplands have looser topsoil and bare soil between rows of crop stubble. Soil particles can become entrapped in the snow reducing the albedo and increasing the melt rate (Lapen and Martz 1996), while thinner snowpacks, as observed at TGC compared to TGG, will melt faster by virtue of having less snow. In grasslands, where the ground surface is completely covered and little soil is exposed, the snow is cleaner and retains a higher albedo during the melt period. This has been observed at GP, where there are a few patches of ground in the depression with little vegetation coverage. These regions have less snow cover overall, were occasionally bare during the winter of 2018, and melt first in the spring.

Snowmelt runoff volumes were very different between 2018 and 2019. This is a result of the large difference in both SWE and total winter precipitation between the two years, as well as the occurrence of a midwinter melt in January of 2019. The large snow drift that formed at TGG is likely the cause for the greater runoff ratio in the grassland than the cropland in 2018. Despite the large drift that formed in GP along the slope, there was no runoff. Runoff in this field has decreased following the cessation of cattle grazing in 2006 (Hayashi and Farrow 2014). Aside from TG in 2018, the difference in snowmelt runoff between the fields is as expected, with the croplands having greater runoff ratios than the grasslands (Allison et al. 1990; Scanlon et al. 2005), and perennial alfalfa having less runoff than the annual crop field (van der Kamp et al. 2003; van Dijk 2005).

The cause of increased soil moisture in TGC is primarily evapotranspiration differences between the sites. TGC was found to have lower ET than TGG over the growing season, due to the deeper roots and longer period of green leaves present in perennial grasses (Walker et al. 2002). Most crops have shallow root systems, typically reaching a maximum depth of 1 m at the most, whereas perennial prairie grasses can reach up to 2 m depth (Canadell et al. 1996). The shallower root systems lead to disconnected macropore networks and do not allow for more focused infiltration. In addition, crops are often not planted until fields have slightly dried following the snowmelt ponding period, which can be weeks after grasses begin to grow. The difference in growing season can been seen in the evapotranspiration, where the grassland has much greater evapotranspiration than the cropland (Figure 3.9, Table 3.4). This can be attributed to the deeper roots of the grasses leading to more water uptake from soil moisture and thus more evapotranspiration in the early spring/late fall before the crops are seeded and after the crops are harvested. Greater water content in the fall leads to soils freezing later due to the latent heat stored in the excess water. Warmer soils will reduce snow accumulation early in the season, increasing the near-surface soil moisture content as snow falls and melts immediately.

The greater runoff ratios in the cropland sites are caused by multiple factors. Primary factors affecting snowmelt runoff and infiltration are the amount of snowpack and the antecedent moisture condition in a field (Granger et al. 1984), as well as the presence of undisturbed macropores (van der Kamp et al. 2003; LeBlanc, 2017). TGC was observed to have greater water content and lower macropore density than TGG, although unfrozen infiltration rates were similar (Muenchrath 2019). The similar infiltration rates could indicate greater matrix porosity in the cropland. Greater water contents in the fall can lead to the soil matrix becoming blocked with ice once the soil freezes, reducing infiltrability. TGG, with a greater density of macropores and lower antecedent moisture, would have greater infiltrability during the melt period than TGC.

Midwinter melts over frozen soil can reduce future soil infiltrability and increase runoff ratios. The melted water infiltrates through open pore spaces (matrix and macropores), where it can then re-freeze. If the pore space is filled, the re-freezing of infiltrated water will block it (Mohammed et al. in press). Infiltrated water can cause ice to grow on the sides of larger macropores, reducing the open pore space and thus lowering the infiltration rate.

The interaction between land use and snowmelt infiltration is complex. This complexity is confounded by differences in snow accumulation. While plot-scale studies can be useful to examine some of the small-scale effects of land use on snow accumulation and snowmelt runoff, they can be hindered by the small number of comparisons that can be made. If sites are not extremely similar with regards to topography, catchment size, aspect, and location; land use effects can be obscured by the effects of other factors.

3.5 Conclusions

Snow accumulation and snowmelt runoff processes are complex and dependent on many factors, which can be influenced by land use. A paired-plot site and secondary land-use comparison sites were examined to examine land-use effects on snow accumulation and snowmelt runoff. Generally, the cropland sites had a higher runoff ratio, however, the total runoff volume was not necessarily greater on the croplands. Differences in land cover, vegetation length, soil moisture, and soil temperature can all impact snowmelt runoff. Year-to-year differences in weather, such as snowfall and midwinter melts, caused large variation in runoff between and within sites, which in turn can affect groundwater recharge.

Chapter 4. Applications of infrared remote sensing to estimate snowmelt runoff in the Canadian prairies

4.1 Introduction

Over the past decades, remote sensing has become a common method to estimate open areas of water in a variety of environments. Remote sensing can make use of many different types of data, such as reflected solar radiation or emitted thermal radiation, with this information received from a number of sources, such as satellite and aerial imagery (McFeeters 1996). It utilizes the fact that different surfaces reflect different amounts of light across the spectrum, and these differences in reflectance can be used to classify land use/cover. For detecting open water specifically, one of the most common methods is to use the infrared wavelengths, as water strongly absorbs infrared radiation, while plants, bare ground, and other surfaces strongly reflect it (McFeeters 1996; Frazier and Page 2000).

Open water areas of the Prairie Pothole Region (PPR) have previously been delineated using remote sensing techniques, however, many of the small ephemeral ponds created by snowmelt runoff were missed (Sethre et al. 2005; Rover et al. 2011). This is partly owing to the spatial resolution needed to detect open water in small depressions being too high for freely available satellite imagery (such as Landsat), and other, higher-resolution, satellite imagery being overly costly to acquire for the large areas and multiple days required. Lower-resolution satellite imagery has been used to effectively map larger prairie pothole wetlands that receive groundwater discharge, however other types of wetlands (flow-through wetlands, recharge wetlands, and ephemeral ponds) were less distinguishable (Rover et al. 2011). While there are ways to estimate multiple land covers from a single pixel, these methods can still miss small ponds and can lead to many false positives (Sethre et al. 2005). Another challenge in mapping small ponded depressions is that snowmelt runoff typically occurs over multiple days, and different land covers can have different melt rates (van Dijk 2005). This can pose problems when using satellites with return periods greater than one or two days.

The combination of pixel-size requirements and return period leads to a need for high spatial and temporal resolution to analyze the small ephemeral ponds common in southern Alberta. Aerial surveys are costly, which commonly limits data collection to a single day. Satellite images can be retrieved for a larger number of days more easily, depending on the weather and return period. Improvements to satellite-image availability and resolution make it possible to use these datasets.

As previously described in Chapter 3, snowmelt runoff generation in the Canadian prairies is dependent on several factors, including macropore development, soil type, topography, and antecedent moisture conditions. While it is not possible to easily determine macropore density or antecedent moisture conditions from remote-sensing imagery, topography can be inferred from a digital elevation model (DEM), and soil and surficial geology maps are available for many regions.

This chapter will explore the use of high-resolution satellite imagery in conjunction with a high-resolution DEM derived from light detection and ranging (LiDAR) data to estimate snowmelt runoff volumes in a small (250 km^2) watershed in the Canadian prairies. These runoff volumes will be compared between land covers to examine the effects of land cover on snowmelt runoff. As groundwater recharge in the prairies is primarily driven by the infiltration of snowmelt runoff, these runoff volumes can be used as a proxy to estimate differences in groundwater recharge between land uses.

4.2 Methods

4.2.1 Study Site

Catchments analysed were selected from within the West Nose Creek watershed described in Chapter 2. The region is a patchwork of grasslands and croplands, with land uses previously mapped as part of a previous study in the area (Figure 4.1) (Guha 2007). The depressions that were to be analyzed were chosen based on catchments only containing one pond in the catchment area (i.e. had enough topographic relief for the catchment to be resolved at the scale of the DEM), depressions drained completely following the melt (i.e. were not discharge or flow-through wetlands), and catchment areas did not intersect roads or ditches to avoid complications from preferential flow along these pathways (Figure 4.2). Grassland and cropland catchments near each other were selected based on these criteria. The proximity of the catchments was accounted for to reduce the effects of topography on the results. In total, 17 grassland and 13 cropland catchments were chosen for analysis.

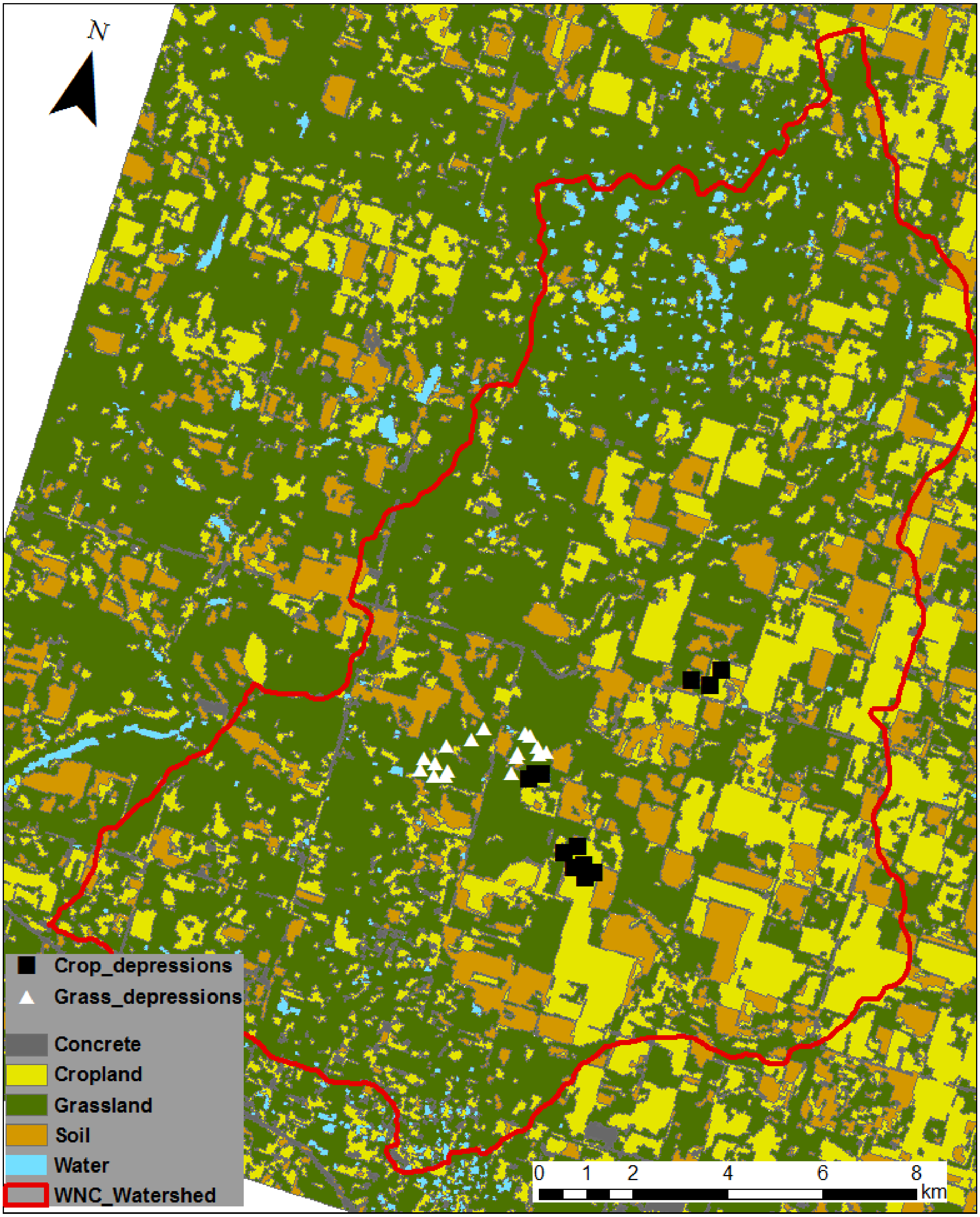

Figure 4.4. Land use map for the West Nose Creek Watershed (outlined in red). Grassland depressions are indicated with white triangles and cropland depressions with black squares.

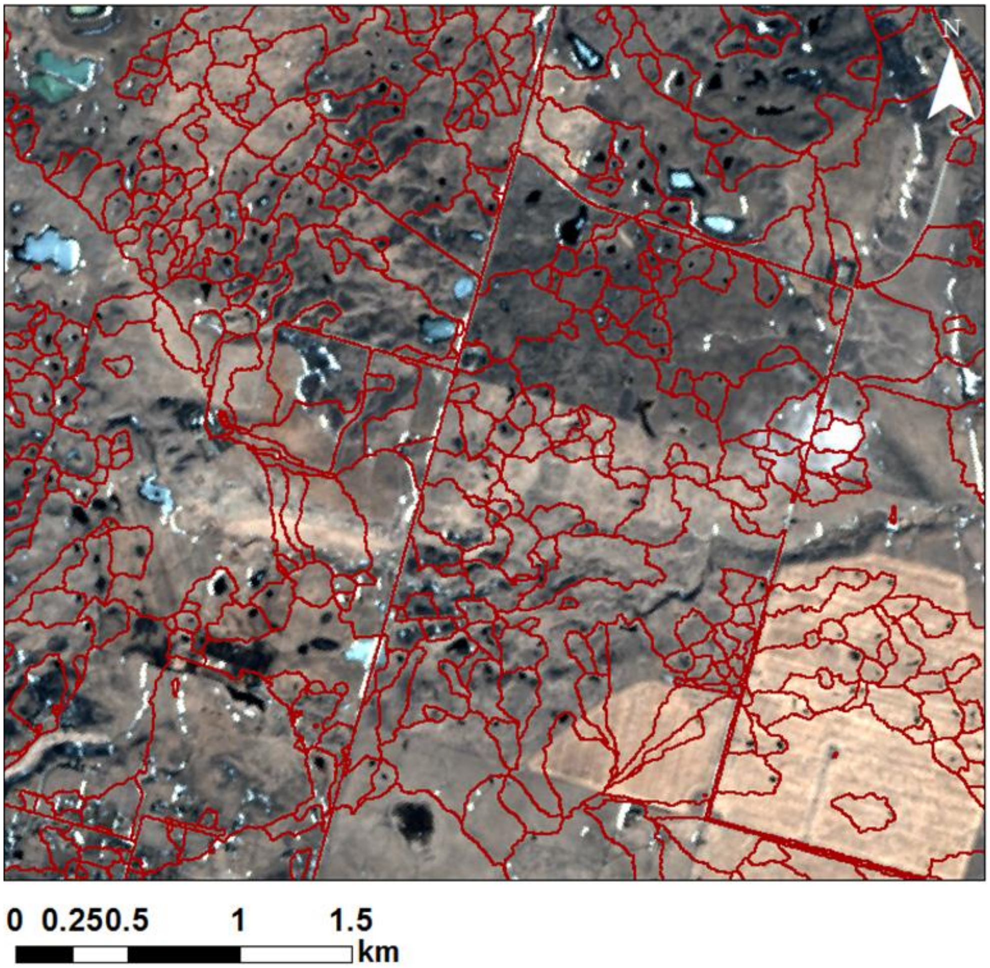

Figure 4.2. False-colour image showing the DEM-delineated catchments (in red) of typical grasslands and croplands in WNC watershed. Dark areas within catchments are open water, and bright regions are snow-covered water. Image from 2017/03/26, retrieved from Planet on 2019/04/18.

4.2.2 Data Sets

A 2-metre horizontal resolution LiDAR elevation survey was previously completed by Rocky View County for the WNC watershed, with a standard deviation of vertical measurements within the cells of 0.224 m. The data from this survey was converted into a DEM, and drainage divides (i.e. catchments) for individual depressions were created using ArcGIS, with each catchment given a unique number between 1 and 20,702 (the total number of depression catchments resolvable at the scale of the LiDAR survey) (Pavlovskii 2019). Depth-area-volume relations were created for each catchment by filling each depression with set heights of water and calculating the resultant area and volume that would be filled (Pavlovskii 2019).

Three aerial infrared photographs were acquired in during snowmelt runoff periods in 2003, 2007, and 2009; and digitized to 0.3-m pixel resolution. Procedures for delineating water-filled depressions were created for the 2003 data covering a limited subarea (*ca*. 30 %) within the watershed, using a combination of manual and supervised image classification schemes (Guha 2007). Similar procedures were applied to the 2007 and 2009 infrared imagery covering the entire watershed.

3-m resolution, 4-band (RGB+NIR) PlanetScope Ortho Scene satellite imagery was downloaded for days during the spring snowmelt periods in 2017, 2018, and 2019. The imagery has been orthorectified, scaled to top-of-atmosphere radiance, and projected to a cartographic projection prior to downloading (Planet Team 2017). Images were taken from days with little to no cloud cover or haze, and from as many dates around the melt period as possible to ensure that the peak runoff was captured.

4.2.3 Data Analysis

The previously delineated water areas from 2007 and 2009 aerial photographs (Matthew Wilson, unpublished data) were included in the comparison. The 2003 flight lines did not intersect all of the chosen catchments and were excluded from this analysis. Areas of ponded water for each depression were extracted from the analyzed aerial imagery using ArcGIS.

A single band approach was chosen to analyze the satellite imagery data, using the NIR band. This method has been successfully implemented to map water bodies in a number of previous studies (e.g., Frazier and Page 2000; Ozesmi and Bauer, 2002). Ponded areas were delineated using visual estimation based on pixel values, coupled with available field observations of pond width for 2018 in ArcGIS. Due to the pixel size, the edges of the ponds are obscured within pixels that are mixed with open water and wet soil. Cut-off values for the infrared imagery were chosen as the halfway point between what was known to be bare ground and open water across a transect of the depression (Figure 4.3). Final areas were chosen based on the maximum ponded area, which occurred on different days based on the land cover each year.

Depth (*h*), area (*A*), and volume (*V*) values extracted from the DEM analysis were used to generate *h-A-V* curves according to Hayashi and van der Kamp (2000) (Appendix A). The pond areas were converted to volumes using these relationships, and volumes were converted to runoff by dividing the volume by the catchment area.

Midwinter melt events were defined for 2007 and 2009 from snow survey and weather data, where periods of temperatures above zero for multiple days and snow surveys showing depleted snowpack were assumed to be one midwinter melt event. 2017-2019 midwinter melt events were counted based on field observations.

Catchment relief was determined using ArcGIS and taken as the difference between the maximum and minimum elevation within each catchment. Pre-freeze water contents were determined based on soil moisture sensors installed at the Spyhill grazed prairie (GP) depression. While not easily applicable across all land uses, these soil moisture values were indicative of a wetter or drier fall. The time of soil freezing and thawing was also defined using these sensors. Snow amounts prior to melt were assumed to be consistent across land uses and were gathered from snow surveys conducted at GP and Woolliams Farm (WF), a cropland site in the WNC watershed.

Runoff was compared between each year using a Mann-Whitney non-parametric test. Parametric tests were not used because the data was not normally distributed, with no transformations used creating a normal distribution (log, square root, square, and inverse transformations were tried).

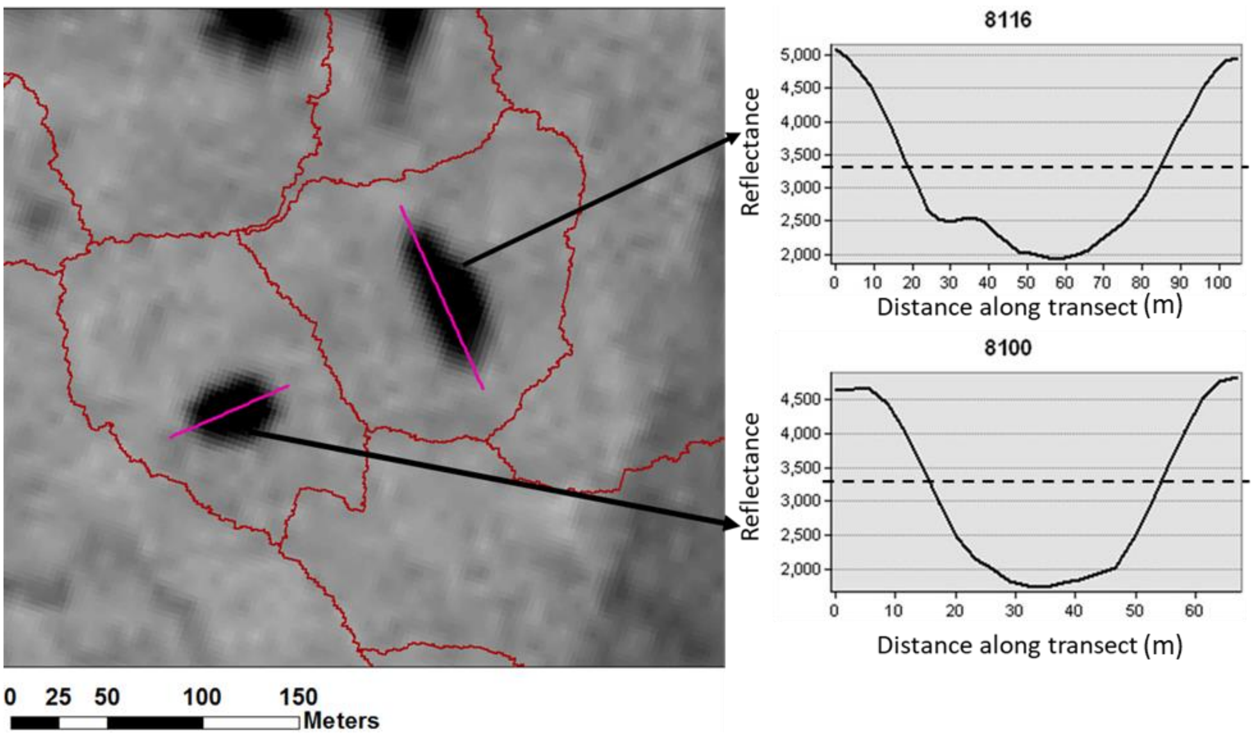

Figure 4.3. Infrared satellite imagery of two analyzed depressions showing the digital number of reflectance along a transect across the ponded area on 2018/04/26. Dashed lines indicate the cut-off value for open water – above was assumed to be wet soil, below open water. Image from Planet, retrieved 2019/02/28.

4.3 Results

The cropland depressions had higher median runoff than the grassland depressions in 2017 and 2018 as calculated using a Mann-Whitney test. There was no significant difference between land covers for any of the other years (Figure 4.4). There was more variation in the cropland runoff values than in the grassland.

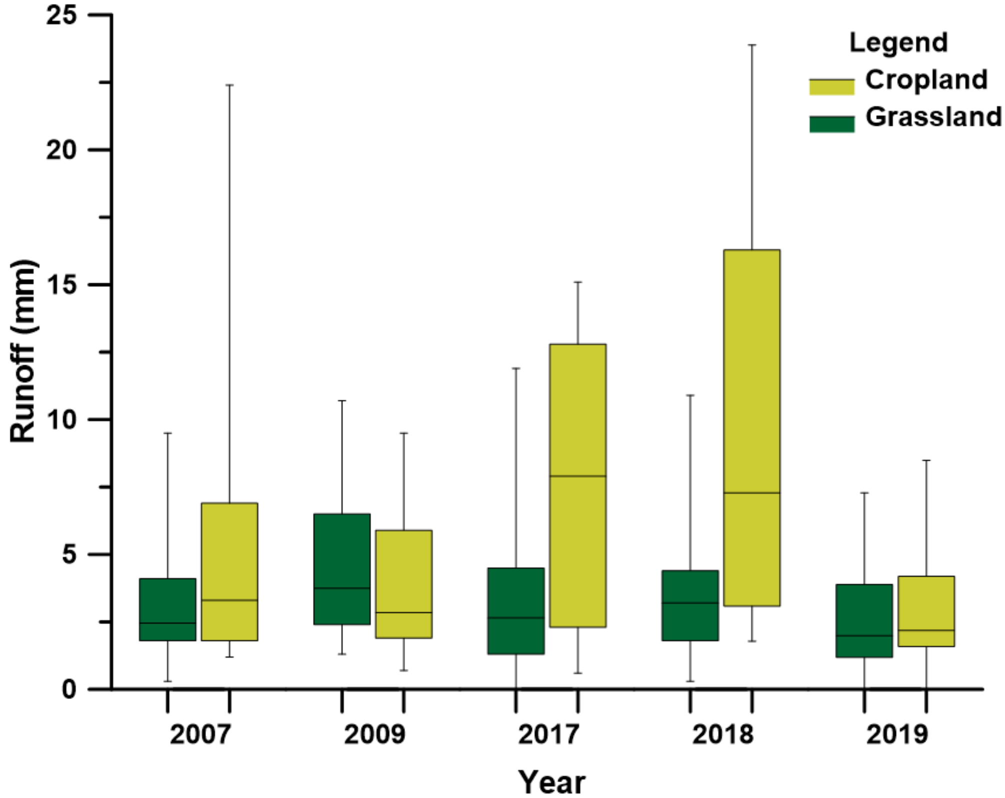

Figure 4.4. Runoff volumes (mm) for the grassland (n=17) and cropland (n=13) catchments. Middle bar is the mean for each year, top and bottom whiskers are the maximum and minimum values, and top and bottom of the box are the upper and lower quartiles for each year.

One of the WF depressions, WF1, was resolvable at the DEM scale and was able to be analyzed using the remote sensing data. The volume of runoff in WF1 calculated using manual water level measurements and higher-resolution manual elevation surveys (using a differentially corrected Global Positioning System, DGPS) agree well, with 2018 runoff values being nearly identical (26 mm as measured in the field, and 24 mm from remote sensing), and 2019 runoff values fairly close (12 mm actual, and 5 mm from remote sensing), although it appears that the remote sensing method slightly underestimates runoff. While there are other monitored sites in the region (a native grassland and an alfalfa field), these sites were not able to be compared. In the case of the alfalfa field, the relief was too low to resolve the different catchment areas from the DEM, and the native grassland did not experience any ponding during the three years of available satellite imagery.

As seen in Figure 4.5, the cropland sites experienced near-complete snowpack depletion (April 22) earlier than the grasslands (April 26) in 2018. This is likely the reason that the estimated cropland average runoff in 2009 is less than the grassland, as the aerial images were taken on a single day, which likely did not correspond to the peak melt day. This was rectified by using multiple days of satellite imagery in the new analysis for 2017-2019.

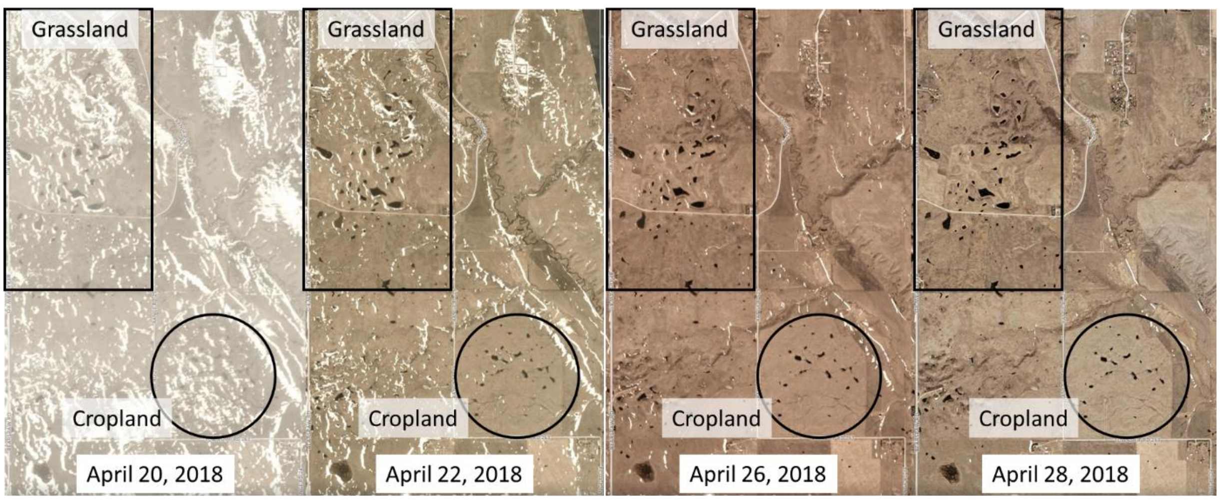

Figure 4.5. Snowmelt over eight days in 2018. The top left of each image is grassland, the bottom right cropland. Images from Planet, retrieved 2019/06/15.

There was no correlation between the amount of runoff generated and the maximum catchment relief, total winter precipitation, or number of midwinter melt events (Figure 4.6). There was also no correlation found between runoff and the SWE prior to melt, pre-freeze water contents, time of soil freezing or thawing, or catchment size (data not shown). The grassland fields, on average, had a greater relief than the croplands (11 ± 8 metres compared to 4 ± 2 metres) (Figure 4.6a), while catchment sizes were generally similar (18 367 ± 14 810 m^2 for the grasslands and 19 266 ± 9 832 m^2 for the croplands).

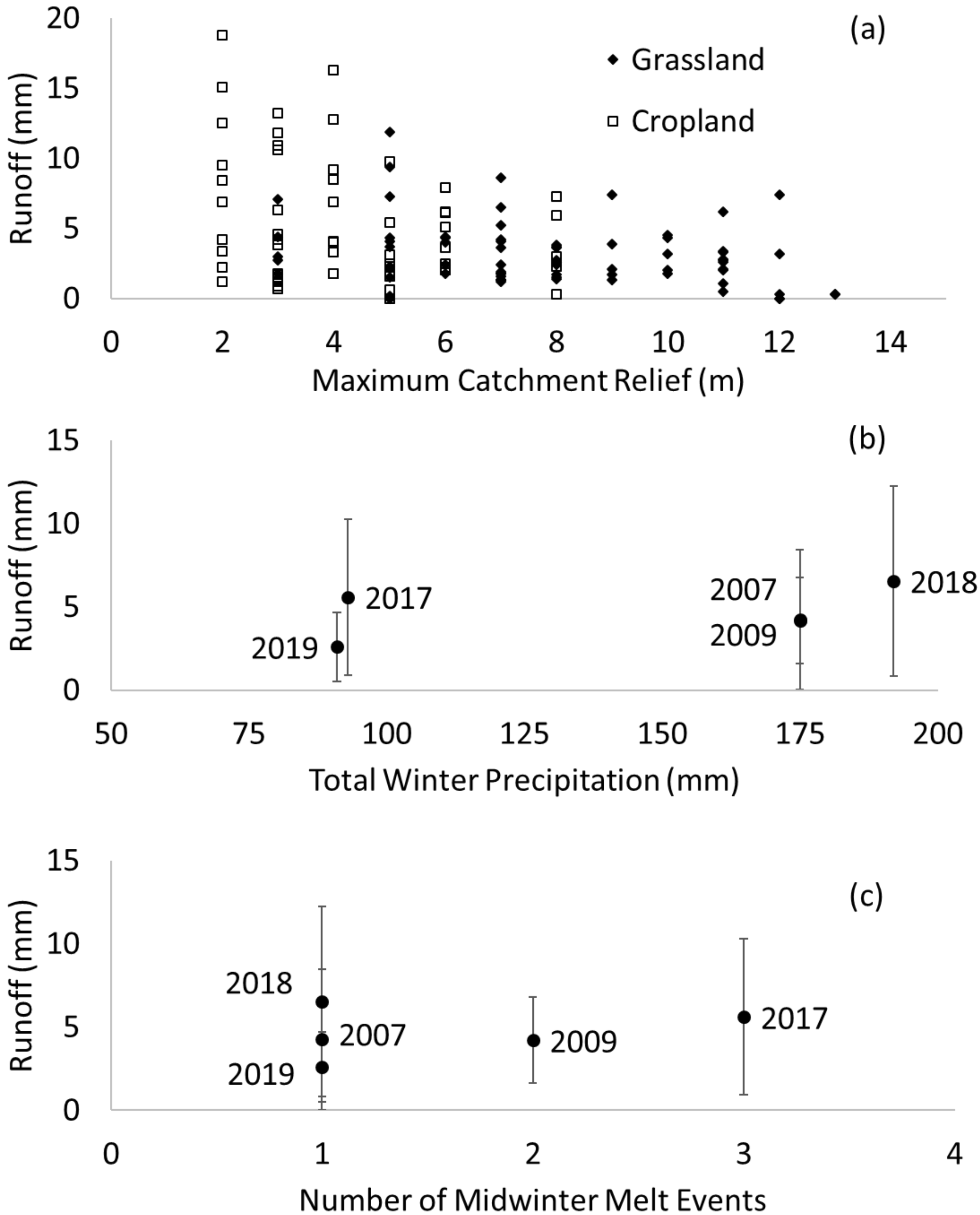

Figure 4.6. Runoff for each year for all land uses compared to (a) catchment relief, (b) total winter precipitation, and (c) number of midwinter melt events.

4.4 Discussion

The greater variation in runoff volumes in the cropland catchments can be attributed to a variety of factors, such as topography, stubble height, and crop type. Because it was not possible to differentiate crop types from satellite imagery, it is possible that some of the crop fields could be alfalfa or other perennial grasses cut for hay, which can respond similarly to grass fields with respect to macropore creation and more infiltration of snowmelt water. The quantity of runoff within a single catchment between years was generally consistent, a pattern that was also observed in a previous snowmelt runoff study in the area (Hayashi and Farrow 2014).

Differences between the manual DGPS and pond depth results and remote sensing survey at WF can be attributed to a few factors. One of the biggest sources of error in the remote sensing method is the inability to account for infiltration of ponded water during the melt period. While infiltration rates are generally small while soils are frozen, they can be on the order of a 10-20 mm per day (Granger et al. 1984; Hayashi et al. 2003). The estimation of the ponded area is less accurate than measurements of water heights from either a water level logger or time-lapse camera image.

It was not possible to differentiate between grazed and ungrazed grasslands from the satellite imagery and land-use map. This could be important for variations in grassland runoff, as grazing compresses the surface, reduces infiltrability, and thus increases runoff (Fiedler et al. 2002). There are very few ungrazed grasslands in the WNC watershed, however, a monitored depression located just outside of the WNC watershed was converted from grazed to ungrazed in 2006 and has generated little to no runoff since (Hayashi and Farrow 2014; Pavlovskii 2019).

When comparing runoff values, a common practice is to normalize the volume of water ponded to the snow water equivalent (SWE) in the catchment, called the runoff ratio. These values are useful particularly when comparing different land uses as there are often different amounts of snow on each field. Normalizing the runoff to each catchment's SWE removes this variability from affecting comparisons. Snow retention is dependent on grass length in grassland fields, and stubble height and crop type in cropland fields (longer stubble can capture more snow), as well as the more general slope height, wind speed, and orientation for all fields (leeward slopes frequently accumulate snow, while windward slopes have little) (Fang and Pomeroy 2009). While grasslands typically retain more snow than croplands, and both more than fallow fields, tall stubble can be as effective as grass for retaining snow (van der Kamp et al. 2003). It was not possible to determine the runoff ratio for the different land uses in this study, as there were not enough field snow surveys completed to generalize SWE across multiple land uses. Snow surveys completed for other studies have shown that there is high variability in the snow retention across land uses within the WNC watershed, with the cropland having the most snow, then the alfalfa field, then the grassland (see Chapter 3).

There are limitations to using a single-band approach to estimate the area of ponded water, largely in that it is subjective, and different analysts could choose different cut-off values to delineate the edges of ponds. However, it was not possible to use a multi-band approach, such as the normalized difference water index (NDWI), to estimate pond areas. The NDWI was first created to reduce bias in manually delineating open water and saturated soil areas/vegetation, and involves normalizing the difference between the green and infrared bands (Gao 1996; McFeeters 1996). However, due to the high turbidity of the ponds and lack of green vegetation, this method failed to distinguish between water and saturated soil.

The dataset was also limited in the ability to measure the ponded area and depth-area-volume curves due to the spatial resolution. The satellite imagery has a pixel size of 3 m, leading to the smallest area that can be resolved being 9 m^2. This 3 m edge to each pixel also obscures the edges of the ponds. The LiDAR data used for the depth-area-volume relationships have a resolution of 2 m horizontally and a vertical resolution of 0.224 m. This limitation is particularly evident in low-relief fields where multiple catchments are amalgamated into one large catchment with multiple depressions. This renders the catchment areas useless for this method of analysis and limits the number of usable ponds.

Future work on this subject could include creating a supervised classification scheme for the NIR band that considers the location of local minima in each catchment to calculate pond area. This would allow for the automated picking of areas while excluding regions of wet soil. Modelling the snow distribution throughout the watershed could allow for estimates of SWE and thus runoff ratios, allowing for unbiased comparisons between land uses.

4.5 Conclusions

Cropland fields trended towards having greater snowmelt runoff than grassland fields within the West Nose Creek watershed. Because groundwater recharge in the region is reliant on the infiltration of ponded snowmelt runoff, it is likely that there would be greater groundwater recharge beneath the croplands as well. The difference between land covers is likely due to the properties of the near-surface sediments, such as antecedent moisture conditions and number and connectivity of macropores.

Using high-resolution satellite imagery is a viable way to estimate the amount of snowmelt runoff in temporally and spatially variable environments. Future work to generate classification schemes for automated area generation would allow for larger areas to be examined. Coupling this procedure with a snow accumulation model could allow for estimations of SWE, and runoff ratios to be calculated for each field. As higher-resolution imagery becomes more inexpensive and available, estimations of runoff will continue to improve.

Chapter 5: Estimating land use effects on short-term groundwater recharge

5.1 Introduction

The Canadian prairie region frequently experiences dramatic differences in weather year to year. The weather differences can cause considerable variability in the quantity of groundwater recharge, depending on the snowpack and other factors as mentioned in Chapters 3 and 4. Errors associated with small-scale short-term measurements, such as evapotranspiration and soil moisture, can be greater in magnitude than the actual value of groundwater recharge. Thus, to determine the average groundwater recharge for a region, either very long-term data collection, larger-scale estimates, or aggregating approaches are required.

The electrical conductivity of the subsurface can be used to infer zones where groundwater recharge may be occurring. High salinity or high moisture content will cause higher conductivity, while leached or drier soils will have lower conductivity (Brus et al. 1992; Doolittle and Brevik 2014). Depressions typically have low-conductivity relative to the surrounding areas, as the centre will be leached from the infiltration of ponded snowmelt water while sulphate salts accumulate around the depression (Hayashi et al. 1998). Once depression-focussed recharge has been confirmed, a more detailed study into the quantity of groundwater recharge is possible.

Geophysical methods can provide effective tools to gain knowledge about the subsurface conductivity for depths ranging from a few to hundreds of metres. A common method to image the near subsurface is the use of electromagnetic (EM) terrain conductivity meters, which have a depth of investigation of up to 6 metres (Geonics 2013; Hayashi et al. 1998). These devices measure the near-surface electrical conductivity, which is related to dissolved ions, water content, temperature, and soil type (Brus et al. 1992; Doolittle and Brevik 2014).

The water table fluctuation (WTF) method has been applied in a variety of environments to estimate groundwater recharge, generally resulting from single precipitation events (Scanlon et al. 2001; Healy and Cook 2002; Crosbie et al. 2005). This method is usually applied to short-term (<1-10 day) fluctuations of groundwater level in shallow aquifers that respond quickly to precipitation. The ponding of snowmelt runoff water in the prairies causes a similar increase in the groundwater level, albeit over a longer time period (>5-10 days). With measured head changes during the event and an appropriate estimate of specific yield, it is possible to apply this method to water table increases due to the infiltration of ponded snowmelt runoff, with the assumption that all flow is vertical. As the water table fluctuation method is event-based, it neglects any processes that occur after the recharge event, such as evapotranspiration.

A common time-aggregated groundwater recharge estimation technique in semi-arid regions is the chloride mass balance (CMB) method (Allison and Hughes 1983; Scanlon et al. 2006). The CMB method utilizes chloride concentrations in the pore-water compared to chloride inputs from the land surface to estimate the quantity of groundwater recharge. This method requires knowledge of the chloride inputs in a system, including precipitation, lateral transport, and anthropogenic inputs (Allison and Hughes 1983; Allison et al. 1994; Pavlovskii et al. 2019b). While precipitation inputs are generally constant, chloride cycling between the uplands and depressions causes lateral flow of chloride in both directions. Anthropogenic inputs can include road salt, fertilizers, or, particularly in grazing pastures, salt blocks, among others. Tritium (^{3}H) isotopic dating methods can be used to determine if the chloride concentrations in the pore-water profiles are likely from younger or older groundwater (Allison and Hughes 1983).

Stable isotopes of water (^{18}O and ^{2}H) can be used to determine whether groundwater is likely sourced from summer or winter precipitation, or a mixture of both (Allison and Hughes 1983; Maule et al. 1994). The isotopic composition of precipitation varies seasonally, with winter precipitation being more negative (i.e. depleted in heavier isotopes) than summer. Isotope profiles have been used to define hydrologic units in glacial tills, with different hydrological units showing distinct isotopic signatures (Hendry et al. 2004). Isotopes can also be used to determine if recharge is diffuse or depression-focussed, as the latter case will have an isotopic signature beneath the depressions more similar to snowmelt, while the uplands will be more similar to the mean annual isotopic signature (Pavlovskii et al. 2018). If the profiles beneath uplands and depressions are similar, diffuse recharge may be occurring, and similar chloride and sulphate concentrations in upland and depression pore-water profiles would be observed.

If a local meteoric water line (LMWL) is available, pore-water isotope compositions can be converted to the line-conditioned excess (lc-excess, ‰), which shows deviation of an isotopic sample from the LMWL (Landwehr and Coplen 2004). This method can indicate whether water has been evaporatively enriched, or, if the water originated from a different climate with a different slope or intercept to the modern LMWL.

The proportion of groundwater likely sourced from summer or winter precipitation can be determined using stable isotopes using a mixing method (Maule et al. 1994). This method utilizes the two end members of precipitation (snow and rain) and the measured isotopic composition of groundwater to determine the fraction from rain or snow.

The purpose of this chapter is to compare methods of estimating groundwater recharge in the prairies, and to use those methods to estimate shallow groundwater recharge beneath two land uses. The importance of aggregating groundwater recharge estimations is examined.

5.2 Field and Laboratory Methods

5.2.1 Study Site Investigation and Sampling

Data were gathered from the cropland and grassland sites at Triple G (TGC and TGG), described in detail in Chapter 2, with most of the data coming from samples collected from boreholes drilled and piezometers installed at the two sites. Boreholes were drilled at both locations on different dates. The boreholes in TGG were drilled in November 2014 using a 15 cm diameter solid-stem auger at two upland and one depression location (Chapter 3, Figure 3.2c), and sediment samples were collected using an auger-wrap technique roughly every 0.75 m up to 15 m in depth in the upland and 12 m in the depression (Pavlovskii et al. 2018). These samples were then stored in sealed glass jars until analysis. They were weighed following collection and immediately before subsamples were removed for analysis to determine if evaporation had occurred.

The boreholes in the cropland site were drilled in June 2017 using a 15-cm diameter hollow-stem auger, using a split spoon sampler. Samples were collected from the unconsolidated material in the split spoon sampler every 0.3 m for the first 2 m, and then every 0.7 m thereafter to a depth of 14 m in the upland and depression boreholes (Chapter 3, Figure 3.2a). Two samples were taken from each depth with one stored in a sealed glass jar for pore-water chloride and isotope analysis, and the other used for bulk density and grain size analysis. These samples were also weighed following collection and before analysis to determine the amount of mass loss due to evaporation that may have occurred during storage.

Piezometers were installed in the upland and depression locations at each site, with screen depths lengths indicated in Table 5.1. All piezometers had a 2.54 cm diameter PVC casing, except for the 3 m depression piezometer at TGG, which was 1.27 cm in diameter.

Sandpacks were added around the screened sections, and the borehole annulus in each well was sealed with bentonite chips. The cropland piezometers were developed using a surge block, and the effectiveness was determined by comparing hydraulic conductivity measurements from slug tests before and after development. Information on all piezometers is in Appendix E.

Table 5.1. Piezometer locations, depths (m), and screen lengths (m) for TGG and TGC

Site	Location	Depth to Bottom of Screen (m)	Screen Length (m)
TGG	Upland	15.2	1.5
	Depression	12.2	1.5
	Depression	7.3	1.5
	Depression	3.0	0.76
TGC	Upland	13.7	1.5
	Upland	7.6	1.5
	Depression	13.7	1.5
	Depression	7.6	1.5
	Depression	4.6	1.5

Unvented pressure transducers (Solinst, Levelogger Edge M5) were installed in all piezometers and set to record water level and temperature every 30 minutes. A barometric pressure logger was installed at the cropland site and used to barometrically correct water level data for both sites. Prior to April 2018, vented pressure transducers (In Situ Inc, miniTroll) were installed in the 15 m upland piezometer and the 8 m and 14 m depression piezometers at TGG.

Due to the low hydraulic conductivity (on the order of 10^{-7} to 10^{-10} m s^{-1}) of sediments at the sites, most groundwater samples were taken without pre-purging by dropping a 1 m long PVC bailer (either 2.5 cm or 5 cm diameter, depending on piezometer casing diameter) into the screened interval and collecting the water contained within. This was not the case for the 8 m depression piezometer in the cropland (in sand) and the 14 m upland piezometer in the cropland (in sandstone). These two piezometers had a fast-enough response to allow for the purging of three well volumes prior to sampling using a peristaltic pump. Hydraulic conductivity for the sand and sandstone formations around these two piezometers was 10^{-6} m s^{-1}. 250 mL plastic sample bottles were filled completely and transported in an ice-filled cooler to the laboratory, where they were stored in the fridge before either isotopic or chemical analysis could be completed. Samples were filtered in the laboratory before analysis using 0.45 µm cellulose-nitrate syringe filters.

Ponded water samples were collected from each site during the ponded period to determine the lateral chloride flux by snowmelt runoff. Samples were taken at regular intervals (every 1-2 weeks) while the depressions were ponded in the spring in 125 mL or 250 mL plastic bottles. Sample bottles were filled with no headspace, stored at 4°C, and filtered prior to for analysis.

A terrain conductivity meter (Geonics, EM-31) was used to survey the electrical conductivity of the top 3 to 5 metres of the subsurface. Measurements were taken every 5-10 metres laterally across the entire field. The grassland EM-31 survey was completed on November 9, 2014 and the cropland survey on June 1, 2017.

5.2.2 Sample Analysis

The pore-water isotopic composition was determined by taking small subsamples from jarred soil samples and placing them in 12 mL glass vials alongside a special platinum catalyst (Hokko beads), following the procedure described in Koehler et al. (2000). The Hokko beads serve as a catalyst for the hydrogen isotope measurements. The vials were quickly sealed and equilibrated with carbon dioxide (CO_2) gas for ten minutes. The samples were left to equilibrate for 24 hours, then analysed using an isotope-ratio mass spectrometer (IRMS) (Thermo Finnigan Delta V with Gasbench) for oxygen isotope ratios. Next, hydrogen (H_2) gas was added to the vials in the same way as the CO_2 gas, with the samples left to equilibrate for another 24 hours, and then analysed on the same IRMS, giving the hydrogen isotope values. Standards with known isotopic composition were inserted after every seven samples to correct for any drift in the machine. The accuracy of this method is 0.25 ‰ for $\delta^{18}O$ and 2.0 ‰ for $\delta^{2}H$ (Stephen Taylor, University of Calgary, personal communication). Pore-water isotope results were discarded if there was more than 5% evaporation before analysis, as determined by the weight loss during storage (see above).

Snow, pond water, and groundwater samples were analysed for stable isotopes by first filtering the samples through 0.45 μm cellulose-nitrate filters and then analysing on an off-axis integrated cavity output spectroscopy (OA-ICOS) laser absorption spectrometer (Los Gatos Research, Liquid Water Isotope Analyzer), with an accuracy of 0.1 ‰ for $\delta^{18}O$ and 1.0 ‰ for $\delta^{2}H$ (Steven Taylor, University of Calgary, personal communication).

Pore-water anion concentrations were determined following the procedure described in Parsons et al. (2004). Approximately 100 g of soil were added to a 250 mL Erlenmeyer flask followed by approximately 120 mL of deionized water. The samples were covered to prevent evaporative loss during shaking and shaken for four hours on an orbital shaker. The liquid was then centrifuged and resulting supernatant filtered through a 0.45 μm cellulose nitrate filter. The filtered water was analysed using an ion chromatograph (Metrohm, 930 Compact IC Flex). Groundwater and pond water samples were first filtered through 0.45 μm cellulose nitrate filters, then analysed using an ion chromatograph (Metrohm, 930 Compact IC Flex).

A sample of fertilizer applied to the cropland field was analysed for chloride concentration. 20 grams of fertilizer was dissolved in 2 litres of deionized water, with the resulting solution filtered through a 0.45 μm cellulose nitrate filter and analysed using an ion chromatograph (Metrohm, 930 Compact IC Flex).

Water samples from piezometers in both the cropland and grassland were analysed for tritium content at the University of Waterloo Environmental Isotope Laboratory by first enriching the samples using electrolysis and then using the liquid scintillation counting method. The detection limit using this method was 0.8 Tritium Units (TU).

5.3 Data Analysis

5.3.1 Water Table Fluctuation

The water table fluctuation method (Healy and Cook 2002) was used to estimate groundwater recharge beneath the two depressions from snowmelt runoff ponding in 2018 and 2019 and following a heavy rainfall event in June 2018 using:

$$R = \Delta h \times S_y \tag{1}$$

where

R (m) is recharge,

Δh (m) is the change in head over the recharge event,

S_y (-) is the specific yield

The difference between the pre-ponding and peak water level during the ponding period was used as the change in head, and 0.11 was used for the average specific yield for clay till, based on analysis of soil samples from TGC (Appendix B).

5.3.2 Chloride Mass Balance

Recharge calculations using the chloride mass balance use (Pavlovskii et al. 2019b):

$$R_{dep} = \left(PC_P + Q_{in} + Q_{lat}A_{upl}/\, A_{dep}\right)/C_{dep} \tag{2}$$

where

R_{dep} is the depression focussed recharge rate (m y^{-1}),

P is annual precipitation in m,

C_P is the concentration of chloride in precipitation (g m^{-3}),

Q_{in} is the annual anthropogenic chloride deposition rate (g m^{-2} y^{-1}),

Q_{lat} is the lateral chloride transport rate from the uplands to the depression (g m^{-2} y^{-1}),

A_{up} is the area of the upland region in each catchment (m^2),

A_{dep} is the maximum area that could pond in the depression (m^2),

C_{dep} is the chloride concentration in the pore-water (g m^{-3}).

If Q_{in} and Q_{lat} are much greater than the precipitation deposition rate, the precipitation term can be ignored (Pavlovskii et al. 2019b). When the mass balance over a long time period (e.g., > 10^3 years) prior to agricultural activity (i.e. Q_{in} = 0) is considered, the chloride cycle within a depression-upland catchment reaches a quasi-steady state (Hayashi et al. 1998b). As such, a simpler form of equation can be used to estimate catchment-scale recharge (R_{cat}):

$$R_{cat} = PC_p/C_{gw} \tag{3}$$

where

C_{gw} (g m^{-3}) is the average groundwater chloride concentration in the catchment (Pavlovskii et al. 2019b).

5.3.3 Line-Conditioned Excess

Line-conditioned excess (lc-excess) was calculated for the pore-water extracts using the coefficients of the Calgary LMWL (Peng et al. 2004), in the lc-excess equation as defined by Landwehr and Coplen (2004, Eq. 2):

$$d_{lc} = (\delta^2H - a\delta^{18}O - b) \tag{4}$$

where

d_{lc} is the lc-excess

a is the slope of the LMWL (7.68 for Calgary),

b is the intercept of the LMWL (-0.21 ‰ for Calgary),

5.3.4 Binary Mixed Isotope Fractions

The binary end-member analysis of isotopes involves the use of a mass-balance equation (Pavlovskii et al. 2018):

$$f = (C_m - C_2)/(C_1 - C_2) \tag{5}$$

where

C_m is the measured isotope ratio in the sample,

C_1 is the isotopic composition of winter precipitation,

C_2 is the isotopic composition of summer precipitation,

f is the fraction of the sample that is contributed by the winter precipitation end member.

For this study, C_1 was -24.02 ‰ and C_2 was -14.76 ‰ for $\delta^{18}O$, which are the volume-weighted means for winter (November to April) and summer (May to October) precipitation for Calgary from Peng et al. (2004).

5.3.5 Uncertainty Analysis

The errors associated with the water table fluctuation method are primarily a result of the uncertainty in estimating the specific yield value used for calculations. Other sources of error in the WTF method include the assumption of vertical flow and little to no background recession occurring during the infiltration, and the use of a single piezometer to represent the field.

The applicability of this average specific yield value was examined by using soil water retention curves for TGC soil samples at 1 m and 1.5 m (Appendix B). These curves were used to estimate van Genuchten parameters, and a static S_y was calculated for each according to Cheng et al. (2015, Eq. 15). These values ranged from 0.068 in the deep depression sample to 0.21 in the deep upland sample, although it should be noted that the soil in the upland sample had more sand than the depression sample. Because of this, the range of values of 0.06 to 0.16 were used to capture the expected range of S_y values for the depression. This range encompasses the average specific yield of 0.083 determined for four samples in a clay till at another site near Lethbridge, Alberta (Kyte, 2018).

The error in the chloride mass balance was calculated assuming that the variance in chloride concentration in the pore-water and Q_{lat} are independent. Errors associated with measuring Q_{lat} were calculated assuming that the error was proportional to the errors calculating the runoff volume, or a maximum of ±8% (Chapter 3). The error for each recharge estimate was calculated as (Kallner 2014)

$$\delta R_{dep} = R_{dep}\sqrt{\left(\frac{\delta[Cl]}{[Cl]}\right)^2 + \left(\frac{\delta Q_{lat}}{Q_{lat}}\right)^2} \tag{6}$$

where

δR_{dep} is the uncertainty associated with the depression-focussed recharge rate (m),

$\delta[Cl]$ is the uncertainty associated with pore-water chloride concentrations (g m $^{-3}$),

δQ_{lat} is the uncertainty associated with the lateral chloride flux (g m^{-2} y^{-1}),

R_{dep} is the magnitude of the depression-focussed recharge rate (m),

$[Cl]$ is the average pore-water chloride concentration (3 mg L^{-1} based on the range of concentrations of chloride observed in groundwater samples over time),

Q_{lat} is the magnitude of the lateral chloride flux (mg m^{-2} y^{-1}).

5.4 Results

5.4.1 Subsurface Investigations

Drilling at the grassland site showed that there was only oxidized clay till beneath both the uplands and depressions (up to 15 m below ground surface), the cropland site had a sand layer starting at approximately 3-4 m below ground surface to a depth of 10 m confined by clay till units above and below (Figure 5.1). A sandstone unit was encountered at approximately 14 m depth in the upland. Based on the hydraulic conductivity of the formation around the 14 m depression piezometer (~10^{-10} m s^{-1}) and the sediments observed on the auger blades of the drill, it is assumed that the missing 2.5 m of core at the bottom of the depression borehole are a clay unit.

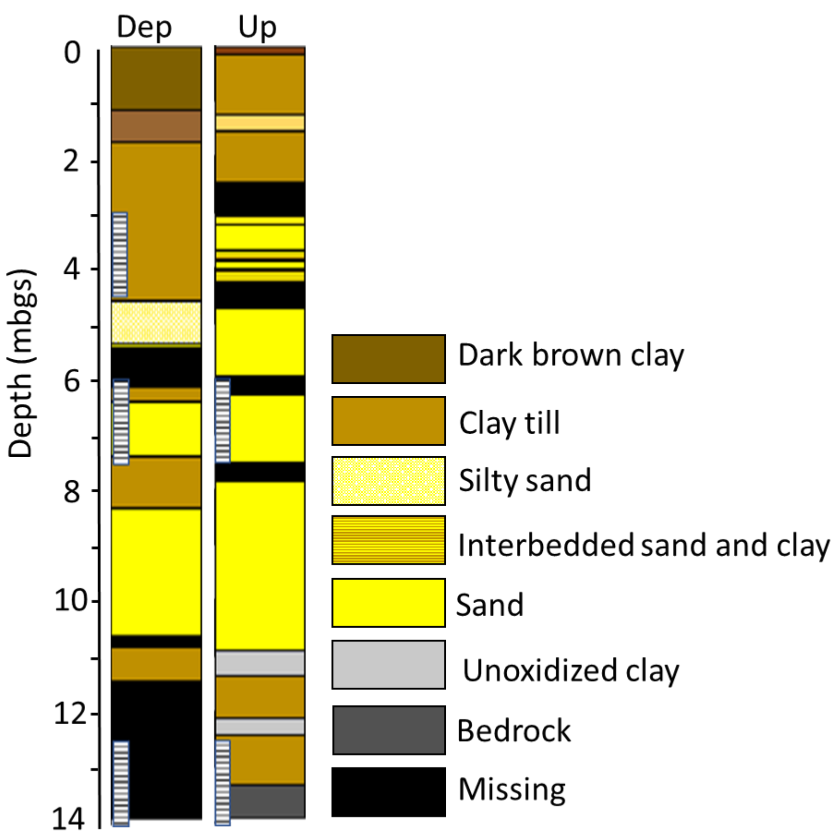

Figure 5.1 Lithology of TGC depression (left) and upland (right). Piezometer screened intervals are indicated by small dashed rectangles.

Zones of high electrical conductivity were observed beneath the depressions in the grassland site (Figure 5.2a), possibly indicating increased water content at this location relative to the rest of the field, as the survey was completed on November 9, 2014 following the growing season, but before the soils froze (Figure 5.5a). Soil volumetric water content following the growing season in this field typically drops below 0.15 (Chapter 3, Figure 3.6b,d). Conversely, the survey in the cropland was completed soon after seeding in June 2017, when the field was wetter from snowmelt infiltration and early spring rainfall (Figure 5.5b). There is a zone of low conductivity in the southeast portion of the cropland, which is likely due to lower water content in the (relatively) higher elevation region of the field. The sand layer beneath the upland was also observed to be closer to the surface in the southeast region in an electrical resistivity tomography survey, which would influence the bulk conductivity of the top 3-5 m of sediment (Appendix C).

5.4.2 Water Chemistry and Isotope Composition

At the grassland, a water sample from the 14 m piezometer contained measurable amounts of tritium, but the 8 m piezometer did not (Figure 5.3a). The elevated tritium and chloride concentrations in the 14 m TGG depression piezometer are assumed to be due to preferential flow path or problems with piezometer construction (chloride concentrations were over ten times greater than pore-water extracts) (Pavlovskii et al. 2019b). Tritium was detected in the upper clay till layer and sand layer in the cropland site (Figure 5.3b). The bedrock and deeper clay layer did not contain detectable amounts of tritium. The low tritium samples in the grassland correspond to low chloride concentrations, however chloride concentrations were similar for all cropland samples.

Chloride profiles for the pore-water chloride extracts at both upland and depression locations in the grassland and cropland were created (Figure 5.4). The depression profiles at both locations had significantly less chloride than the uplands. A chloride “bulge” is present in the upland profiles at both sites, where the chloride concentration increases dramatically before decreasing again. In the cropland, the upland pore-water chloride concentrations decrease at depth to values similar to those found in the depression in the sand layer. The grassland depression chloride concentrations decrease to *ca*. 4 mg L^{-1} below 5 m depth and were below the detection limit below 9.5 m.

Chloride concentrations in groundwater samples are similar to the pore-water chloride concentrations over the screened intervals of the piezometers samples were taken from. For example, in the cropland depression, the pore-water chloride concentration over the screened interval at the 4 m piezometer ranged from 9-14 mg L^{-1}, while the groundwater samples ranged from 12-19 mg L^{-1}. The greatest difference between groundwater and pore-water concentrations was in the 8 m upland piezometer, where the pore-water chloride concentration ranged from 26-35 mg L^{-1} over the screened interval but the groundwater concentration was 41 mg L^{-1}.

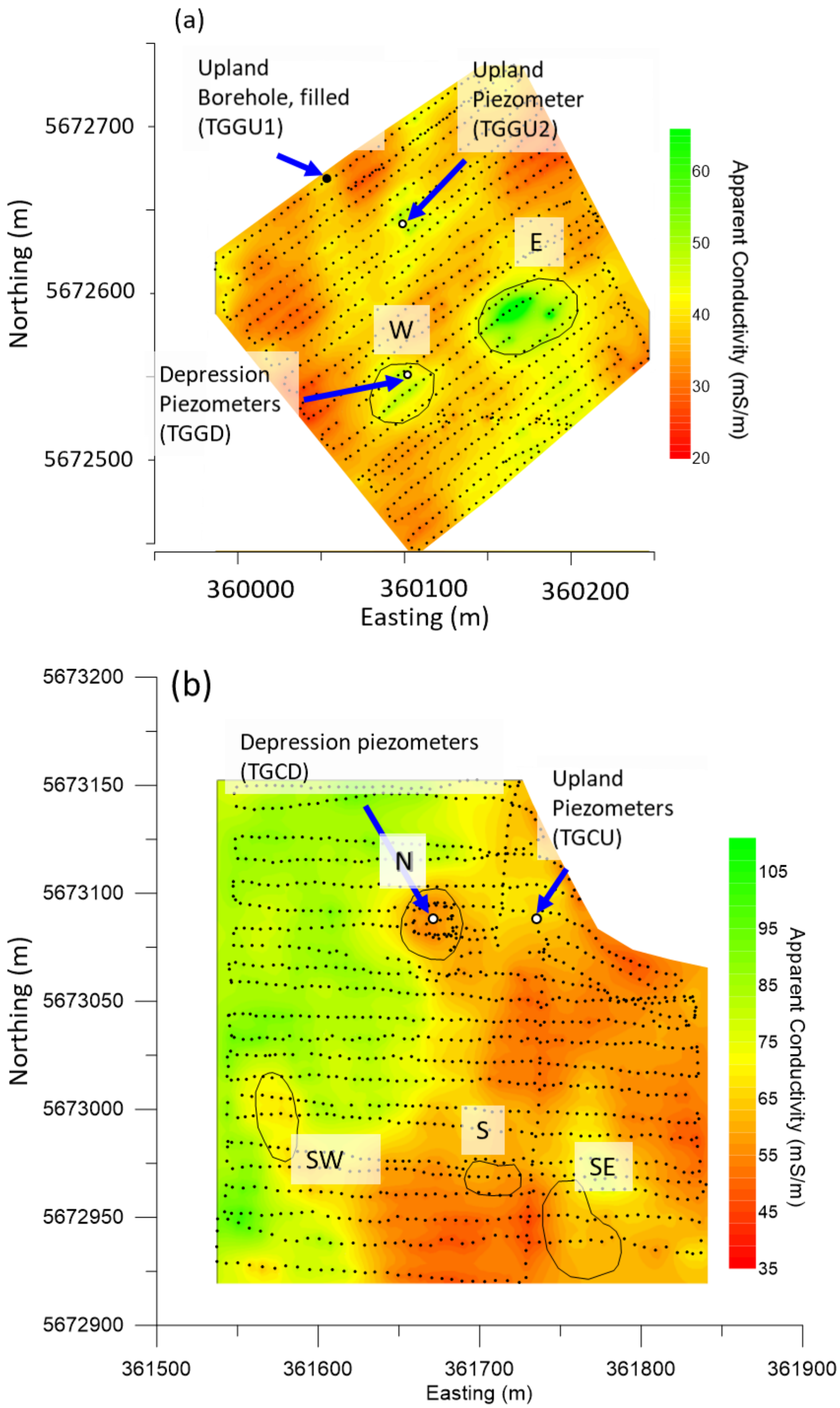

Figure 5.5. Distribution of apparent electrical conductivity in (a) grassland and (b) cropland. Maximum ponded areas in the depressions are indicated. Small white dots represent the locations or boreholes, and small black dots represent conductivity measurement locations. Data is projected using the NAD 1983 datum and is in the UTM Zone 12N.

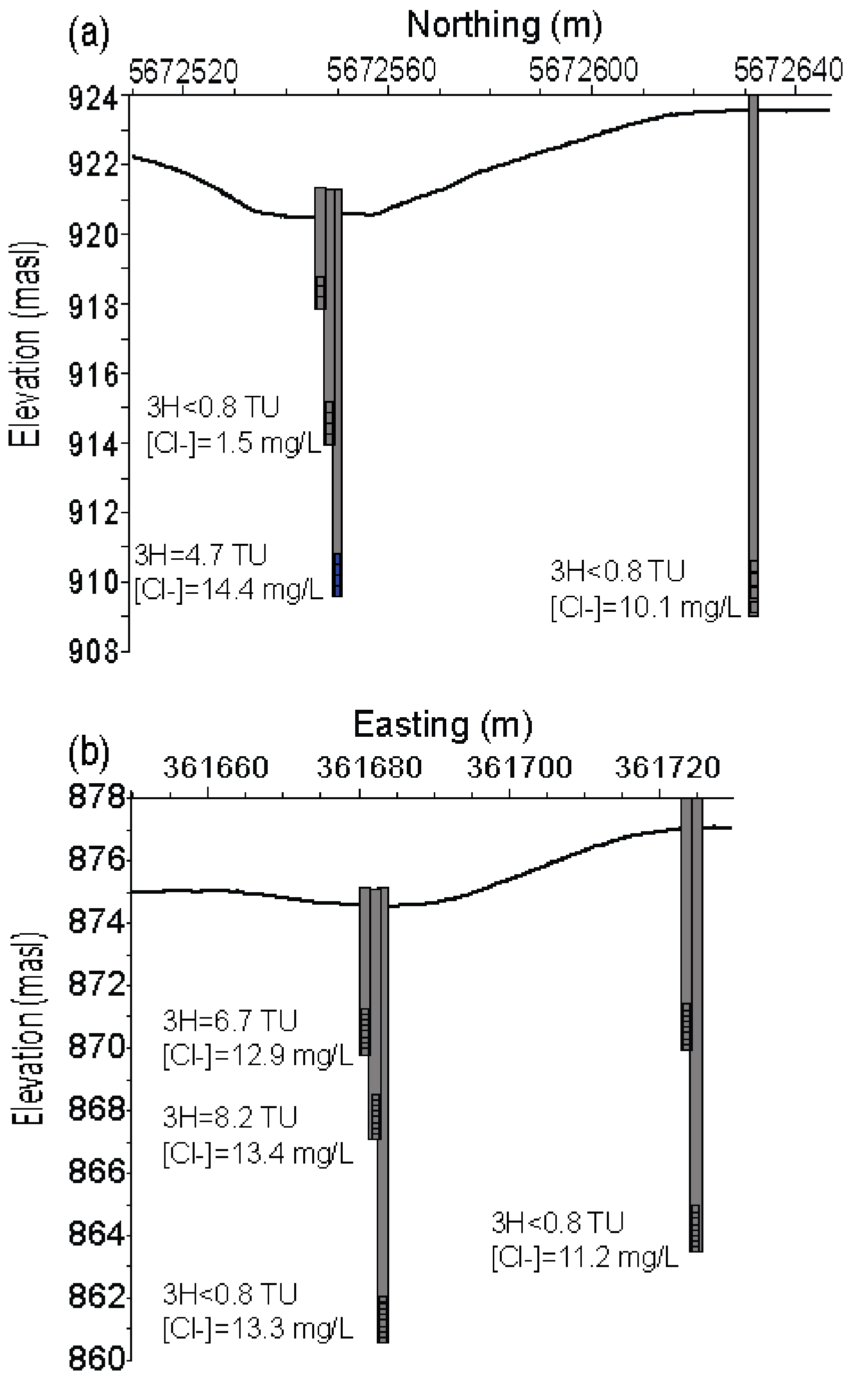

Figure 5.3. Cross-sections of TGG (a) and TGC (b) showing piezometer installation depths. Chloride and tritium concentrations measured are indicated to the left of the respective piezometer.

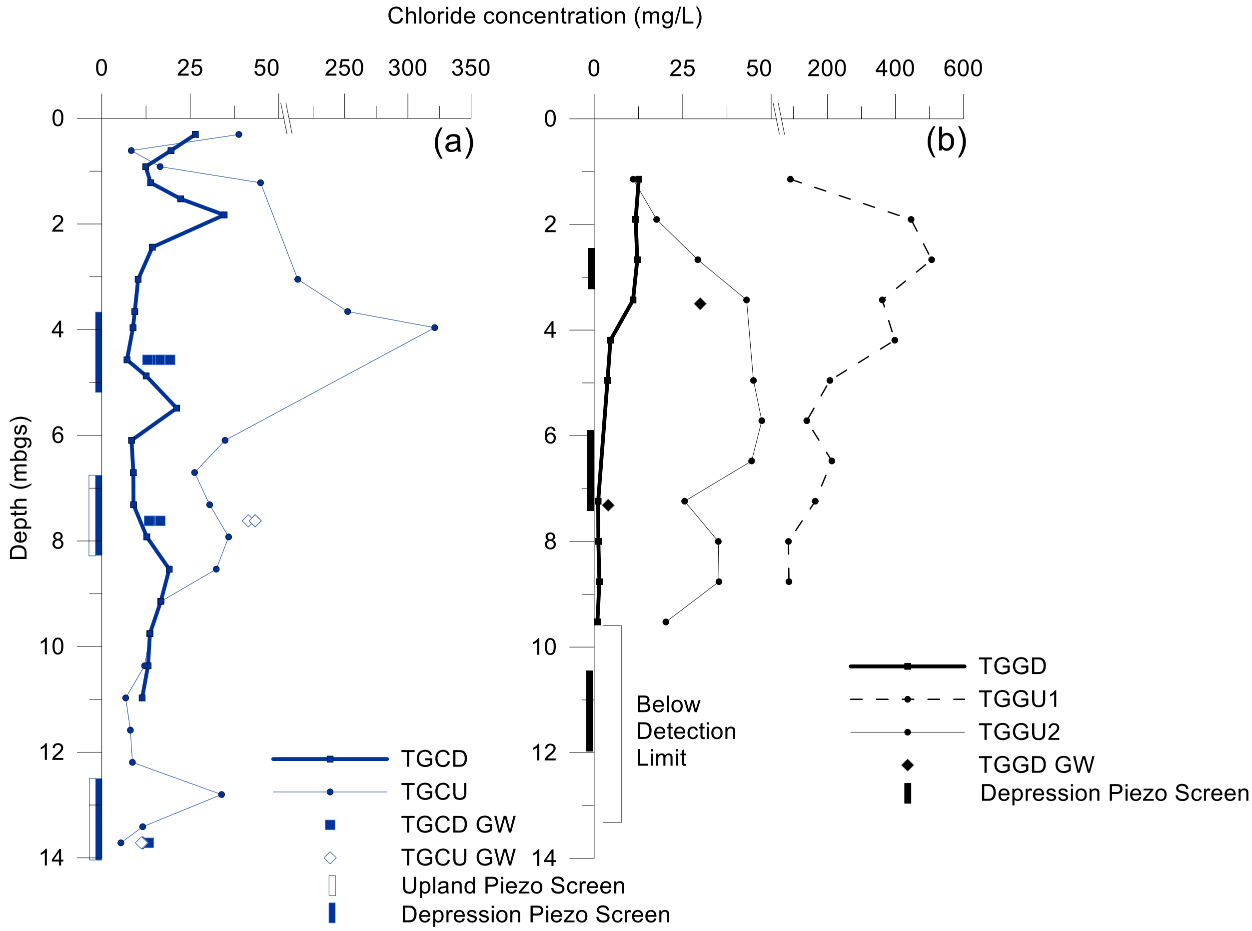

Figure 5.4. Chloride concentration in the cropland (a) and grassland (b). Depression profiles are indicated with a thicker line, groundwater samples are points. TGGU1 is the filled borehole, and TGGU2 is the borehole and piezometer. Chloride concentrations below 9.5 metres at all grassland boreholes were below detection limits. Screened intervals of piezometers are indicated on the y-axis.

Similar to the pore-water chloride concentrations, pore-water sulphate concentrations in the depressions at both locations were less than the uplands, indicating leaching of sulphate salts beneath the depressions (

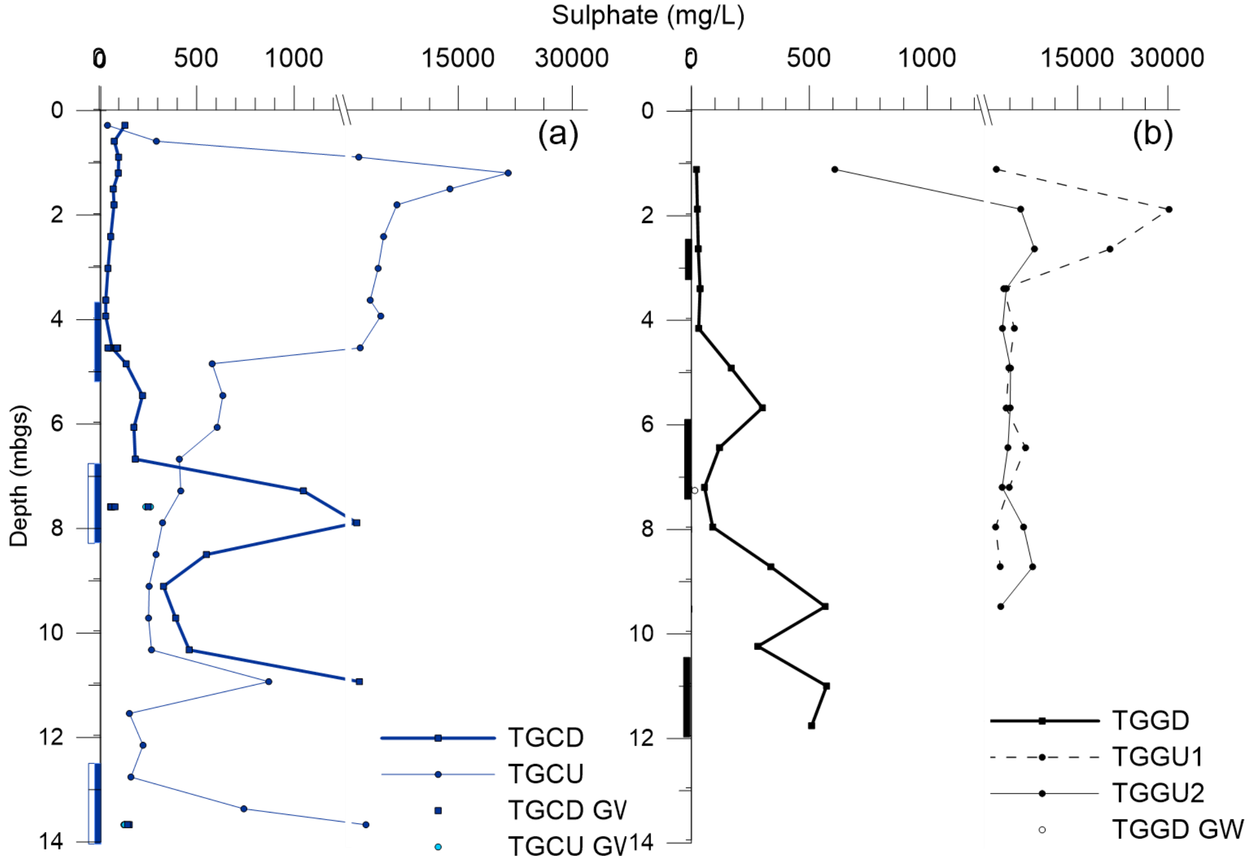

Figure 5.5). Groundwater sample concentrations were very similary to pore-water concentrations over the screened intervals. Very high concentrations of sulphate in the uplands are a result of the dissolution of sulphate salts in the sediments during the pore-water extraction process, as commonly seen in the Canadian prairies (Keller and van der Kamp 1988; Hayashi et al. 2016). While drilling, lenses of white precipitate were found in the core samples over 1.5-2 m depth and speculated to be gypsum. This precipitate layer indicates that there is no recharge in the uplands, as the deposit would be flushed through the soil column leading to lower pore-water concentrations (as in the depression, where this layer was not observed).

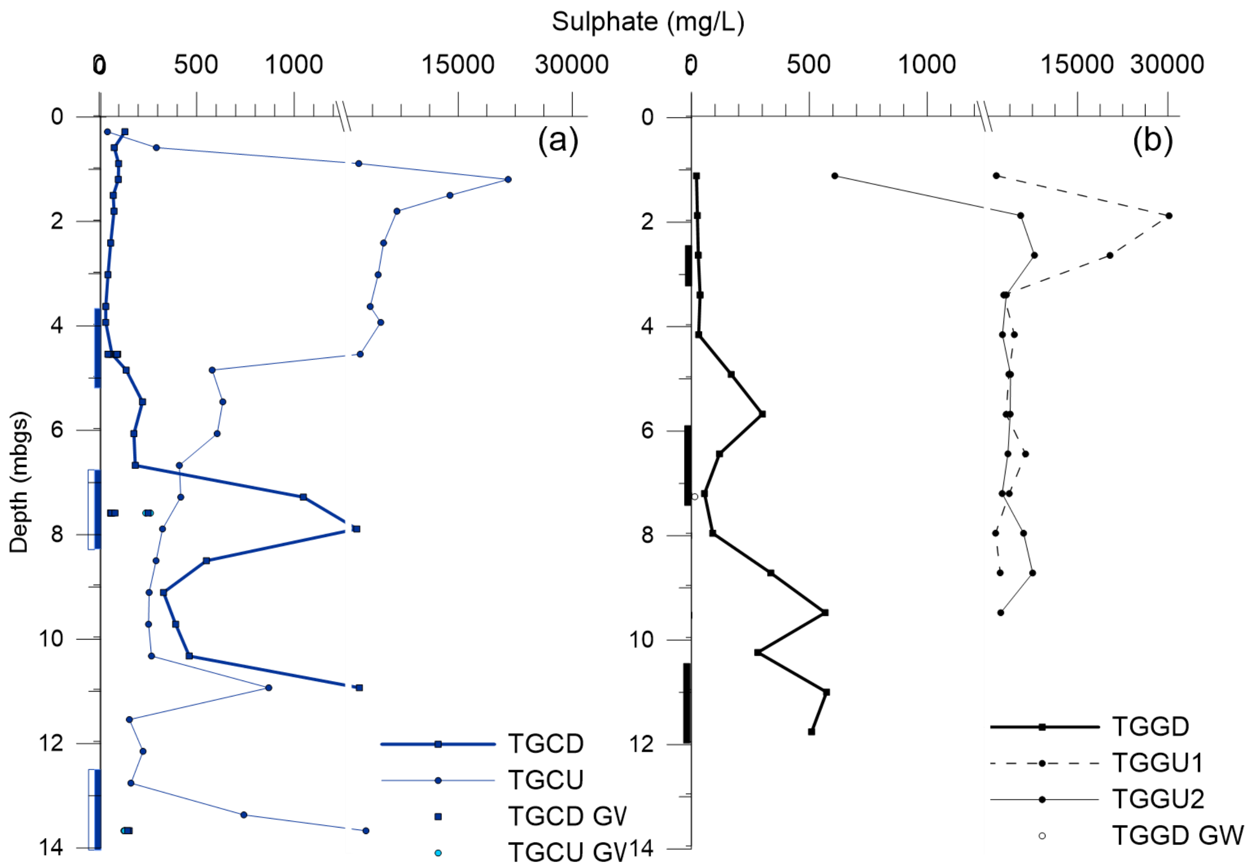

Figure 5.5. Pore-water sulphate concentrations (mg L^{-1}) at TGC (a) and TGG (b) in the uplands and depressions. The break in the axis is from 1200 mg L^{-1} to 1250 mg L^{-1}. TGGU1 is the filled borehole, and TGGU2 is the borehole and piezometer.

Isotope profiles were generally more depleted beneath the depressions than the uplands (Figure 5.6). Groundwater samples were similar isotopically to the surrounding pore-water, excluding samples taken from the sand layer in the cropland at 8 m depth and the water samples from the 8 m depth in the grassland.

To examine these differences, the fraction of winter precipitation that makes up the sample was calculated using the binary mixed isotope fraction method (Eq. 5). C_m for the cropland was -17.45 ‰ and was -19.76 ‰ for the grassland. These values were the arithmetic mean of the $\delta^{18}O$ values at the 8 m piezometers in each location. For the cropland, the average fraction was 29 % winter precipitation. For the grassland, the average fraction was 54 %.

As the different methods were used to analyse samples from pore water and from groundwater have different accuracies (0.25 ‰ for pore-water and 0.1 ‰ for groundwater), comparing the results from the two sample sets can be slightly more difficult. However, the groundwater samples that did not fall close to the pore-water profiles (at 8 m depth in both the grassland and cropland) also did not fit within the expected range of values that would be covered by the accuracy of the two methods.

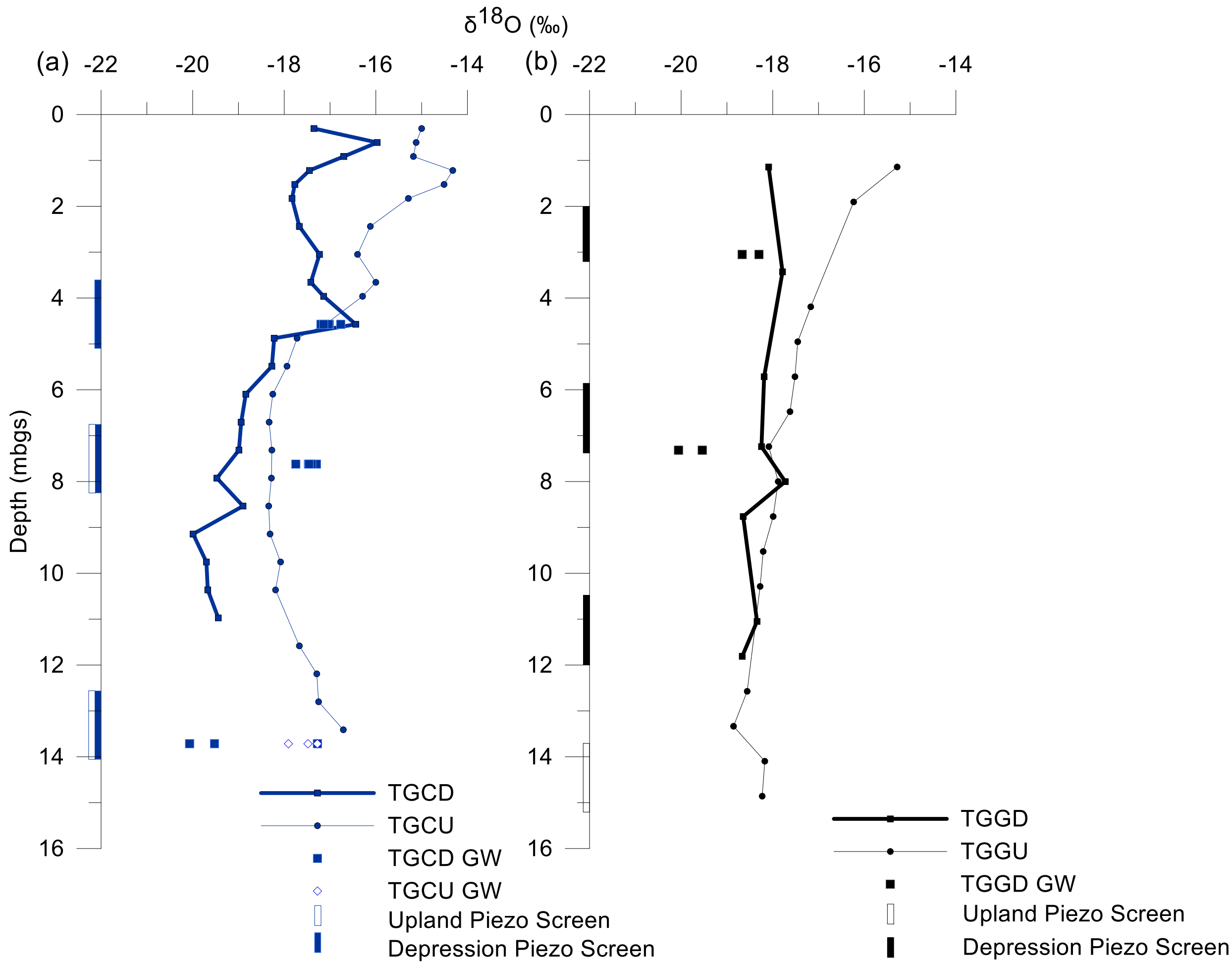

Figure 5.6 Oxygen isotope ratio (‰) for the cropland (a) and grassland (b). Depressions are indicated with a thicker line, and groundwater samples with points. Multiple points at each depth represent distinct sampling events throughout time over multiple seasons. Screened intervals of piezometers are indicated on the y-axis.

Snow, groundwater, pond water, and pore-water samples were plotted alongside the Calgary LMWL (Figure 5.7). Snow samples have much more depleted composition than the winter precipitation average. This is likely a result of differences in weather the two years of the study compared to the 10 years of data for the average, and the distance of the study site from Calgary. Evaporation lines are identifiable in the pond samples for both years. Groundwater and pore-water samples are close to the yearly average isotopic composition. There is a slight offset of the pore-water samples below the LMWL.

The modified lc-excess (d_{lc}) was calculated for each of the pore-water samples from the cropland (Figure 5.8). Grassland pore-water analysis was impacted by evaporation of pore-water in the soil samples between sampling and analysis, with multiple samples having greater than 5% mass lost during storage (data not shown for those samples). The lack of available data for these samples precluded the grassland depression isotopes from being used to calculate the line-conditioned excess in a similar manner to the cropland.

Pore-water in the vadose zone plotted close to $d_{lc} = 0$, while deeper waters plot closer to - 4 ‰. The deeper pore-water samples from the upland plot close to d_{lc} = -8 ‰. The more negative values correspond to a region where tritium was not found. Values of d_{lc} stabilized at - 4 ‰ in the depression at the depth of the static water level (the water level before and after ponded water has fully infiltrated in the spring, *ca.* 3.5 m) (Figure 5.8) and at -8 ‰ in the upland at the depth of the top of the sand unit (approximately 3 m) (Figure 5.1). The upland values in the same layers were more negative than in the depression. The d_{lc} values dropped from near 0 to -7 ‰ at a depth of 1.5 m in the upland, indicating that there was some kinetic fractionation of the water isotopes occurring. This drop did not occur in the depression until the water table was reached, a function of the large amount of snowmelt infiltration that occurs without fractionation, as well as the equilibrium evaporation that occurs in the moist pore spaces. There was a spike in d_{lc} in the cropland upland to 4 ‰ at 10 m depth, which is likely an outlier, as this point was the only one which plotted slightly above the LMWL (Figure 5.7). Groundwater samples plot similarly to the pore-water at similar depths, with the exception of the 8 m depression samples, which are more negative than the pore-water.

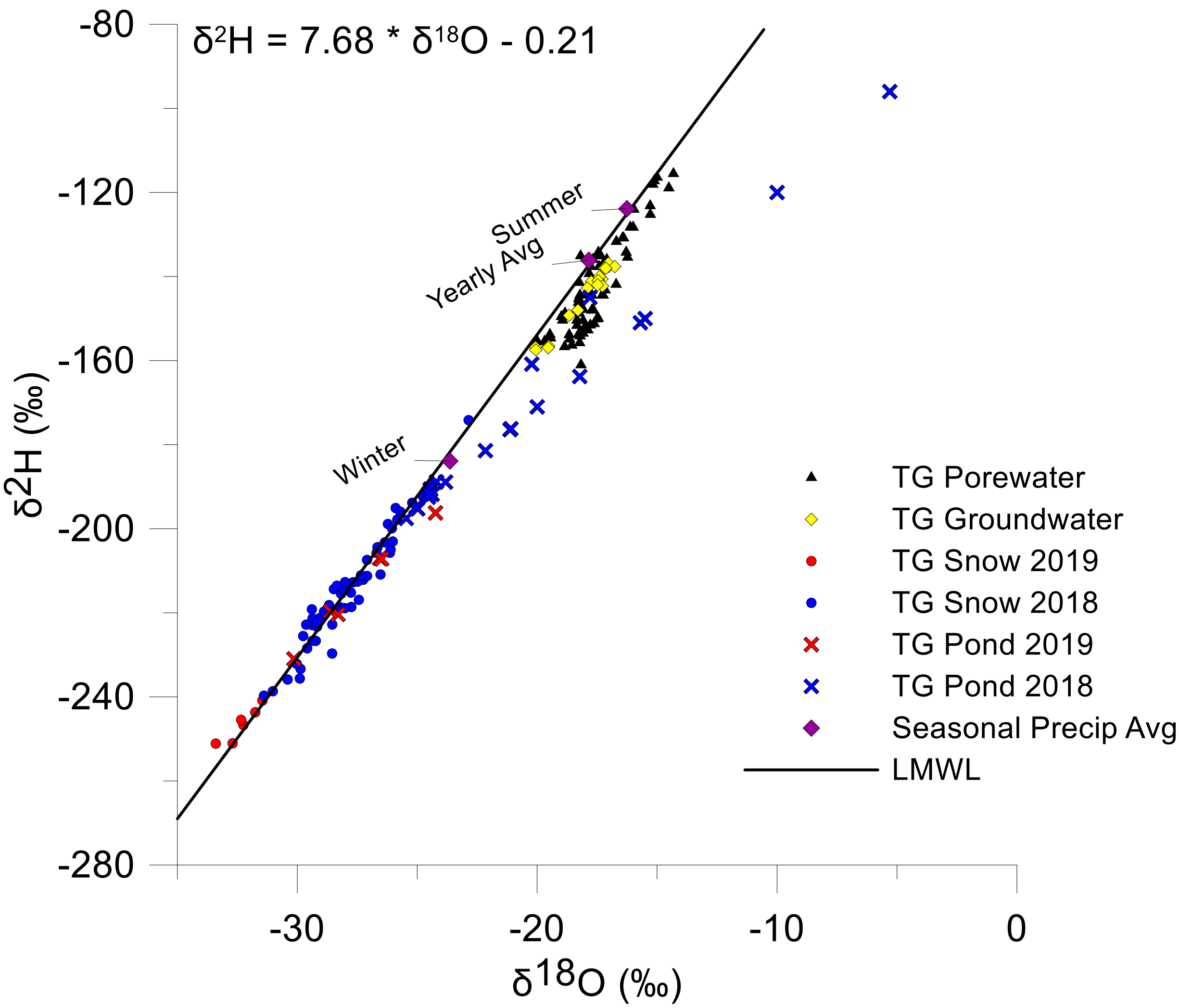

Figure 5.7. Triple G water samples along the LMWL for Calgary, AB. Seasonal and yearly volume-weighted average compositions for Calgary precipitation are shown. Samples plotted are for all sites together (e.g. TG Pond is all pond samples at TGG and TGC for 2018).

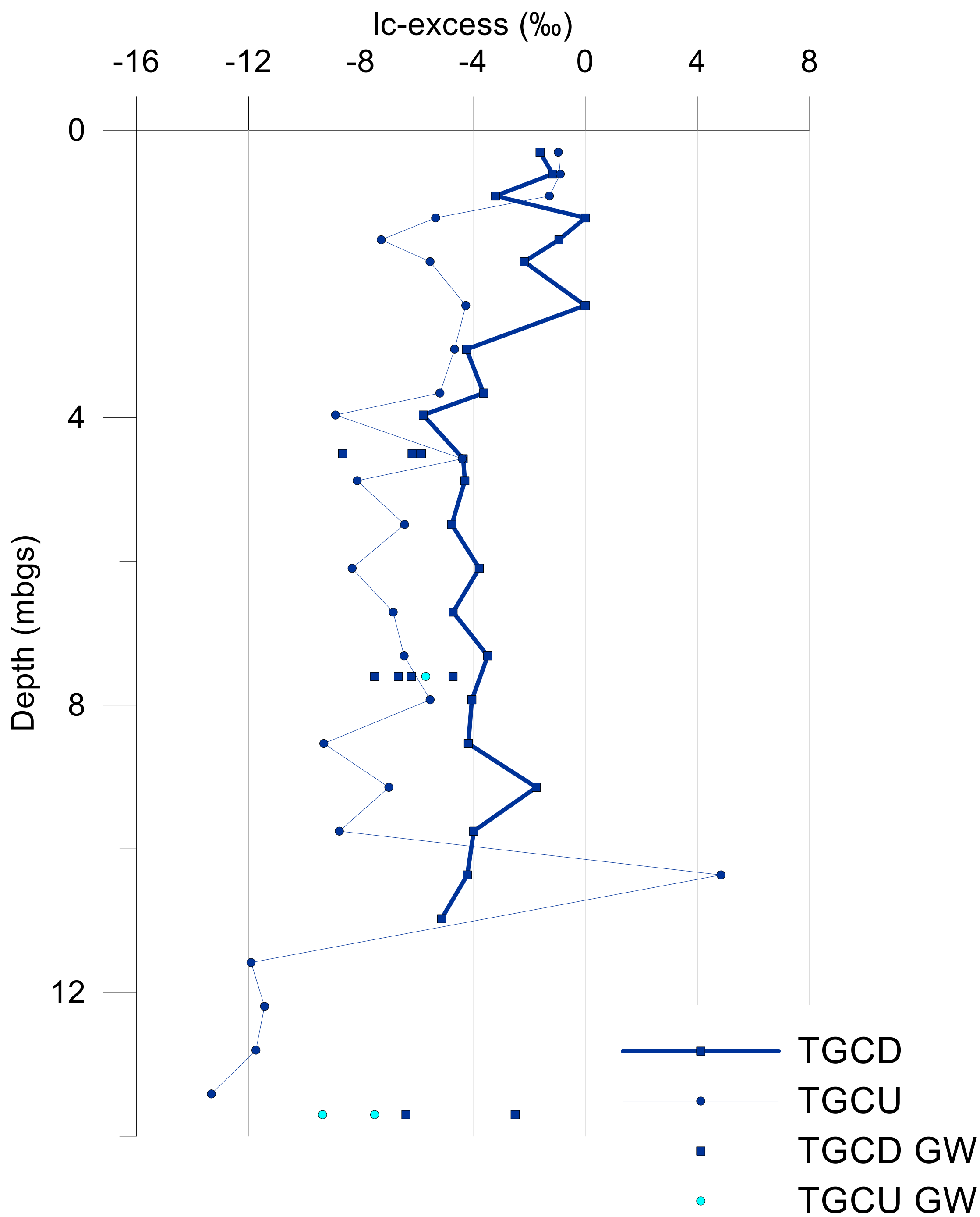

Figure 5.8. Line-conditioned excess (lc-excess) for the cropland boreholes.

5.4.3 Water Table Fluctuation

The water table fluctuation method was applied to both spring pond events in 2018 and 2019, as well as a large rainstorm event that caused ponding in 2018 (Figure 5.9). The grassland had greater recharge than the cropland in both years (Table 5.2).

Groundwater recharge was calculated using the WTF method as follows for TGG in 2019:

$R_{dep} = (\Delta h)\ (S_y)$

$= (2.8\ m)\ (0.11)\ (1000\ mm\ )\ (1\ m^{-1}) = 308\ mm$

$R_{cat} = (R_{dep})\ (A_{dep})\ (A_{cat\backslash})^{-1}$

$= (308\ mm)\ (1160\ m^2)\ (9793\ m^{-2}) = 36\ mm$

Uncertainty was estimated by repeating this calculation with the higher and lower estimates of specific yield.

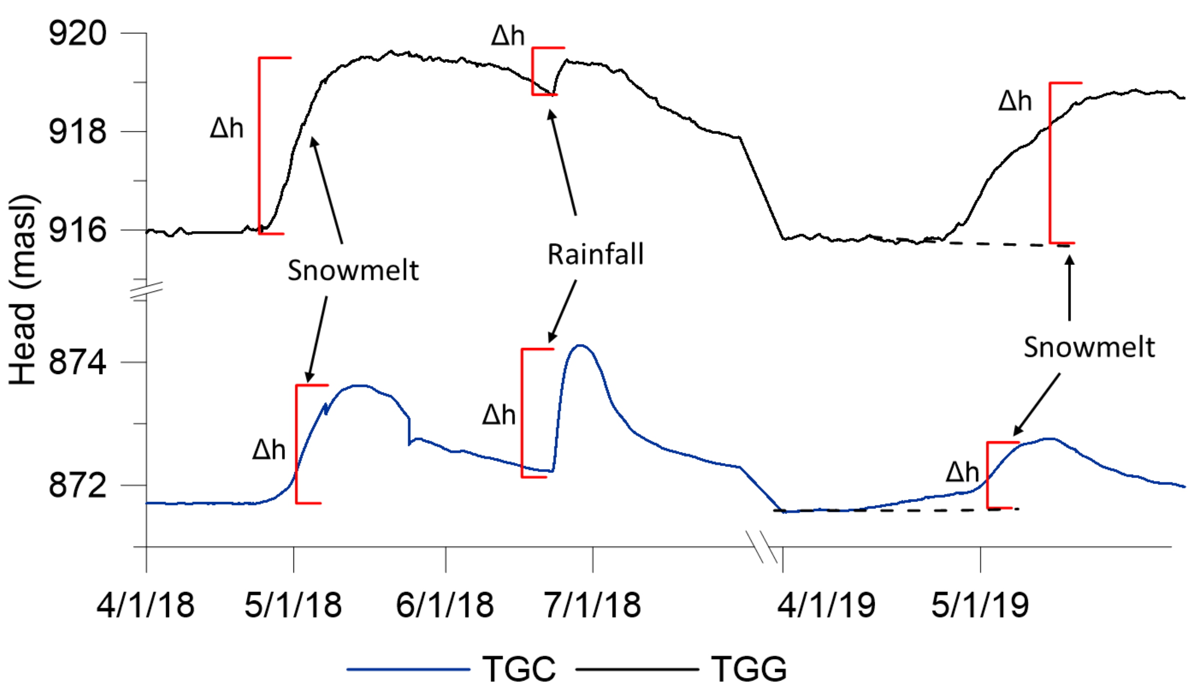

Figure 5.9. Head changes (*Δh*) for each recharge event (red brackets) calculated using the water table fluctuation method. Values of *Δh* for each event are indicated in Table 5.1.

Table 5.2. Water table fluctuation calculation recharge estimates for the 2018 and 2019 spring runoff years. In 2018 there was also a large rainstorm that caused runoff and recharge. R_{dep} is the recharge beneath the depression, R_{cat} is the recharge normalised to the total catchment area. Range of recharge values given account for the error associated with estimating specific yield.

Year	Site	Catchment area (upland / depression) (m^2)	Event Type	Head rise (Δh) (m)	Total R_{dep} (mm)	Total R_{cat} (mm)
2018	TGC	10620 (9602/1018)	snowmelt	1.9	418±190	40±20
			rain	1.9		
	TGG	9793 (8633/1160)	snowmelt	3.7	495±225	58±30
			rain	0.8		
2019	TGC	10620 (9602/1018)	snowmelt	1.1	99±55	12±6
	TGG	9793 (8633/1160)	snowmelt	2.8	308±140	36±19

5.4.4 Chloride Mass Balance

Recharge rates for 2018 and 2019 were also calculated using the CMB method (Equation 2) for the grassland and cropland sites using measured chloride concentrations in groundwater (Table 5.3). The grassland had greater recharge rates than the cropland, likely due to the greater runoff volume in the spring. Despite the differences in lateral chloride flux (Q_{lat}) between the two years, the estimates of recharge within each site are very similar.

Q_{lat} was calculated as follows using TGC in 2018 as an example:

$$Q_{lat} = (C_{pond})\ (V_{pond})\ (A_{upl})^{-1}$$

$$= (3.8\ \text{mg L}^{-1})\ (286\ \text{m}^3)\ (9602\ \text{m}^{-2}) = 113\ \text{mg m}^{-2}\ \text{y}^{-1}$$

Depression-focussed recharge for TGC 2018 was estimated by:

$$R_{dep} = (Q_{lat})\ (A_{upl})\ (A_{dep})^{-1}\ (C_{dep})^{-1}$$

$$= (113\ \text{mg m}^{-2}\ \text{y}^{-1})\ (9602\ \text{m}^{2})\ (1018\ \text{m}^{-2})\ (13\ \text{mg L}^{-1})^{-1} = 82\ \text{mm}$$

This value was normalised to the catchment in the same way as the water table fluctuation.

Uncertainty analysis was completed using Equation 6. For the cropland depression in 2018, the magnitude of recharge was 82 mm, the variance in pore-water chloride concentrations was 3 mg L^{-1}, and the magnitude of pore-water chloride concentration was 13 mg L^{-1}. The magnitude of Q_{lat} was 113 mg m^{2} y^{-1} and with the assumed variance in Q_{lat} of ±8%, the variance of Q_{lat} for 2018 in the cropland depression was 8 mg m^{-2} y^{-1}. These values combined provide the recharge estimate uncertainty of 20 mm.

Chloride concentrations in pore-water that contained tritium in the cropland were averaged over the chloride profile from 4 to 8 metres (the part of the profile below the lowest recorded water table elevation and with known tritium concentrations). This represents “modern” water recharged after 1950-1960. In the grassland, pore-water concentrations from 3 to 4 metres were used, as this part of the profile had previously been identified as modern water, despite the lack of knowledge about tritium concentrations (Pavlovskii et al. 2019b).

The chloride concentration in the sample of fertilizer analysed was 0.11 mg L^{-1}. This means 0.0011 % of the total fertilizer mass is chloride. Fertilizer is applied to the field at a rate of 9.2 g m^{-2} y^{-1} (B. Christensen, personal communication), and thus 0.001 g m^{-2} y^{-1} of chloride is applied in the fertilizer. This chloride load is negligible compared to Q_{lat}.

Chloride concentration in precipitation near TGG and TGC is assumed to range from 0.04 mg L^{-1} to 0.07 mg L^{-1}, and the annual atmospheric chloride deposition over the fields then ranges from 15 to 26 mg m^{-2} (Pavlovskii et al. 2019b). As these values were substantially lower than the calculated lateral flux, precipitation inputs were excluded from the chloride mass balance calculations.

Table 5.3. Recharge estimates for 2018 and 2019 using the chloride mass balance technique and modern pore-water chloride concentrations.

Year	Site	Catchment area (upland / depression) (m^2)	$[Cl^-]$ pore-water (modern water) (mg L^{-1})	$[Cl^-]$ pond (mg L^{-1})	Q_{lat} (mg m^{-2} y^{-1})	R_{dep} (mm y^{-1})	R_{cat} (mm y^{-1})
2018	Cropland	10620 (9602/1018)	13±3	3.8	113±9	82±20	9±2
	Grassland	9793 (8633/1160)	12±3	3	148±12	92±24	12±3
2019	Cropland	10620 (9602/1018)	13±3	3.9	72±6	52±13	6±1
	Grassland	9793 (8633/1160)	12±3	5.6	182±15	112±30	15±4

To estimate groundwater recharge rates before anthropogenic chloride inputs are assumed to have increased (i.e. pre-tritium increases in the 1960's), Equation 3 was used assuming that the only input was PC_p. A range of chloride concentrations in precipitation of 0.04 to 0.07 mg L^{-1} were used for calculations to account for uncertainty in the unmeasured precipitation chloride concentration (Pavlovskii et al. 2019b). This method assumes that the amount of precipitation remains constant through time, and that chloride concentrations in precipitation have not changed. While there would be some lateral transfer occurring, with no anthropogenic inputs to the system, it is assumed that the chloride flux would be in balance between the upland and depression (Hayashi et al. 1998b). Similar chloride concentrations in 14-m piezometers at TGC depression and upland (Figure 5.4a) supports this idea. In contrast, upland and depression concentrations did not converge to similar values at depth under TGG (Figure 5.4b), which precluded the use of Equation 3 at this site. Using the average concentration in 14-m piezometers to represent C_{gw} (13±3 mg L^{-1}) and PC_p = 20.5±5.5 mg m^{-2} y^{-1} in Equation 3, pre-settlement R_{cat} at TGC was estimated to be 15 ± 5 mm y^{-1}.

5.5 Discussion

Although at first appearing contradictory, the subsurface electrical conductivity distribution indicates depression-focussed recharge occurring beneath the depression at both sites. As conductivity is a function of salinity and moisture, all must be considered in interpreting results. Within the grassland, the depressions are the wettest part of the field, leading to higher conductivity simply due to the increased water content. In the cropland, however, where the field is consistently wetter, the leaching of salts beneath the depression leads to lower conductivity relative to the surrounding areas.

The depression chloride (Figure 5.4) and sulphate (

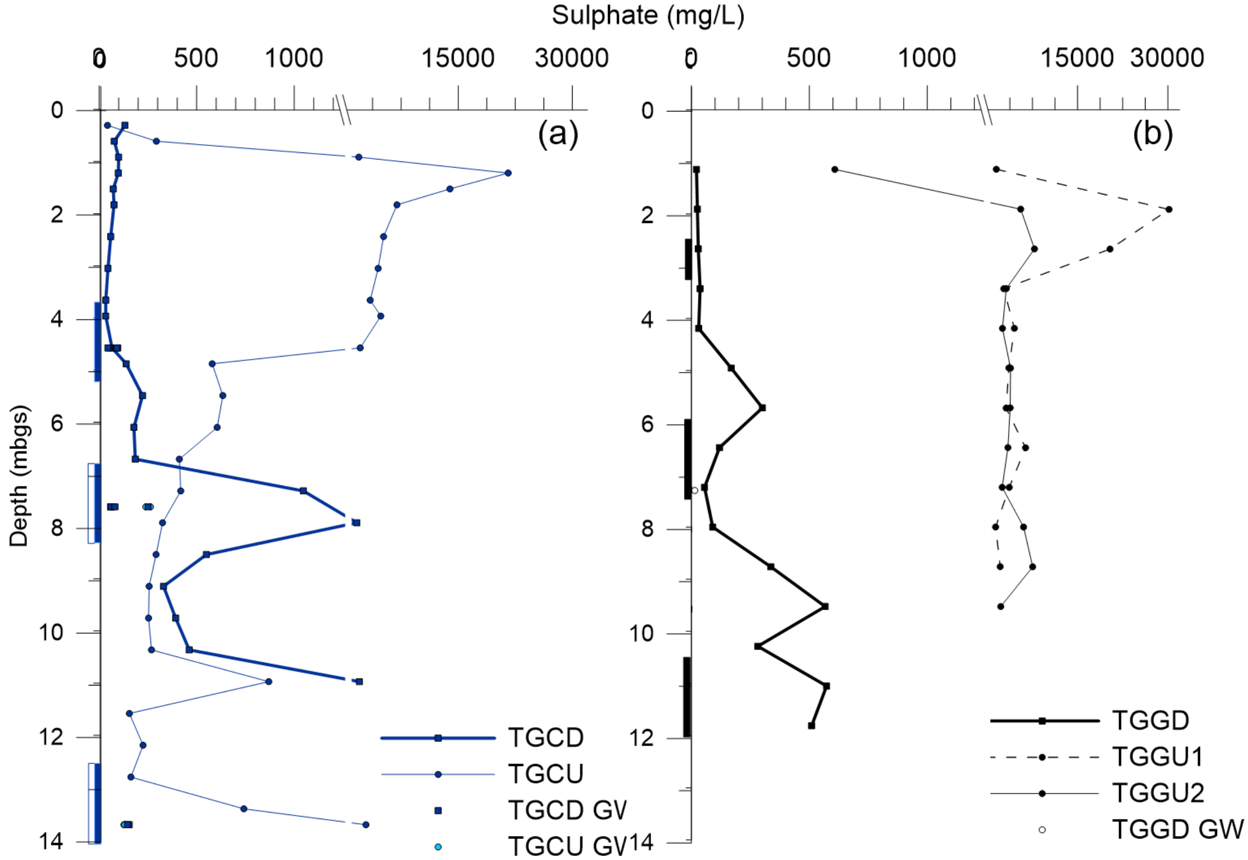

Figure 5.5) profiles at each site indicate that leaching is occurring in the depressions relative to the uplands. The high chloride and sulphate concentration at 3 to 4 metres depth in both uplands is indicative of salt accumulation and implies that there has been little to no recharge beneath the upland areas (Hayashi et al. 1998b; Pavlovskii et al. 2019b). The pore-water isotope compositions in the depressions at each site are more negative than the respective uplands, further indicating depression-focussed recharge of snowmelt water (Pavlovskii et al. 2018). The combination of these two supports the electrical conductivity data, and it is unlikely that there is diffuse recharge occurring beneath the uplands in these two fields.

Based on the isotope profiles (Figure 5.6), most groundwater samples were isotopically similar to the pore-water. The depression pore-water was more negative than the upland pore-

water, however, there was some variation in the mid-level piezometers at both sites.
The TGC 8 m piezometers are located within the sand layer, which had a higher hydraulic conductivity (on the order of 10^{-6} m s^{-1}) than the surrounding clays (Figure 5.1). The groundwater samples from these piezometers in sand were similar to those from the 4 m depression piezometer and were also more similar to the upland 8 m pore-water composition. This similar composition may be due to the connectivity of the sand layer throughout the site allowing for mixing, and an averaging of isotopic composition. This mixing is assumed to occur due to the concurrent changes in head in the upland sand layer piezometers during ponding (Appendix D). The lc-excess of the depression groundwater samples at these depths also did not match the pore-water profile, and were closer to the upland profile.

The grassland 8 m piezometer groundwater sample showed a more depleted isotopic composition than the pore water, possibly indicating a greater proportion of snowmelt than rainwater influence. As previously mentioned, there was no overlap of these samples taking the measurement error for the analyses into account. However, during pore-water spiking tests conducted on soil samples from TGG, it was noted that there was a large range of error possible, and the water samples would fall within this range (Pavlovskii, 2019).

The depression isotope profiles, while more negative than the uplands, were isotopically heavier (i.e. more positive) than the snowmelt runoff water. This is because the evaporation of open ponded water leads to the loss of lighter isotopes, and the resulting pond water is heavier than pure snowmelt (Pavlovskii et al. 2018). However, the depression pore-water is still less evaporatively enriched (d_{lc} closer to zero) than the upland due to the infiltration of the ponded water over time. Pore-water that has been evaporatively enriched in the near-surface in the upland is only occasionally pushed deeper during large rainfall and snowmelt events, leading to more enrichment occurring between events, and a more negative d_{lc}.

Recharge estimates for the grassland using the chloride mass balance method were compared to a previous study in the same depression and were slightly lower than the estimated 202 mm y^{-1} calculated beneath the depression and 26 mm y^{-1} beneath the entire catchment (Pavlovskii et al. 2019b). These differences are likely due to the way that the lateral flux of chloride was calculated, as the previous study utilized buried runoff plots to collect water that moved through the subsurface and collected chloride, as well as ponded water, while this study used only ponded water sitting over the depression. Differences between the runoff plot and pond water chloride concentrations could be due to subsurface chloride transport or different placement of salt blocks within the field that year.

Chloride inputs are likely highly variable year to year in both fields. The inputs in the grassland depend on grazing patterns and the placement of salt blocks within the field, while the cropland depends on grazing (the field is used for steer and horses over winter) and the type and application rate of fertilizer. The application of the CMB method assumes that the lateral flux of chloride has been relatively constant through time, however recharge estimates for both fields using different Q_{lat} values for 2018 and 2019 had results in similar groundwater recharge rates. Using a multi-year average of Q_{lat} would account for the range of recharge values that were observed and could be expected.

The estimates of recharge obtained from using the catchment-scale method were consistent with what has typically been observed in the Canadian prairies of 2-20 mm y^{-1} (Hayashi and Farrow, 2014; Pavlovskii et al. 2019b). This application of the CMB method assumes that there is no Q_{in} or Q_{lat}. This is likely the case for Q_{in}, given that there would be no anthropogenic inputs. The lateral flux of chloride between the uplands and depressions would likely be balanced over the year (Hayashi et al. 1998b).

The water table fluctuation method provided a much greater estimate of groundwater recharge than the chloride mass balance technique, even considering the error associated with the specific yield estimation. This method also showed that there was greater recharge beneath the grassland than the cropland in 2019. The difference in magnitude of estimations between the two methods is likely because while the water does reach the water table, some of the shallow groundwater is consumed via evapotranspiration over the summer (see Chapter 3 for ET and soil moisture change).

The WTF method, as applied here, does not account for any time-variable specific yield changes or the Lisse effect, whereby entrapped air in the subsurface sediments causes a greater rise in water table than would occur from only water flow (Crosbie et al. 2005). This effect is less likely to occur if sediments are fully saturated before the rainfall. As seen in Chapter 3, the grassland depression sediments were fully saturated, however the cropland was not fully saturated at the 20 cm sensor, and as such there is likely some influence of the Lisse effect in the cropland water level rise.

The water table fluctuation methods showed that there was more groundwater recharge occurring beneath the grassland than the cropland, an unexpected result given previous studies (van der Kamp et al. 2003; van Dijk 2005; Hayashi and Farrow 2014). However, this increased recharge value is not necessarily supported by the CMB method, where the quantity of recharge is similar between the two sites. As the CMB method averages groundwater recharge over multiple years and accounts for evapotranspiration differences, there is likely little difference between the two sites.

Generally, the reduced number, size, and depth of macropores in croplands would increase the amount of snowmelt runoff in a cropland, leading to greater groundwater recharge. While the cropland site did have a greater proportion of snowmelt runoff relative to snow water equivalent (Chapter 3), the overall amount of snow, and thus runoff, was less. This finding emphasizes the importance that topography and aspect can play in snow accumulation. The grassland site has steeper slopes surrounding the depression which, when combined with the slope aspect relative to the general wind direction, facilitates the formation of large snowdrifts around the depressions (Chapter 3). This snow drains directly into the depressions as it melts, increasing the snowmelt runoff and thus groundwater recharge.

5.6 Conclusions

Isotopic profiles can be useful to determine the source of groundwater (whether from winter or summer precipitation), as well as dating groundwater in the case of tritium. Post-settlement chloride inputs alongside the pore-water chloride concentration of tritium-laden water, can be used to estimate aggregated groundwater recharge rates beneath different land uses. For short-term estimations of groundwater recharge, the water table fluctuation method can be used, but with caution in the prairie environment, as much of this shallow groundwater can be utilized by plants throughout the growing season and lost to evapotranspiration. Despite the larger runoff ratios observed in the cropland (see Chapter 3), the grassland depression appeared to have a greater groundwater recharge rate than the cropland when recharge was calculated using the WTF method due to the greater amount of water that ponds. When comparing recharge quantities with the CMB method, however, which accounts for growing season ET, the recharge quantities were similar between the two fields. This study highlights the complexity in comparing groundwater recharge quantities using a single paired-plot study site, as well as the need for careful selection of sites with similar topography.

Chapter 6. Conclusions

6.1 Synthesis and Summary

Effective groundwater management frameworks require knowledge of all components of the system, including groundwater recharge. However, in the semi-arid Canadian prairies, groundwater recharge rates are low and difficult to measure directly using a water balance approach. The magnitude of error associated with directly measuring evapotranspiration is often greater than the total amount of groundwater recharge. This study aimed to better understand groundwater recharge rates in the prairies, through measuring snowmelt runoff and estimating groundwater recharge rates beneath different land uses.

Snowmelt runoff processes are governed by many factors that land use can influence, such as antecedent moisture conditions and snow water equivalent, but also by the landscape in general in the form of topographic relief and slope aspect. The landscape affects the land use, where lower relief fields are the first to be converted from grasslands to croplands, as it is easier to farm.

In this study, snowmelt runoff was measured directly by measuring the height of snowmelt runoff water ponded in a depression, and remotely using aerial or satellite imagery to estimate the total ponded area. These heights or areas were then converted to volumes of water using relationships from a digital elevation model. In the West Nose Creek watershed, croplands generally generated more snowmelt runoff than grasslands regardless of topography. However, the paired plot site at Triple G showed that the importance of topography and aspect cannot be overlooked at a small scale, as a higher-relief grassland field generated more snowmelt runoff than a nearby lower-relief cropland field.

High-resolution satellite imagery can be used in conjunction with a high-resolution DEM to estimate the total ponded area of spring snowmelt. While this method allows for a comparison of relative snowmelt runoff volumes, it cannot estimate the relative amount of snowmelt compared to SWE (i.e. runoff ratio) and cannot account for the infiltration of ponded water into frozen soil. However, future work coupling remote sensing observations with snow accumulation and infiltration models could allow for more constrained estimates of snowmelt runoff.

Groundwater recharge rates in the prairies are low, often a fraction of the volume of ponded water each year. This is due to evapotranspiration throughout the growing season, as well as lateral flux of water away from the depressions. There are a variety of ways to estimate groundwater recharge, and this study compared the water table fluctuation and chloride mass balance methods.

The water table fluctuation method showed greater groundwater recharge rates beneath the grassland than the cropland. This was unexpected based on land use alone, as the cropland was expected to have higher runoff ratio, and thus groundwater recharge. However, this higher rate of groundwater recharge was determined to be reasonable when the pre-melt snow water equivalent and volume of snowmelt runoff between the two fields was compared. Despite the greater snowmelt runoff ratio in the cropland field, the grassland had a greater SWE and total volume of runoff overall due to the site's orientation and topography. This finding highlights the importance of topography in snowmelt runoff generation and overall groundwater recharge amounts.

Grasslands and croplands can have different growing seasons in the prairies, where grasslands will begin to grow once there is adequate sunlight and soils have thawed, while croplands are often not seeded until the risk of frost and snow is gone. Crops are harvested in the late summer (typically at the end of August or early September), while grasses can still grow for another month, depending on the weather that year. The longer growing season, along with deeper roots in the perennial grasslands allowing for more access to soil water, causes the evapotranspiration in grassland sites to be greater than that in the croplands.

The water table fluctuation method, while a useful first-cut approximation for the seasonal amount of groundwater recharge, is limited by both its assumptions of vertical groundwater flow and a lack of ability to account for shallow groundwater consumption over the growing season. The chloride mass balance estimates of groundwater recharge showed that actual groundwater recharge rates averaged over the last 10 to 30 years are two to four times less than those calculated using the water table fluctuation method. This method also showed slightly greater recharge beneath the grassland than the cropland, but the values are not significantly different given the uncertainty bounds. The CMB estimates average recharge over multiple years, and as such account for evapotranspiration, which the WTF method does not. The large difference in groundwater recharge rates between the grassland and cropland seen using the WTF method is reduced by the much greater evapotranspiration in the grassland over the growing season.

While the two winter seasons used for most of the analyses were in years with plentiful snowfall and one or no midwinter melts, the weather in the area is highly variable year to year. Many years have multiple midwinter melt events that can completely deplete the snowpack and cause ponding and infiltration before the soil has thawed. Some years have very little snowfall, leading to low volumes of snowmelt runoff. The processes controlling snowmelt runoff generation between land uses can be observed on this short time scale, but average groundwater recharge cannot. To overcome this high degree of variability, long-term studies or methods to estimate groundwater recharge on a longer time scale are necessary.

6.2 Limitations and Future Research

The largest limitation in this study was the number of sites compared for groundwater recharge. Further land use comparison sites, particularly if they had more similar topography than Triple G, would be beneficial to estimate groundwater recharge using the chloride mass balance technique. Extra sites would also be beneficial in examining the viability of lc-excess for dating water in the prairies. Modelling could be better constrained with more sites available for calibration. The measurement of evapotranspiration is always a limitation in the semi-arid regions, due to the error associated with all estimates, even those using an eddy-covariance system. For this reason, a water balance to estimate recharge was not calculated.

A major limitation with the remote sensing is selector bias, where the only depressions analyzed were depressions that had snowmelt runoff. To help allay this bias in the future, all possible depressions that fit the criteria (i.e. all catchments are resolvable on the scale of the DEM) should be considered and compared. The development of an object-based supervised classification scheme for remote sensing data could allow for the larger-scale application of the remote sensing analysis described in Chapter 4, and reduce or remove the selector bias. The coverage of estimations could be expanded as the availability of high-resolution DEMs expands throughout southern Alberta. This method could also be coupled with a physically-based snow model, such as the Prairie Blowing Snow Model (Fang and Pomeroy 2009), to estimate the SWE across the landscape and the runoff ratio in the fields. Runoff ratios allow for a normalised comparison of runoff relative to snow amounts, and thus are easier to compare directly across fields.

Further use of line-conditioned excess in soil profiles along with tritium concentrations in pore water could confirm the speculation that the tritium-free water in TGC was isotopically distinct due to deposition under a different climate. The distinction in lc-excess could reduce the need for tritium dating.

6.3 Research Implications

Groundwater recharge rates could be increased by converting higher relief grassland fields to croplands, and, if maintaining grazing pasture area is required, converting the lower relief cropland fields to grasslands. The cropland fields would generate greater volumes of snowmelt runoff, and with their shallower root systems and lower evapotranspiration over the growing season, use less of the water that infiltrates over the growing season (leading to greater yearly recharge). To ensure as much snow as possible is captured, fields should have tall stubble left on them. Given the impact of man-made structures such as fences observed in this study, they can also be a viable way to trap snow in specific locations to increase snowmelt runoff.

Expanding the coverage of high-resolution DEMs will allow for larger areas to have snowmelt runoff estimates generated remotely via satellite imagery. These estimates of snowmelt runoff could be used to calibrate models over a larger area and multiple land uses and allowing for better constraints on groundwater recharge rates.

References

Alberta Environment and Parks (2017a) Bow, Oldman and South Saskatchewan River Basin water allocation order. Water Act Alberta Regulation 171/2007. Web access: http://www.qp.alberta.ca/1266.cfm?page=2007_171.cfmandleg_type=Regsandisbncln=9780779725748 last accessed Sept. 21 2019.

Alberta Environment and Parks (2017b) Water Act. Web access: http://www.qp.alberta.ca/documents/Acts/w03.pdf last accessed Sept. 21 2019.

Allison GB, Hughes MW (1983) The use of natural tracers as indicators of soil-water movement in a temperate semi-arid region. Journal of Hydrology 60:157–173. doi: 10.1016/0022-1694(83)90019-7

Allison GB, Cook P., Barnet SR, et al (1990) Land clearance and river salinisation in the western Murray Basin, Australia. Journal of Hydrology119:1–20. doi: 10.1016/0022-1694(90)90030-2

Allison GB, Gee GW, Tyler SW (1994) Vadose-zone techniques for estimating groundwater recharge in arid and semiarid regions. Soil Science Society of America Journal 58:6–14. doi: 10.2136/sssaj1994.03615995005800010002x

Barr AG, van der Kamp G, Black TA, et al. (2012) Energy balance closure at the BERMS flux towers in relation to the water balance of the White Gull Creek watershed 1999-2009. Agricultural and Forest Meterology 153: 3-13 doi: 10.1016/j.agrformet.2011.05.017

Berthold S, Bentley LR, Hayashi M (2004) Integrated hydrogeological and geophysical study of depression-focused groundwater recharge in the Canadian prairies. Water Resources Research 40:14. doi: 10.1029/2003WR002982

Brus DJ, Knotters M, van Dooremolen WA, et al (1992) The use of electromagnetic measurements of apparent soil electrical conductivity to predict the boulder clay depth. Geoderma 55:79–93. doi: 10.1016/0016-7061(92)90006-S

Canadell, J, Jackson RB, Ehleringer JR, et al (1996) Maximum rooting depth of vegetation types at the global scale. Oecologia 108:583–595. doi: 10.1007/BF00329030

Charuchittipan D, Babel W, Mauder M, et al (2014) Extension of the averaging time in eddy-covariance measurements and its effect on the energy balance closure. Boundary-Layer Meterology 152: 303-327 doi: 10.1007/s10546-014-9922-6

Cheng DH, Wang YH, Duan JB, et al (2015) A new analytical expression for ultimate specific yield and shallow groundwater drainage. Hydrological Processes 29:1905–1911. doi: 10.1002/hyp.10306

Crosbie RS, Binning P, Kalma JD (2005) A time series approach to inferring groundwater recharge using the water table fluctuation method. Water Resources Research41:1–9. doi: 10.1029/2004WR003077

Doolittle JA, Brevik EC (2014) The use of electromagnetic induction techniques in soils studies. Geoderma 223–225:33–45. doi: 10.1016/j.geoderma.2014.01.027

EBA Engineering Consultants, 2003. Spy Hill Lands Provincial Aggregate Operation Hydrogeological Assessment. Calgary, Alberta.

Fang X, Pomeroy JW (2009) Modelling blowing snow redistribution to prairie wetlands. Hydrological Processes 23: 2557-2569 doi: 10.1002/hyp.7348

Farrow CR (2014) Winter Surficial Processes and Groundwater Recharge in the Southern Alberta Prairies. MSc Thesis, University of Calgary

Fiedler FR, Frasier GW, Ramirez JA, Ahuja LR (2002) Hydrologic response of grasslands: effects of grazing, interactive infiltration, and scale. Journal of Hydrologic Engineering 7:4 293-301 doi: 10.1061/(asce)1084-0699(2002)7:4(293)

Frazier PS, Page KJ (2000) Water body detection and delineation with Landsat TM data. Photogrammetric Engineering and Remote Sensing 66: 1461–1467

Foken T (2008) The energy balance closure problem: An overview. Ecologial Applications 18:6 1351-1367 doi: 10.1890/06-0922.1

Gao B (1996) NDWI—A normalized difference water index for. Remote Sensing of Environment 266: 257–266. doi: 10.1016/S0034-4257(96)00067-3

Geonics EM31-MK2. http://www.geonics.com/html/em31-mk2.html. Accessed 20 Jun 2017

Government of Alberta (2005) Natural Regions and Subregions of Alberta (shapefile) [WWW Document]. URL http://www.albertaparks.ca/media/429607/natural_regions_subregions_of_alberta.zip

Granger R, Gray D, Dyck G (1984) Snowmelt infiltration to frozen prairie soils. Canadian Journal of Earth Sciences 21:6 669-677 doi: 10.1139/e84-073

Guha S (2007) Quantification of depression storage and its relation with land and soil parameters. MGIS Thesis, University of Calgary

Hayashi M, van der Kamp G, Rudolph DL (1998a) Water and solute transfer between a prairie wetland and adjacent uplands, 1. Water balance. Journal of Hydrology 207:42-55 doi: 10.1016/S0022-1694(98)00098-5

Hayashi M, van der Kamp G, Rudolph D (1998b) Water and solute transport between a prairie wetland and adjacent uplands, 2. Chloride cycle. Journal of Hydrology 207: 56-67 doi: 1016/S0022-1694(98)00098-5

Hayashi M, van der Kamp G (2000) Simple equations to represent the volume-area-depth relations of shallow wetlands in small topographic depressions. Journal of Hydrology 237: 74-85 doi: 10.1016/S0022-1694(00)00300-0

Hayashi M, van der Kamp G. Schmidt R (2003) Focused infiltration of snowmelt water in partially frozen soil under small depressions. Journal of Hydrology 270: 214-229 doi: 10.1016/S0022-1694(02)00287-1

Hayashi M, Jackson JF, Xu L (2010) Application of the Versatile Soil Moisture Budget Model to estimate evaporation from prairie grassland. Canadian Water Resources Journal 35:2 187-208

Hayashi M, Mohammed GA, Farrow CR, et al (2011) Little pond on the prairie: Effects of land-surface hydrology on groundwater recharge. Geohydro 1-6

Hayashi M, Farrow CR (2014) Watershed-scale response of groundwater recharge to inter-annual and inter-decadal variability in precipitation (Alberta, Canada). Hydrogeology Journal, 22(8), 1825–1839, doi: 10.1007/s10040-014-1176-3

Hayashi M, van der Kamp G, Rosenberry DO (2016) Hydrology of prairie wetlands: Understanding the integrated surface-water and groundwater processes. Wetlands 36:237–254. doi: 10.1007/s13157-016-0797-9

Healy RW, Cook PG (2002) Using groundwater levels to estimate recharge. Hydrogeology Journal 10:91–109. doi: 10.1007/s10040-001-0178-0

Hendry MJ, Kelln CJ, Wassenaar LI, Shaw J (2004) Characterizing the hydrogeology of a complex clay-rich aquitard system using detailed vertical profiles of the stable isotopes of water. Journal of Hydrology 293:47–56. doi: 10.1016/j.jhydrol.2004.01.010

Hubbard D, Linder R (1986) Spring runoff retention in prairie pothole wetlands. Journal of Soil and Water 41:2 122-125

Ireson AM, van der Kamp G, Ferguson G, et al (2013) Hydrogeological processes in seasonally frozen northern latitudes: understanding, gaps and challenges. Hydrogeology Journal 21:1 53-66 doi: 10.1007/s10040-012-0916-5

Johnson WC, Millett BV, Gilmanov T, et al (2005) Vulnerability of northern prairie wetlands to climate change. BioScience 55:10 863-872 doi: 10.1641/0006-3568(2005)055[0863:vonpwt]2.0.co;2

Kallner A (2014) Laboratory statistics: handbook of formulas and terms. Elsevier

Keller CK, van der Kamp G, Cherry JA (1988) Hydrogeology of two Saskatchewan tills, I. Fractures, bulk permeability, and spatial variability of downward flow. Journal of Hydrology 101:97-121 doi: 10.1016/0022-1694(88)90030-3

Kochendorfer J, Nitu R, Wolff M, et al (2017) Analysis of single-Alter shielded and unshielded measurements of mixed and solid precipitation from WMO-SPICE. Hydrology and Earth System Sciences 21:7 3525-3542 doi: 10.5194/hess-21-3525-2017

Koehler G, Wassenaar LI, Hendry MJ (2000) An Automated Technique for Measuring δD and δ^{18}O Values of Porewater by Direct CO_2 and H_2 Equilibration. Analytical Chemistry 72:5659–5664. doi: 10.1021/ac000498n

Kyte E (2018) Evaluation of nitrate in groundwater under long-term manure application. MSc thesis, University of Calgary

Landwehr JM, Coplen TB (2004) Line-Conditioned Excess: A New Method for Characterizing Stable Hydrogen and Oxygen Isotope Ratios in Hydrologic Systems. In: International Conference on Isotopes in Environmental Studies – Aquatic Forum 2004. pp 132–135

Lapen DR, Martz LW (1996) An investigation of the spatial association between snow depth and topography in a Prairie agricultural landscape using digital terrain analysis. Journal of Hydrogeology 184: 277–298. doi: 10.1016/0022-1694(95)02975-3

LeBlanc F (2017) Laboratory investigation of infiltration processes in frozen soil and the influence of antecedent moisture content and macroporosity. MSc thesis. University of Calgary.

Maule CP, Chanasyk DS, Muehlenbachs K (1994) Isotopic determination of snow-water contribution to soil water and groundwater. Journal of Hydrology 155:73–91. doi: 10.1016/0022-1694(94)90159-7

McFeeters SK (1996) The use of the Normalized Difference Water Index (NDWI) in the delineation of open water features. International Journal of Remote Sensing 17:1425–1432. doi: 10.1080/01431169608948714

Mekis E, Vincent LA (2011) An overview of the second generation adjusted daily precipitation dataset for trend analysis in Canada. Atmosphere-Ocean 49:163-177

Mohammed GA, Hayashi M, Farrow CR, Takano Y (2013) Improved characterization of frozen soil processes in the Versatile Soil Moisture Budget model. Canadian Journal of Soil Science 93:511-531 doi: 10.4141/cjss2012-005

Mohammed AA, Pavlovskii I, Cey EE, Hayashi M (in review) Effects of preferential flow on snowmelt partitioning and groundwater recharge in frozen soils. Hydrology and Earth System Sciences Discussions doi: 10.5194/hess-2019-169

Muenchrath AK (2019) Land-use and topographic effects on near-srface saturated hydraulic conductivity and soil properties in southern Alberta. BSc Hon. Thesis, University of Calgary

Oncley S, Foken T, Vogt R, et al (2007) The energy balance experiment EBEX-2000. Part I: Overview and energy balance. Boundary-Layer Meterology 123:1 1-28 doi: 10.1007/s10546-007-9161-1

Ozesmi SL, Bauer ME (2002) Satellite remote sensing of wetlands. Wetland Ecology Management 10:381–402. doi: 10.1023/A:1020908432489

Parsons DF, Hayashi M, van der Kamp G (2004) Infiltration and solute transport under a seasonal wetland: Bromide tracer experiments in Saskatoon, Canada. Hydrological Processes 18:2011–2027. doi: 10.1002/hyp.1345

Pavlovskii I, Hayashi M, Lennon MR (2018) Transformation of snow isotopic signature along groundwater recharge pathways in the Canadian Prairies. Journal of Hydrology 563: 1147-1160 doi: 10.1016/j.jhydrol.2017.09.053

Pavlovskii I (2019) Groundwater recharge in the Canadian Prairies: mechanisms, constraints, and rates. Doctoral dissertation, University of Calgary

Pavlovskii I, Hayashi M, Itenfisu D (2019a) Midwinter melts in the Canadian prairies: energy balance and hydrological effects. Hydrology and Earth System Sciences 23:4 1867-1883 doi: 10.5194/hess-23-1867-2019

Pavlovskii I, Hayashi M, Cey EE (2019b) Estimation of depression-focussed groundwater recharge using chloride mass balance: problems and solutions across scales. Hydrogeology Journal 27:6 2263-2278 doi: 10.1007/s10040-019-01993-2

Peng H, Mayer B, Harris S, Krouse HR (2004) A 10-year record of stable isotope ratios of hydrogen and oxygen in precipitation at Calgary, Alberta, Canada. Tellus, Series B: Chemical and Physical Meteorology 56:147–159. doi: 10.1111/j.1600-0889.2004.00094.x

Planet Team (2017) Planet Application program interface: In space for life on Earth. San Francisco CA. https//api.planet.com

Pomeroy J, Gray D, Shook K, et al (1998) An evaluation of snow accumulation and ablation processes for land surface modelling. Hydrological Processes 12:15 2339-2367 doi: 10.1002/(SICI)1099-1085(199812)12:15<2339::AID-HYP800>3.0.CO;2-L

Pomeroy J, de Boer D, Martz LW (2007) Hydrology and water resources. In: Thraves BD, Lewry ML, Dale JE et al. (eds) Saskatchewan: Geographic Perspectives. University of Regina Press, pp 63-80

Prior GJ, Hathway B, Glombick PM, et al (2013) Digital Data 2013-0018 Bedrock Geology of Alberta (GIS data, polygon features)

Renton D, Mushet D, DeKeyser E (2015) Climate change and prairie pothole wetlands – mitigating water-level and hydroperiod effects through upland management. USGS Scientific Investigations Report 2015-5004:1-21

Rover J, Wright CK, Euliss NH Jr, et al (2011) Classifying the hydrologic function of prairie potholes with remote sensing and GIS. Wetlands 31:319-327 doi: 10.1007/s13157-011-0146y

Scanlon BR, Healy RW, Cook PG (2001) Choosing appropriate technique for quantifying groundwater recharge. Hydrogeology Journal 10:18–39. doi: 10.1007/s10040-0010176-2

Scanlon BR, Reedy RC, Stonestrom DA, et al (2005) Impact of land use and land cover change on groundwater recharge and quality in the southwestern US. Global Change Biology 11: 1577–1593. doi: 10.1111/j.1365-2486.2005.01026.x

Scanlon BR, Keese KE, Flint AL, et al (2006) Global synthesis of groundwater recharge in semiarid and arid regions. Hydrological Processes 20:3335–3370. doi: 10.1002/hyp.6335

Sethre PR, Rundquist BC, Todhunter PE (2005) Remote Detection of Prairie Pothole Ponds in the Devils Lake Basin, North Dakota. GIScience Remote Sensing 42:277–296. doi: 10.2747/1548-1603.42.4.277

Soil Classification Working Group: The Canadian system of soil classification. Agriculture and Agri-food Canada publication 1646:187, 1998

Sprenger M, Tetzlaff D, Soulsby C (2017) Soil water stable isotopes reveal evaporation dynamics at the soil-plant-atmosphere interface of the critical zone. Hydrological Earth Systems Science 21:3839–3856. doi: 10.5194/hess-21-3839-2017

Statistics Canada. (2017). Table 32-10-0408-01 Tillage practices used to prepare land for seeding. doi: 10.25318/3210040801-eng. Last accessed 2019/09/06.

van der Kamp G, Hayashi M, Gallen D (2003) Comparing the hydrology of grassed and cultivated catchments in the semi-arid Canadian prairies. Hydrological processes 17:3 559-575 doi: 10.1002/hyp.1157

van der Kamp G, Hayashi M, Bedard-Haughn A, Pennock D (2016) Prairie pothole wetlands – suggestions for practical and objective definitions and terminology. Wetlands 36 (Suppl 2):S229-S235 doi: 10.1007/s13157-016-0809-9

van Dijk T. (2005) Depression-focused recharge and the impacts of land use on the hydrology of small depressions in Calgary, Alberta. MSc. Thesis, University of Calgary

Walker GR, Zhang L, Ellis TW, et al (2002) Estimating impacts of changed land use on recharge: Review of modelling and other approaches appropriate for management of dryland salinity. Hydrogeology Journal 10: 68–90. doi: 10.1007/s10040-001-0181-5

Watanabe K, Kugisaki Y (2017) Effect of macropores on soil freezing and thawing with infiltration. Hydrological Processes 31:2 270-278 doi: 10.1002/hyp.10939

Webb E, Pearman G, Leuning R (1980) Correction of flux measurements for density effects due to heat and water vapour transfer 106: 85-100 doi: 10.1002/qj.49710644707

Wilczak JM, Oncley SP, Stage SA (2001) Sonic anemometer tils correction algorithms. Boundary-Layer meterology 99:127-150 doi: 10.1023/A:1018966204465

Winter TC, Rosenberry D (1995) The interaction of groundwater with prairie pothole wetlands in the Cottonwood Lake area, east-central North Dakota, 1979-1990. Wetlands 15:3 193-211

Zaitlin B, Hayashi M, Clapperton J (2007) Distribution of northern pocket gopher burrows, and effects on earthworms and infiltration in a prairie landscape in Alberta, Canada. Applied Soil Ecology 37: 88-94

Appendix A – Parameters for Depth-Area-Volume Equation for Remote Sensing

The height of water in a depression is be related to both the ponded area and pond volume for individual depressions. By determining the water height or area, and calculating the volume using the prescribed equations for each depression (Hayashi and van der Kamp 2000), it is possible to estimate snowmelt runoff.

Snowmelt runoff was estimated using the remote sensing technique (Chapter 4) in 17 grassland and 13 cropland catchments in the West Nose Creek watershed (Figure 4.1). The depth-area-volume (*h*-*A*-*V*) relationships for each were determined by fitting the equations of Hayashi and van der Kamp (2000):

$$A = s\left(\frac{h}{h_o}\right)^{2/p} \tag{A1}$$

$$V = \frac{s}{(1+2/p)}\frac{h^{1+(2/p)}}{h_o^{2/p}} \tag{A2}$$

where

A is the ponded area (m^2) corresponding to the water height h (m)

s (m^2) is a scaling constant equal to the ponded area when $h = h_o$

p is a scaling factor related to the shape of the basin

h is the height of the water in the depression (m)

h_o is the unit depth (= 1 m)

V is the volume of water (m^3) corresponding to the water height h.

with s (m^2) and p (-) values to heights, areas, and volumes extracted through the DEM analysis as found in Pavlovskii (2019). Values for s and p were determined using the solver function in Excel to minimize the root-mean-squared error for each height and corresponding area or volume. The values are reported in Table A.1, with sample cropland and grassland best-fit graphs shown in Figures A.1 and A.2 respectively. As s values are equal to the ponded area corresponding to $h = 1$ m, the relationship between catchment size and s values are indicative of what fraction of the catchment is ponded in high runoff years.

Table A.1. Catchment IDs (from DEM extraction), catchment area (A_c), and s and p value for the analysed grassland and cropland catchments.

Land use	Catchment ID	A_c (m^2)	s (m^2)	p
Grassland	6269	17153	1909	1.84
	6279	7270	758	2.39
	6287	9165	1287	1.36
	6333	20300	375	1.98
	6367	18533	6517	1.89
	6384	8336	1687	2.81
	6516	49271	10895	1.49
	6571	6319	2740	2.56
	6624	36785	5074	1.11
	8289	10762	2894	3.34
	8330	7265	761	1.45
	8334	7552	1043	1.92
	8349	4305	594	1.67
	8356	50358	6152	3.26
	8362	18098	4361	1.80
	8370	9685	1677	1.89
	8372	31083	8412	4.38
Cropland	8100	17194	4811	0.99
	8116	19482	7818	1.15
	8128	39382	2255	1.19
	8131	32083	715	1.67
	8162	9599	1207	1.29
	8181	12601	1062	1.01
	8292	17652	342	1.74
	8293	14719	856	1.18
	8301	19414	3052	1.62
	8624	34079	1154	1.72
	8625	15189	1550	1.51
	8632	9961	7199	1.49
	8679	9109	2417	1.28

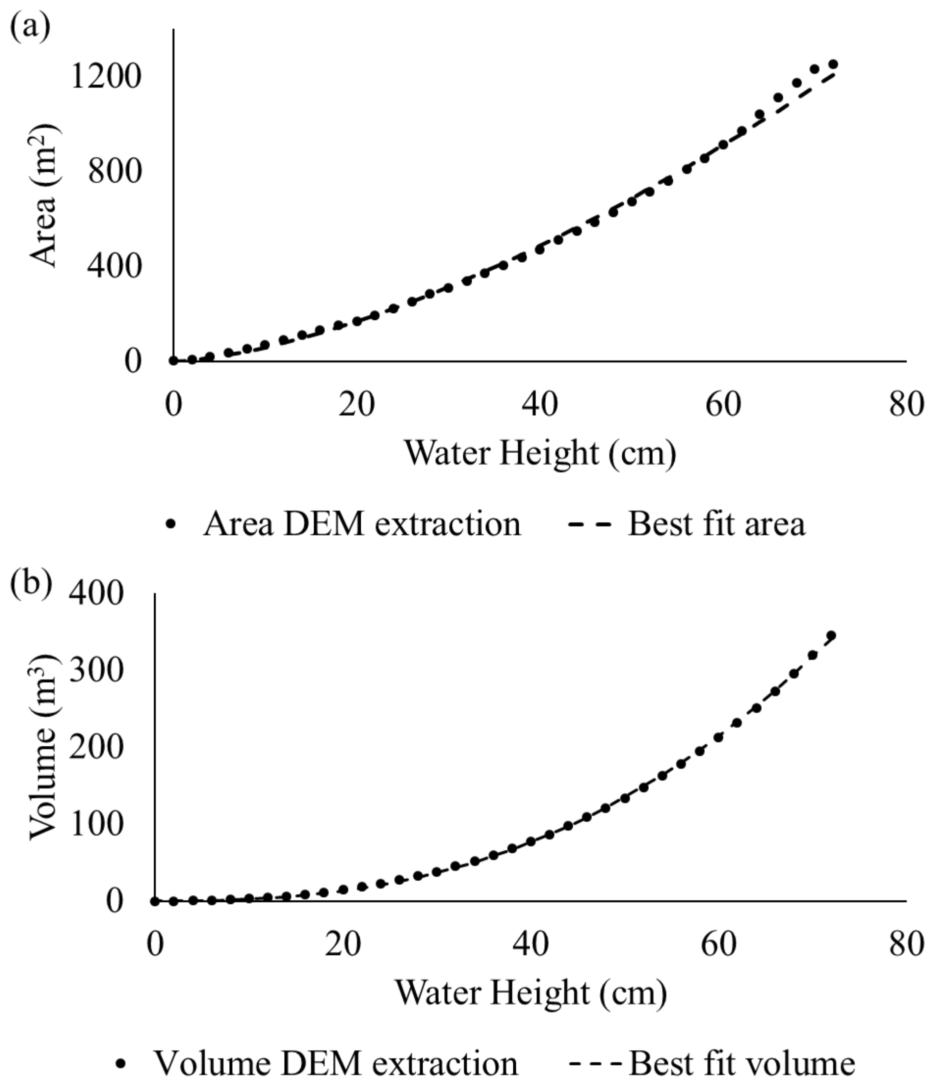

Figure A.1. Cropland DEM extracted and best fit areas (a) and volumes (b) for catchment 8162. The best fit values were calculated using *s* and *p* values as found in Table A.1.

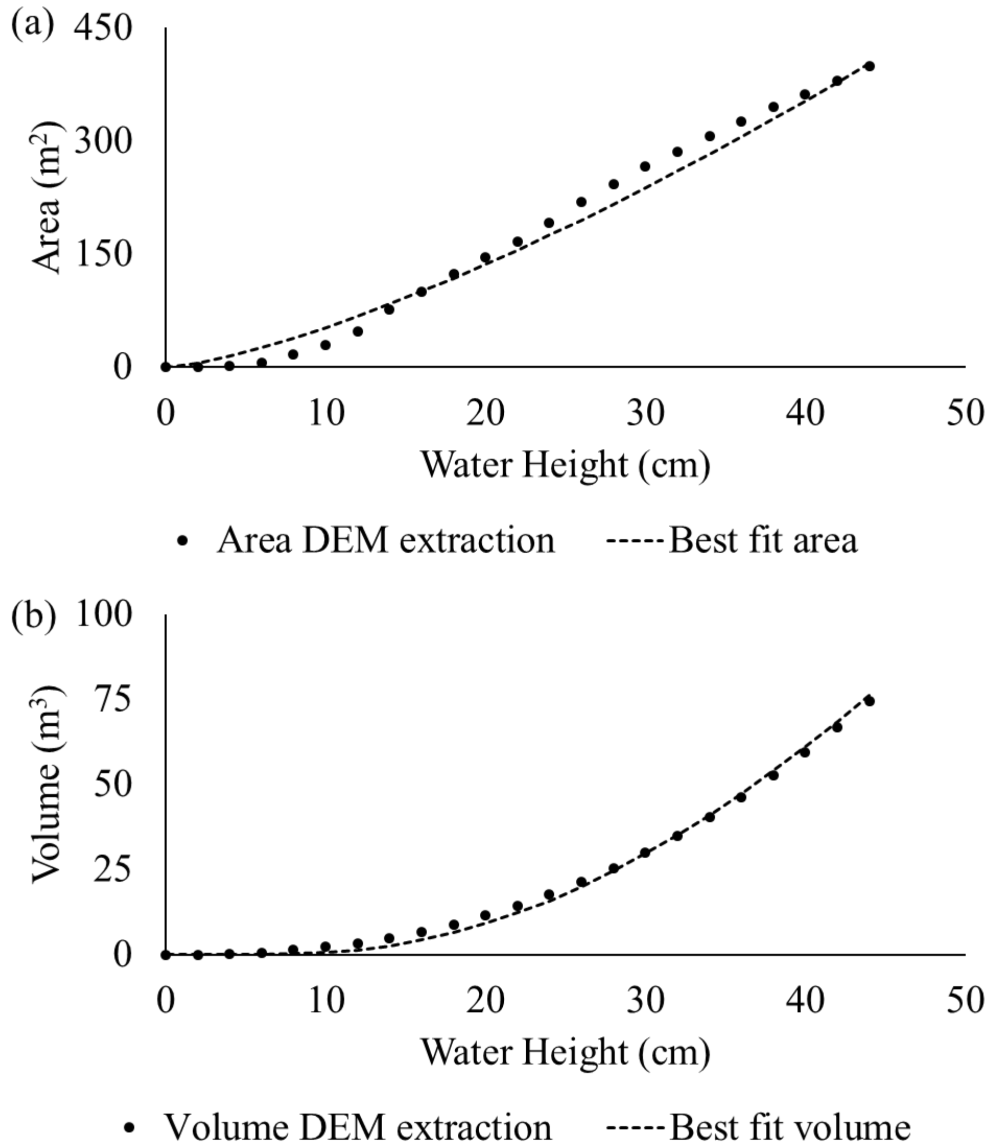

Figure A.2. Grassland DEM extracted and best fit areas (a) and volumes (b) for catchment 8330. The best fit values were calculated using *s* and *p* values as found in Table A.1.

Appendix B – Estimation of Specific Yield

To estimate the range of specific yield expected for TGC, water retention characteristic curves were created. The relationship between soil matric potential and volumetric water content was determined for undisturbed soil samples taken from the soil pits during the installation of soil moisture and temperature sensors (Chapter 3, Figure 3.2a). Soil samples were collected in 100 cm^3 stainless steel rings, which were 5 cm in diameter and 5 cm in height. Soil was partially removed from within the rings before analysis to create a height of 3 cm of soil in the ring, and an average volume of 60 cm^3. The soil samples were analysed using a pressure plate extraction system with matric potential head ranging from -0.01 to -50 m during a stepwise drainage process (Soil Moisture Corp, 5 Bar Pressure Plate Extractor). Saturated water content was determined by saturating the soil samples before analysis and weighing them, and once the pressure plate analysis was complete, the soil samples were completely dried in an oven and weighed again. Water contents at matric potential head lower than -50 m were estimated using a dewpoint potentiometer (METER group, WP4C).

The water content (θ) and corresponding matric potential head (ψ) were plotted, and a line was fit using van Genuchten (1980) equation (Equation B.1) through the solver function in Excel, which minimized the error between the fit line and data points by changing n and α (Figures B.1-B.4).

$$\theta = (\theta_s - \theta_r)(1 - \left(1 + \alpha(-\psi)\right)^n)^m \tag{B.1}$$

where:

θ_s is the saturated water content

θ_r is the residual water content *n* and *m* are fitting parameters for the van Genuchten model (-), where

$m = 1 - 1/n$

α is the reciprocal of capillary length (m^{-1})

The depth of the water table under the depressions before snowmelt recharge events were approximately 4 m below ground surface (Figure 5.9). Therefore, specific yield was estimated by calculating the total water volume between the ground surface and the water table located at 3.9 m and 4.0 m below the surface (Figure B.5). The difference between the two curves in Figure B.5 indicate the total volume of water drained by lowering the water table by 0.1 m. Dividing this volume by 0.1 m gives an estimate of specific yield by definition (Table 3.1). This calculation assumes the static condition within the vadose zone, instantaneous drainage, and no hysteresis in the water retention characteristics.

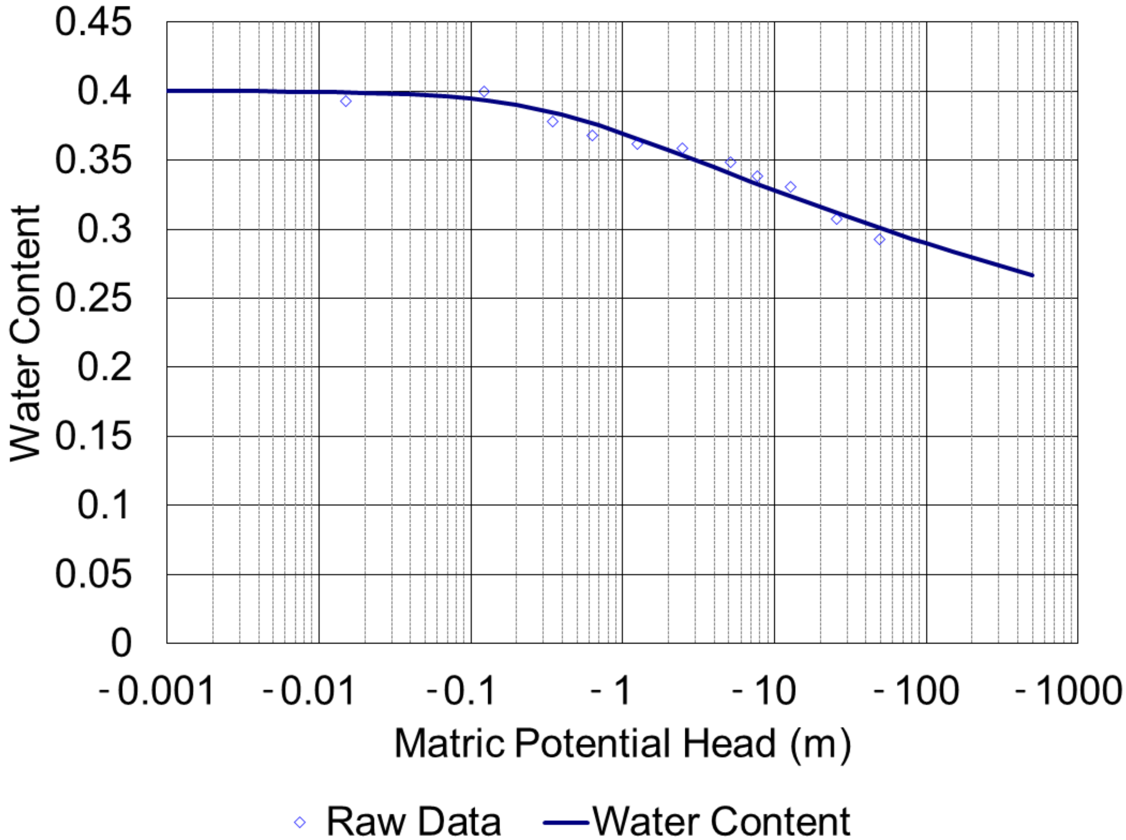

Figure B.1 Water retention characteristic curve for the soil sample collected from the TGC depression at 100 cm depth.

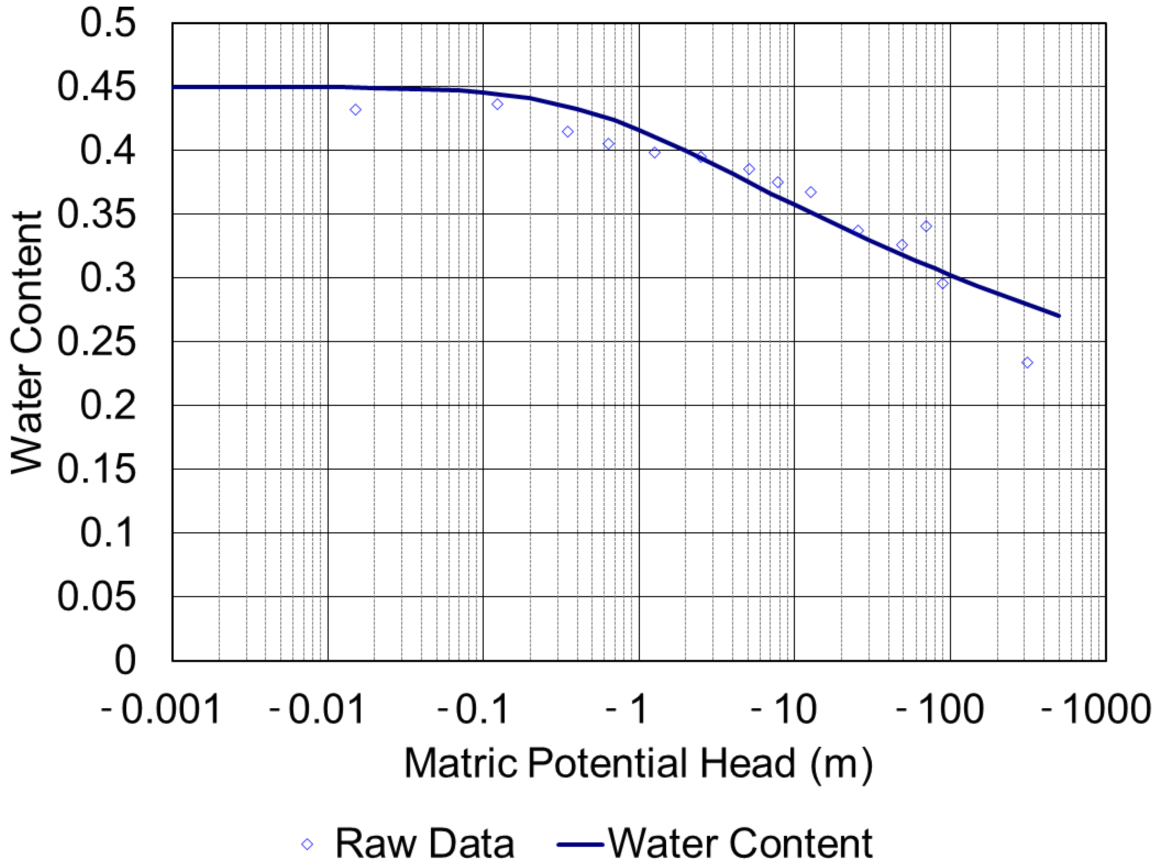

Figure B.2. Water retention characteristic curve for the soil sample collected from the TGC depression at 150 cm depth.

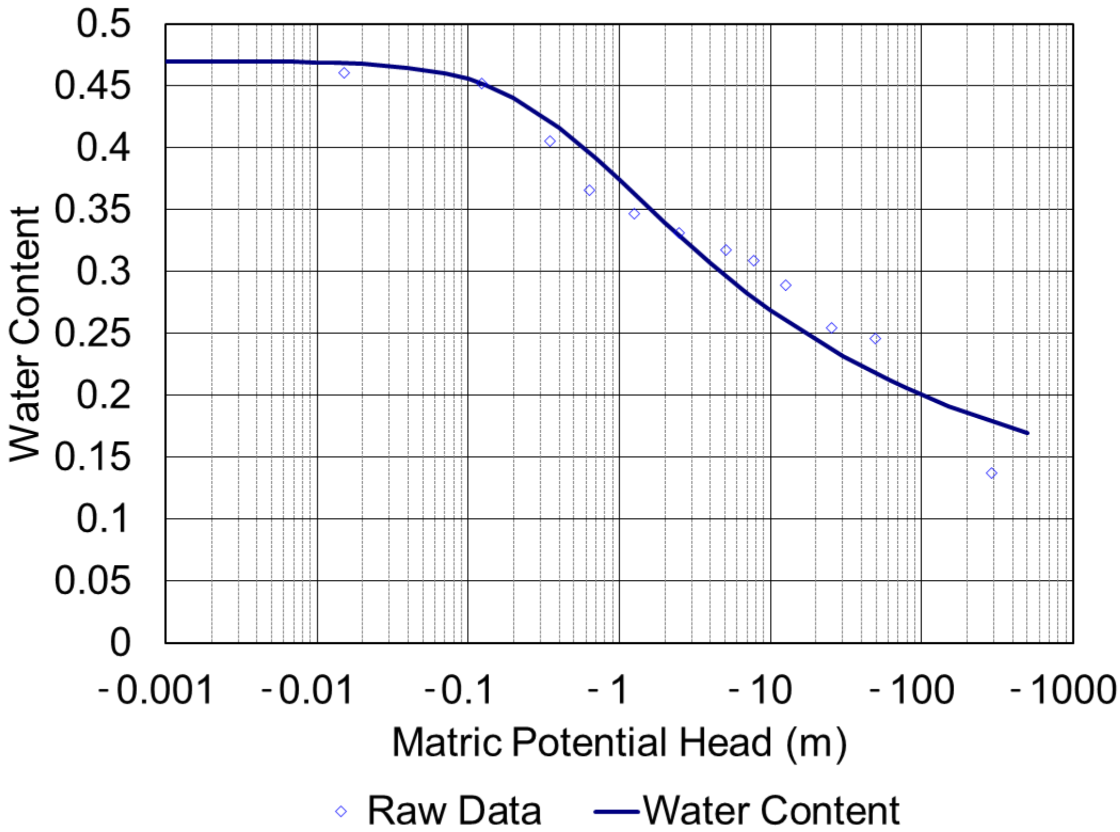

Figure B.3. Water retention characteristic curve for the soil sample collected from the TGC upland at 100 cm depth

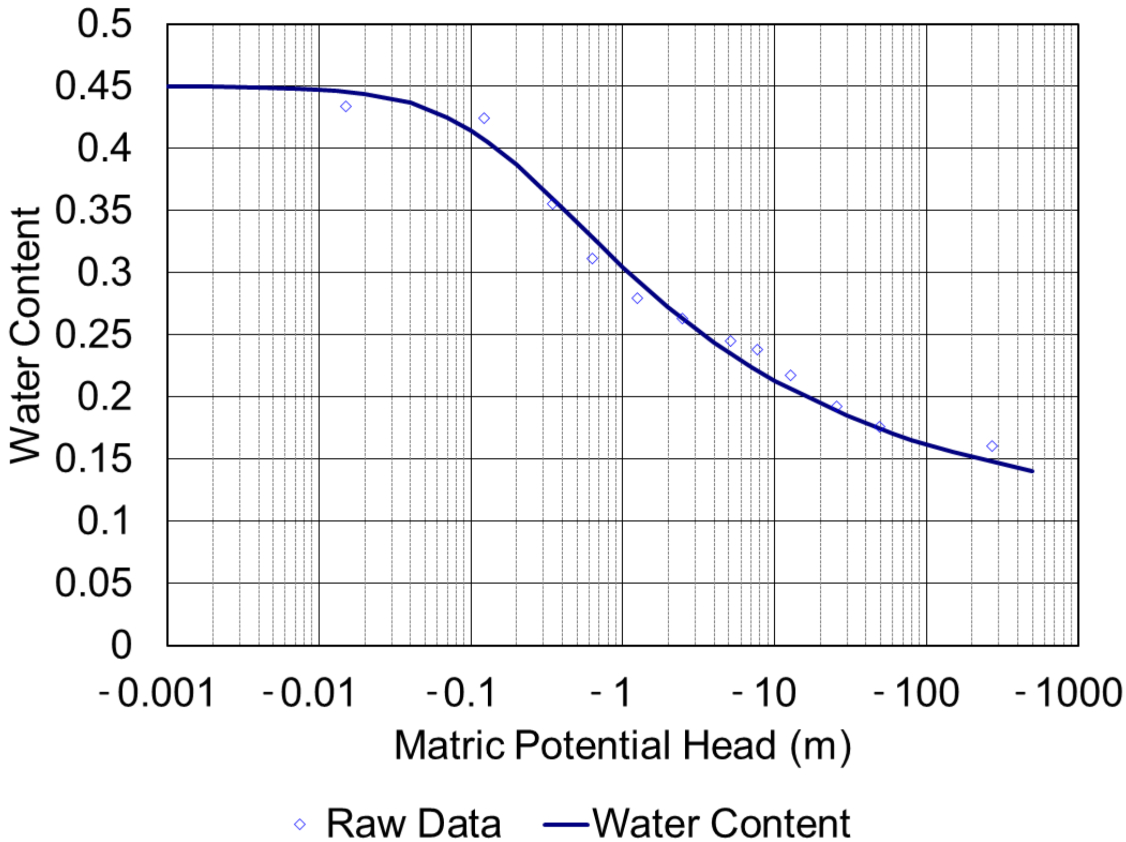

FigureB.4. Water retention characteristic curve for the soil sample collected from the TGC upland at 150 cm depth.

Table B.1. van Genuchten fitting parameters and specific yield estimates for four soil rings based on matric potential curves generated from pressure plate analysis.

Location	Depth (cm)	θ_s	θ_r	n	m	α	h_o	$(1-n)/n$	Sy
Depression	100	0.4	0.1	1.08	0.074	2.97	3	-0.07417	0.0933
	150	0.45	0.1	1.106	0.096	1.78	3	-0.0956	0.0683
Upland	100	0.47	0.1	1.227	0.18	3.14	3	-0.18502	0.1628
	150	0.45	0.1	1.264	0.21	7.21	3	-0.2087	0.2059

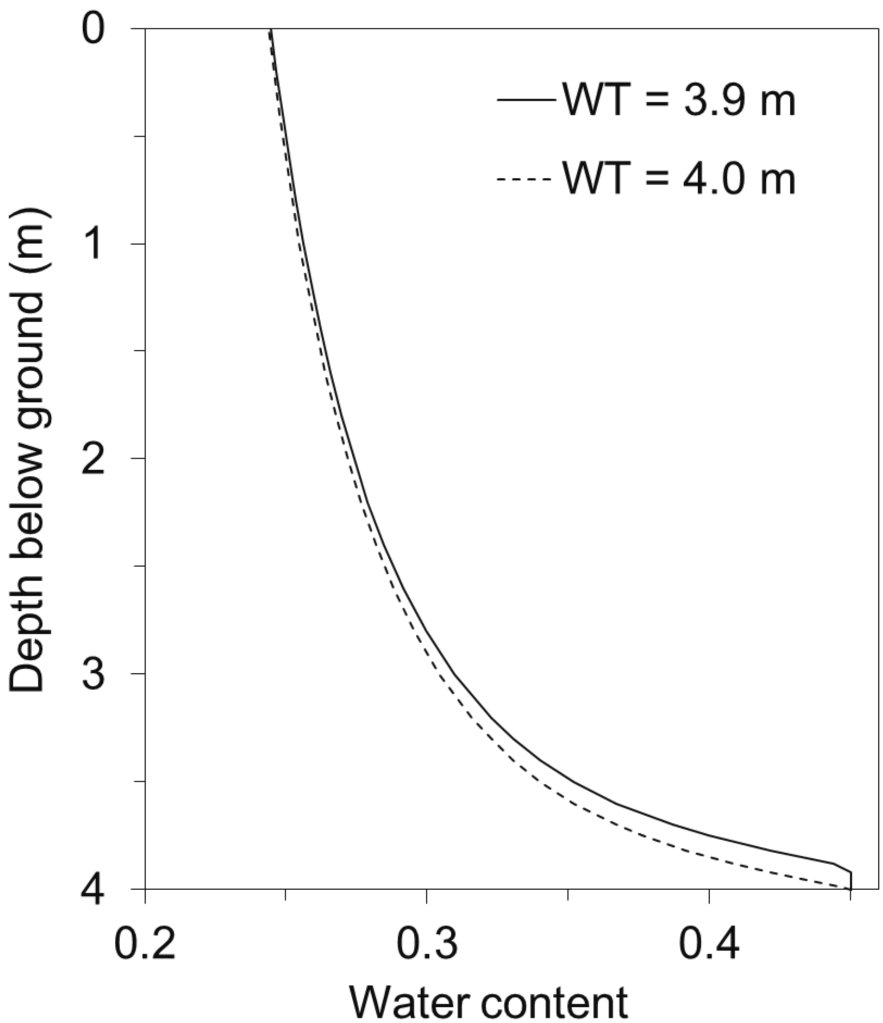

Figure B.5. Calculated water content with depth for water table depths of 3.9 and 4.0 m, with the area between the two curves used to estimate specific yield.

Appendix C – Electrical Resistivity Tomography

Electrical resistivity tomography is (ERT) is a geophysical tool used to image the subsurface, with depths of investigation 4-5 times the distance between the electrodes. The resistivity of subsurface materials is strongly related to clay content in low-salinity groundwater systems, with the charge that most clays carry causing them to act as good conductors, and coarser sediments such as sand acting as worse conductors (Yazicigal and Sendlein 1982).

Five two-dimensional electrical resistivity profiles of varying lengths and spacing (Table C.1) were acquired at TGC in October 17 and 18, 2017 to identify the areas of salt accumulation and determine the extent of both the sand layer and bedrock found beneath the site. A combined Wenner and dipole-dipole array configuration was used with an IRIS instruments Syscal Pro 72 electrode system. Prior to the inversion, noisy data was filtered by deleting the data that had a standard deviation larger than 1 and voltage on measurement electrode pair smaller than 0.1 V. The data were then inverted using the Geotomo RES2DINV software (Loke and Barker 1996) using the robust inversion algorithm with 1/2 grid cell refinement.

Cutoff depths for the images were assumed to be half of the theoretical depth of investigation for a Wenner array (L. Bentley, personal communication). This theoretical depth is based on the largest electrode separation multiplied by 0.52. For a line with 5 m spacing, this corresponds to 23 electrodes, multiplied by 5 m, which is then multiplied by 0.52 to give 59.8 m. Half of this depth is 30 m, which was chosen for the depth for 5 m lines. Cutoff depth for the 4 m spacing was 25 m, and for the 1 m line it was 6 m.

Survey lines in the cropland went through multiple depressions (Figure C.1), with the inverted cross sections corresponding to each line created (Figure C.2, Figure C.3). Two lines were completed with different spacing over the main depression to refine the image directly beneath the depression (denoted in Table C.1 and Figure C.1 as Line 1 and Line 1a).

The same system was used at TGG in September 2014, however only two lines were completed, one with 5 m spacing and one with 1 m spacing, both through the west depression (Figure C.4, Figure C.5).

Table C.1. Line number, length, and spacing for the TGC ERT surveys.

Line Number	Length (m)	Spacing (m)
1	284	4
1a	71	1
2	355	5
3	355	5
4	355	5

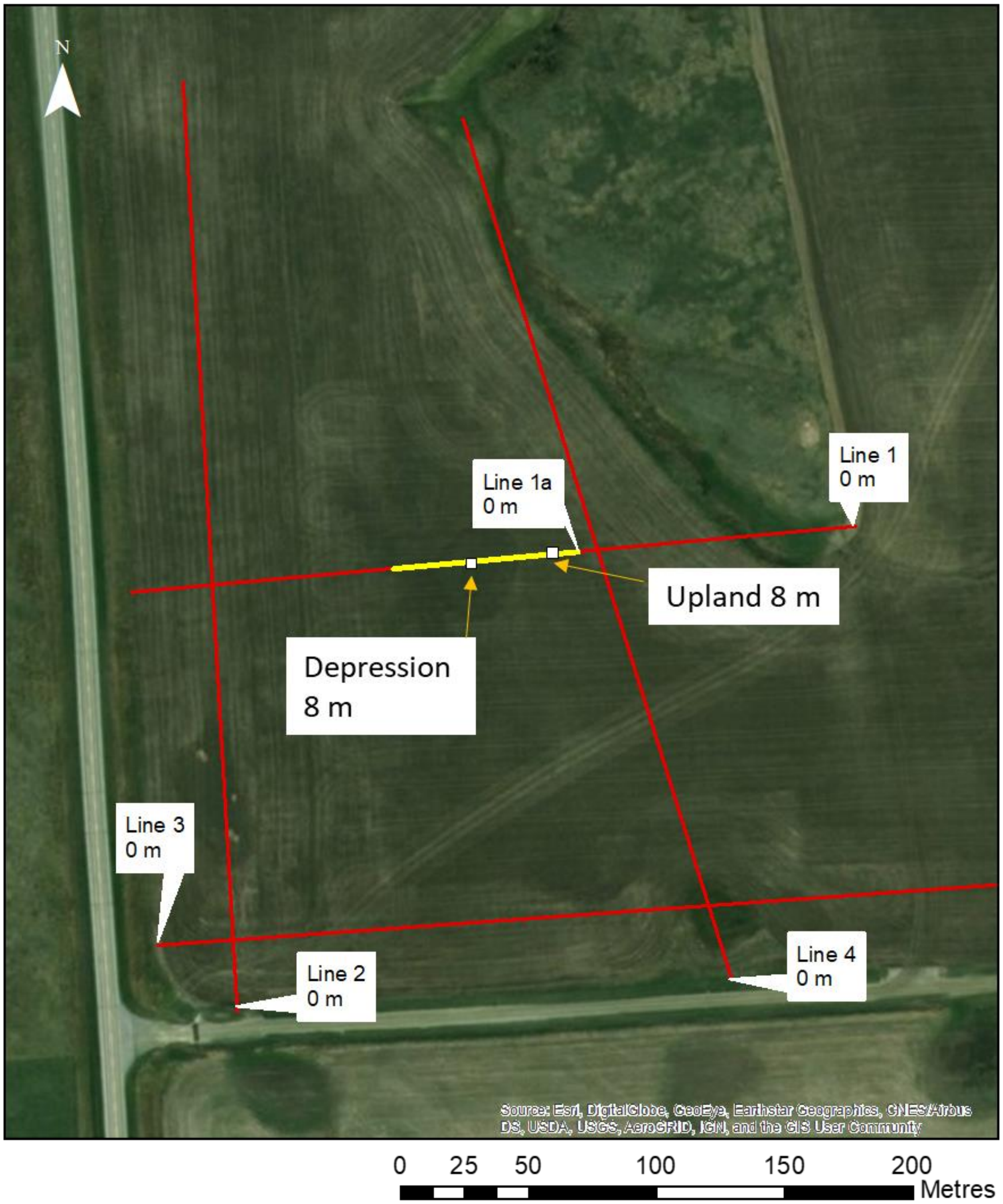

Figure C.1. Location of ERT lines and starting points at TGC. Borehole locations in the depression and upland are indicated.

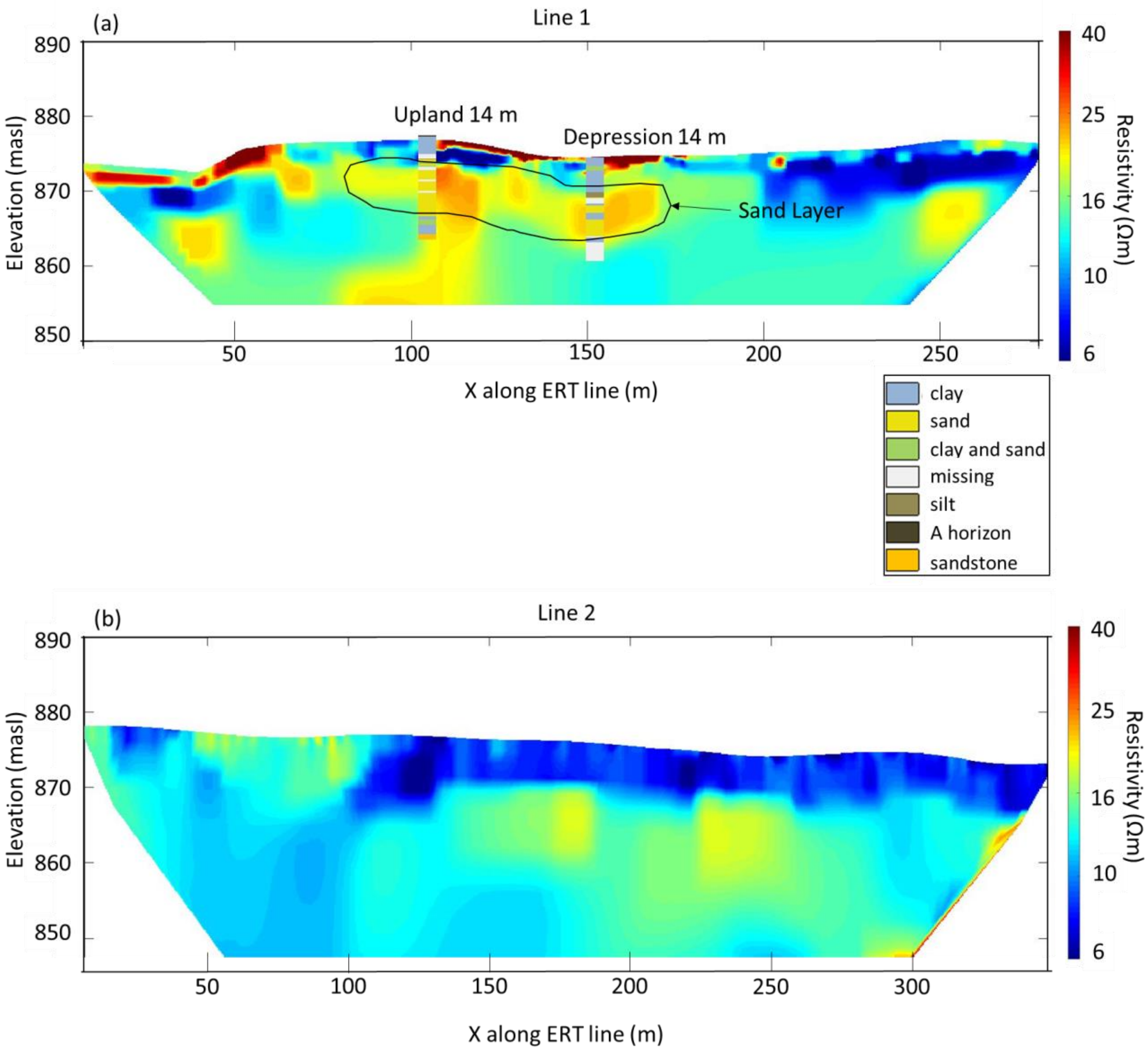

Figure C.2. ERT profiles for TGC Line 1, 1a (a) and Line 2 (b). Borehole locations and stratigraphy are indicated on Line 1, as is the extent of the sand layer observed between the upland and depression wells..

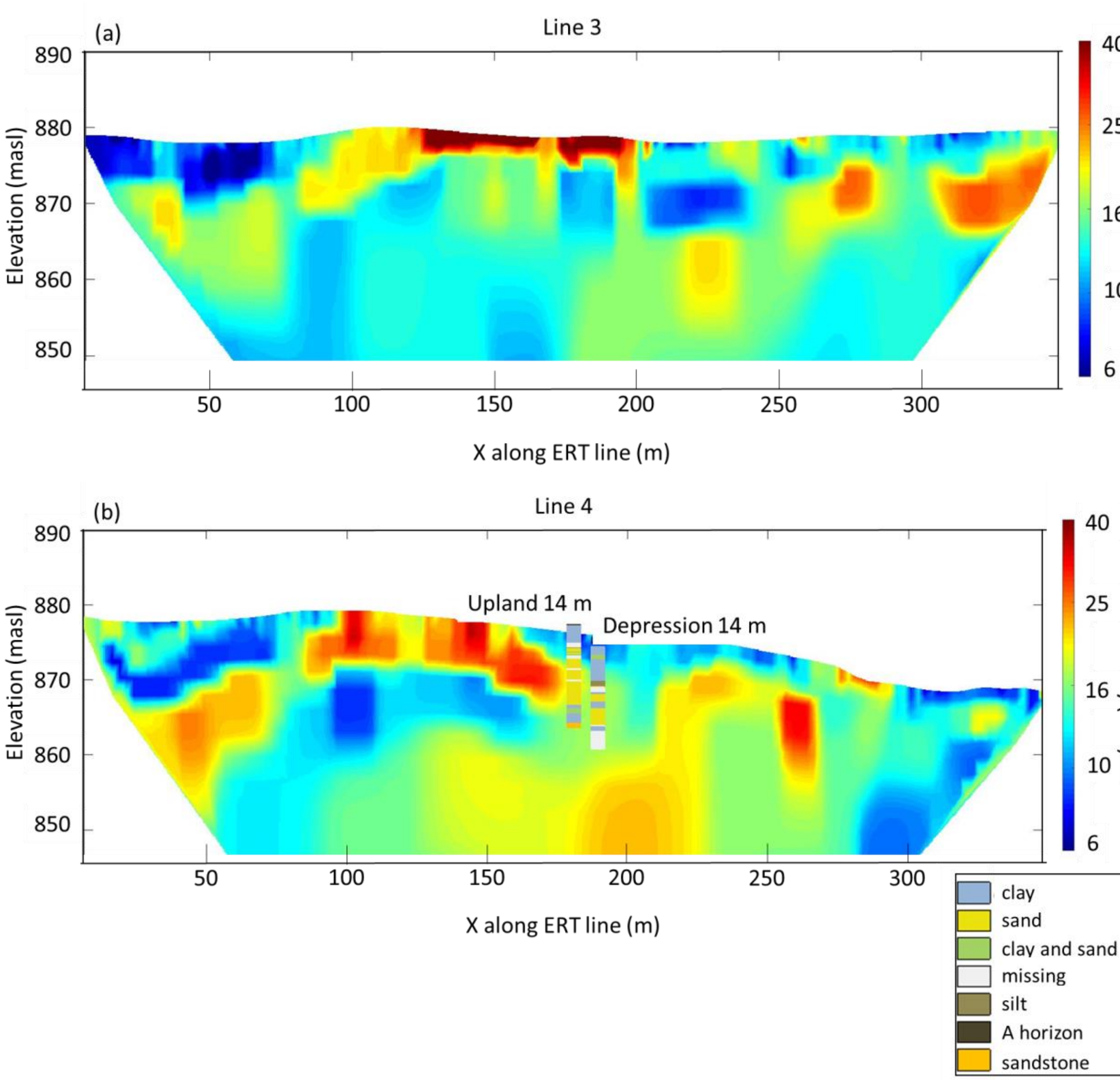

Figure C.6. ERT profiles for TGC Line 3 (a) and Line 4 (b). Well locations and stratigraphy are indicated on Line 4.

Figure C.4. ERT line locations and starting points for TGG. Line 1 had 5 m electrode spacing and Line 2 had 1 m spacing.

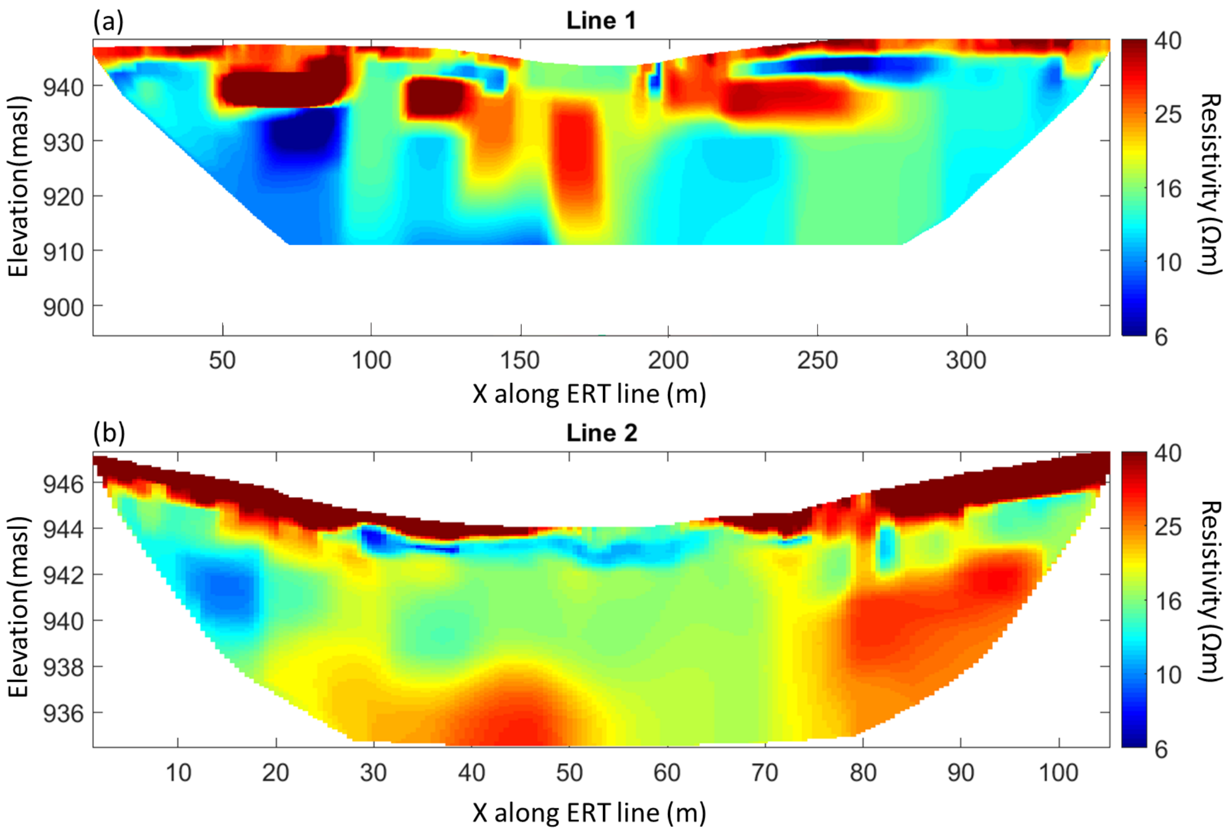

Figure C.5. ERT profiles for TGG. Line 1 (a) had 5 m spacing and Line 2 (b) had 1 m spacing

Appendix D – Piezometer Water Levels at TGC Site

Chloride and isotope values in the depression 8 m piezometer water samples at TGC were found to be different than the pore-water composition at the time of drilling. It was speculated that this difference is due lateral flow between the upland and depression within the sand layer. Connectivity in the sand layer at TGC was observed during the spring melt event in 2018, where the 8 m piezometers in the depression and upland, both in the sand unit, responded to snowmelt infiltration (Figure D.1). This connectivity, and generally greater hydraulic conductivity in the sand unit compared to the clay layers, could explain the differences in isotopic composition in groundwater due to mixing. The upland piezometer has a higher head than the depression piezometer, also leading to the movement of different isotopic water to the depression from the upland. The connectivity of the sand layer was also observed in the ERT (Appendix C, Figure C.1a).

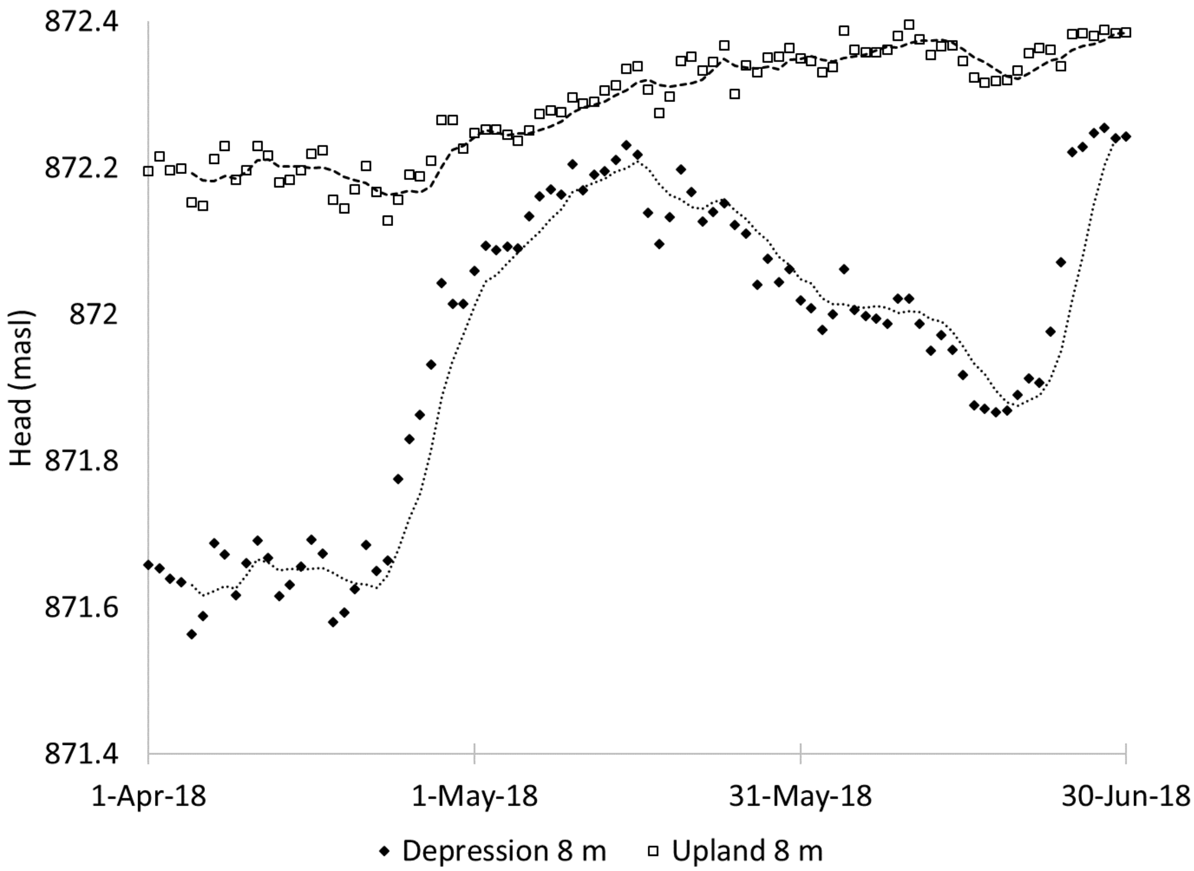

Figure D.1. Head values for the depression and upland 8 m piezometers from April 1, 2018 to June 30, 2018. Dashed lines are a moving average through the daily data points to show trends.

Appendix E - Detailed Piezometer Information

This appendix lists the detailed information on piezometer installations and locations. Locations of the piezometers are indicated in Chapter 3 (Figure 3.2). Detailed coordinates and identification numbers (which are written on the sides of piezometers inside of the casings in the field) are indicated in Table E.1. The diameter of all boreholes was assumed to be 0.15 m, based on the auger diameter. All piezometer screens were installed to the bottom of the borehole and were capped with a PVC cap. Sand packs were installed to cover the screen lengths. When formation sand was allowed to slough around the screens, bentonite was added above the sloughed sand once the screens were covered. Finishing details regarding sand packs and borehole sealing are also indicated Table E.1. Unless otherwise stated, all units of length are in metres. Hydraulic conductivity was determined via slug tests.

Boreholes were sealed with bentonite chips. In the case of TGCU4504 and TGCD4504, formation sand was allowed to slough to fill the region between borehole wall and casing. This sloughing was sealed on both ends by bentonite chips, and formation sand did not reach the screens of these two wells.

Table E.1. Piezometer completion information for Triple G. All depths and lengths are in metres.

Site	Location	ID	Drilling Date	Depth to Bottom of Hole	Screen Length	Top of Casing Elevation	Ground Surface Elevation	Casing Diam	Formation Screened	Sand or Formation Packed?	Ksat (m/s)
Grassland	Upland	2014TGU5001	Nov-14	15.2	1.5	924.157	923.246	0.0508	till	Sand	--
	Depression	2014TGD4001	Nov-14	11.9	1.5	921.2278	920.5058	0.0508	till	Sand	6.10E-07
		2014TGD2402		7.2	1.5	921.2982	920.4962	0.0508			1.80E-08
		2014TGD1003		3.2	0.76	921.2472	920.5252	0.0254			3.60E-07
Cropland	Upland	TGCU4504	02-Jun-2017	14.55	1.5	878.0264	877.3604	0.0508	bedrock	Sand	8.50E-07
		TGCU2505		8.79	1.5	878.0382	877.3402		silty sand	Formation (sloughed sand)	4.70E-08
	Depression	TGCD4501	01-Jun-2017	14.55	1.5	875.1047	874.4047	0.0508	till	Sand	5.40E-10
		TGCD2502		8.2	1.5	875.1433	874.4523		silty sand	Formation (sloughed sand)	6.10E-06
		TGCD1503		5.14	1.5	875.1104	874.4224		till	Sand	1.60E-08